A Universal Grid-Forming VSC Control for Future Power System

Yuan Lu

A thesis presented in fulfilment of the requirements for the degree of Doctor of Philosophy

Department of Electronic and Electrical Engineering

University of Strathclyde, Glasgow, UK

August 2023

This thesis is the result of the author's original research. It has been composed by the author and has not been previously submitted for examination which has led to the award of a degree.

Signed: Date:

Acknowledgement

I would like to express my deepest gratitude to all those who helped me during my life in UK. The PhD program is an unforgotten experience and great wealth for me.

With my most sincere respect, I would like to thank my supervisor Prof. Lie Xu for his patient guidance, sincere encouragement and continuous support. Without his inspiration, I would not have got through the most difficult time in my PhD life. His profound knowledge, rigorous research attitudes and enthusiasm, innovative ideas and efficient research methods will benefit me for life.

My special gratitude to Dr. Dong Chen and Dr. Rui Li, who have always been patient and generous to give me valuable comments and suggestions for my research. My gratitude extends to Dr. Yin Chen, who helped me on the coding work to build the small signal model of the grid-forming and grid-following VSCs in Chapter 6. With his assistance and support, I got the ability to understand and build the small signal models. I would also like to thank Dr. Dimitrios Vozikis and other colleagues in PEDEC research group for all the help and advice.

Great acknowledgement is made to my friends, Dr. Kamyab Givaki and Dr. Shuren Wang, for all concerns and companies in the past time.

Finally, I would like to express my most gratitude to my parents for their support and understanding during my life in the UK.

Abstract

To decarbonise the electricity sector, power systems are facing a significant transition to converter-dominated systems with higher penetration of renewable energy generations to replace conventional power generations using synchronous generators (SGs), changing the characteristics of power grid. Unlike SGs, power electronic converters do not contain rotating mechanical components. Accordingly, the mechanical properties owned by SGs will not be exhibited in the future power system, which can result in various issues in term of power system stability and the ability of faults and disturbances ride through. As power electronic converters are used to interface renewable resources with the power grid, they rely on the control dynamics and algorithms to maintain the entire system power balance and stability. However, there are lots of different control requirements considering the various grid conditions, including weak and strong grid connection, islanding, symmetrical and asymmetrical AC faults, which brings a big challenge for the control design of the power electronic converters. This thesis proposes a universal grid-forming (GFM) VSC (Voltage source converter) control for future power system with consideration to the corresponding various grid conditions.

In this thesis, the control of grid-following (GFL) and GFM converters are reviewed firstly. The GFL control usually contributes to the regulation of active and reactive power output by injecting current through a vector current controller at a given phase. The grid phase is tracked by using a phase-locked loop (PLL) at all times. Different outer controller can be applied for different control purposes such as active power and voltage control. The GFL converters are predominantly applied in present renewable power generations, due to the capability in handing transient current during large transient events, precise control of current and good control dynamics, etc. However, as the GFL converters cannot regulate the system voltage and frequency directly, which makes them lack the capability of islanded operation. In addition, another constraint comes along with the use of vector current controller that causes the risk of instability on a weak grid. Intrinsically different from the GFL converters, the GFM converters use voltage regulation as the inner loop combined with power droop controller as the outer loop, to actively control their voltage and frequency outputs for the aim of voltage support. Hence, the GFM converters have

the ability to work stably on islanding network, as well as weak grid connection network. However, the most common issue for GFM converters is the absence of effective current control loop, which limits their overcurrent capability.

To synthesise the advantages of both GFM and GFL converters, a universal GFM VSC control is proposed. A direct voltage control in the dq reference frame is combined with a frequency droop control to regulate the AC voltage and frequency. Hence, the VSC has the capability of handling islanded operation. To ensure a stable grid connected operation, an adaptive power droop control is added as the outer loop to regulate the power exchanged between the converter and grid. A universal current limit control is also developed to limit the overcurrent and share the active and reactive current on both grid connection and islanding networks.

In order to enable the ability of asymmetrical faults ride-through, the GFM VSC control is built in double synchronous frames to enable independent control of positive- and negative-sequence components. An enhanced AC fault current control that employs both positive- and negative-sequence current control is proposed. An additional voltage balancing control is also developed to retain the AC voltage controller for fault current limiting. By applying this controller, the general fault current limiting, dq current distribution and negative-sequence current control when required can be achieved on a weak grid connection.

Finally, small signal analysis is carried out to compare the stability of the GFM and GFL VSCs on weak networks. The impedance-based method is adopted to derive the admittances of the VSCs and connected grid in the positive- and negative-sequence (pn) reference frame. Time-domain simulations are also performed to verify the accuracy of the small signal admittances. Stability improvement with the GFM VSC on a very weak grid is validated.

List of Abbreviations

GHG	Greenhouse Gas
COP27	2022 United Nations Climate Change Conference
EU	European Union
PV	Photovoltaic
SG/SM	Synchronous Generator/Machine
AC	Alternating Current
DC	Direct Current
GFL	Grid-Following
GFM	Grid-Forming
VSC	Voltage Source Converter
IGBT	Insulated Gate Bipolar Transistor
PWM	Pulse Width Modulation
SCR	Short Circuit Ratio
ROCOF	Rate of Change of Frequency
PCC	Point of Common Coupling
SSR	Sub-Synchronous Resonance
PLL	Phase-Locked Loop
VSG/VSM	Virtual Synchronous Generator/Machine
PI	Proportional-Integral
PR	Proportional-Resonant
HVDC	High Voltage Direct Current
KVL	Kirchhoff’s Voltage Law

List of Symbols

Z_s	Grid impedance
Z_{vir}	Virtual impedance
Z_c	Converter output impedance
Z_L	Impedance of the local load
Z_a	Additional load switched in/off
Y_{vsc}	Converter output admittance
R_s	Grid resistance
X	Reactance of the converter inductance
L_s	Grid inductance
L_f	Converter inductance of the LC filter
L_{tm}	Inductance of transformer
C	Converter capacitance of the LC filter
S	Static switch
s	Laplace operator
T_m	Time constant of the low-pass filter for active power droop loop
T_e	Time constant of the low-pass filter for reactive power droop loop
$I_{\lim}$	Maximum permissible current threshold
I_{th}	Certain current threshold
I_c	Converter filter bus current
I_l	Converter output current
V_s	Grid voltage
V_c	Converter filter bus voltage
V_{conv}	Converter output voltage

V_{dc}	DC voltage
V_{corrd}	Correction voltage
ω	Angular frequency of the grid
θ	Phase angle of the grid
P	Active power flow
P_L	Nominal local load demand
Q	Reactive power flow
$G_P(s)$	Active power controller
$G_Q(s)$	Reactive power controller
$G_{ud}(s)$	d-axis voltage controller
$G_{uq}(s)$	q-axis voltage controller
$G_{nf}(s)$	Closed loop transfer function of notch filter
$G_{pll}(s)$	Closed loop transfer function of PLL
M_{abc}	Modulation signal
ξ_i	Damping ratio of the vector current controller
ξ_{nf}	Damping ratio of notch filter
ω_i	Natural frequency of the vector current controller
k_p , k_q	Active and reactive droop coefficient of the power droop controller
k_{ppll} , k_{ipll}	Proportional and integral gain of PLL
k_{pi} , k_{ii}	Proportional and integral gain of the vector current controller
k_{pp} , k_{ip}	Proportional and integral gain for the close loop active power controller
k_{pq} , k_{iq}	Proportional and integral gain for the close loop reactive power controller
k_{pac} , k_{iac}	Proportional and integral gain for the AC voltage controller
k_{pvi}	Droop constant of the AC voltage controller

k_{pg} , k_{ig}	Proportional and integral gain of the voltage controller
k_{pv} , k_{iv}	Proportional and integral gain of the direct voltage controller
k_f	Droop coefficient of the frequency controller
k_d	Droop gain of the transient fault current limit controller
k_o	Proportional gain of the overcurrent limit controller
k_1 , k_2	Proportional gains of the dq current distribution controller
k_3	Proportional gain of the negative-sequence current controller
k_{vi}	Proportional gain for the reactive current order
k_b	Proportional gain of the voltage balancing controller
T_d	Time delay of digital control method
T_{sw}	PWM duty circle
λ	Eigenvalues of the open-loop transfer function matrices $Y_{vsc}(s)Z_s(s)$
Superscript 0	Nominal value
Superscript *	Reference value
Superscript +	Positive-sequence component
Superscript -	Negative-sequence component
Superscript s	Variable in the system reference frame
Subscript d,q	dq-axes components

List of Figures

List of Tables

Table of Contents

Chapter 1 Introduction

1.1 Renewable energy development

The greenhouse gas (GHG) emissions and dependency on fossil fuels lead to global warming, which adversely impacts the climate, ecosystem and health of people. Meanwhile, the overuse of fossil fuels has led to global energy crisis. With the intense negotiations and successful conclusions of the 2022 United Nations Climate Change Conference (COP27) in Egypt, all participated countries reaffirmed the Glasgow Climate Pact to limit global warming to around 1.5 ℃ in reach [1]. To achieve this goal, countries are aimed to cut GHG emissions in half by 2030 and reach net zero by 2050, which requires the rapid development and deployment of clean energy, especially renewable energy. Renewable capacity grew 5% averagely per year during 2009-2019 [2], and is expected to grow by almost 2400 GW over 2022-2027, equivalent to the entire current installed capacity in China [3]. With the global electricity demand rising, the electricity sector is being the first sector to be decarbonised [4]. The electricity sector takes a steady increasing share of the global energy supply, rising from 19% in 2010 to 23% in 2020 [2]. The sufficiently fast increase of renewable electricity generation is driving down the need of fossil fuels contributed to power [5]. As of 2022, nearly one-third of the global electricity production was contributed from renewable energy [6]. Since renewable energy is the only source of electricity generation that is expected to grow, it is seen to overtake coal as the largest source of global electricity generation by early 2025, and the share is forecast to reach 38% in 2027 [3].

Fig. 1.1 displays the progress towards renewable energy source targets for the European Union (EU). As seen, the renewable energy share had more than doubled between 2005 and 2022, while the share of total final energy consumption from renewable sources in the EU was maintained at 22% between 2020 and 2021. The EU increased the binding goal of the share of total final energy consumption from renewable sources from the existing 32% up to 42.5% by 2030 [7]. To meet this goal, the European energy system requires a deep and fast transition to renewable energy dominated system.

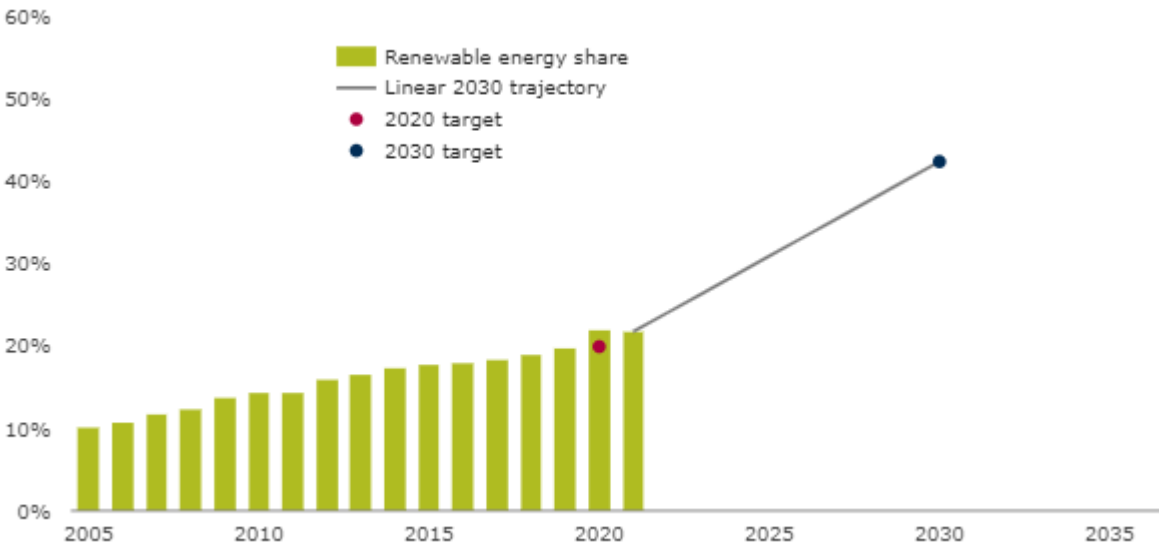

Fig. 1.1 Progress of installed power towards renewable energy source targets for EU [7]

Among all renewable energy sources, wind and solar energy have been the most reliable and rapidly exploited due to the lower cost and easy obtainment. In 2022, wind and solar achieves record growth, reaching 12% share of the global electricity generation in total [4]. According to the report of [3], global wind and solar PV (photovoltaic) capacity are forecast to grow by 570 GW and 1500 GW by 2027 respectively to make electricity from wind and solar PV reach 20% share of global power generation. For wind energy, it was the first time that the global capital expenditures committed to wind power exceeded the investment in fossil fuels in 2020 [8]. The installed wind power energy capacity for several representative countries is shown in Fig. 1.2. The installed wind power global capacity rose up to 825 GW in 2021, which was led by a dramatic leap in China as well as a significant jump in the United States [8]. The installed solar power energy capacities for several representative countries are shown in Fig. 1.3. As seen, China has led the world in the installed capacity since 2015, followed by the United States which outstripped Germany with a big jump in 2017.

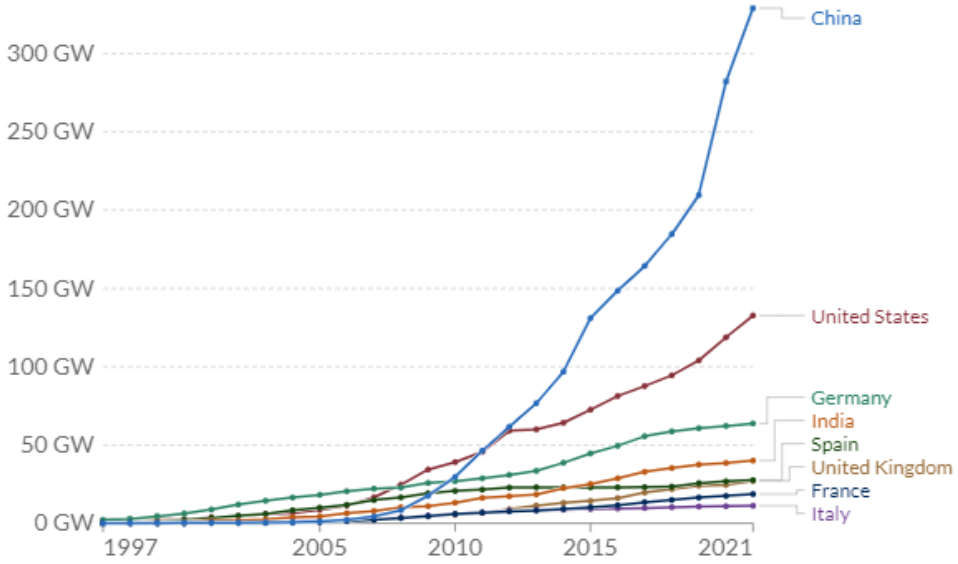

Fig. 1.2 Installed wind power capacity [9]

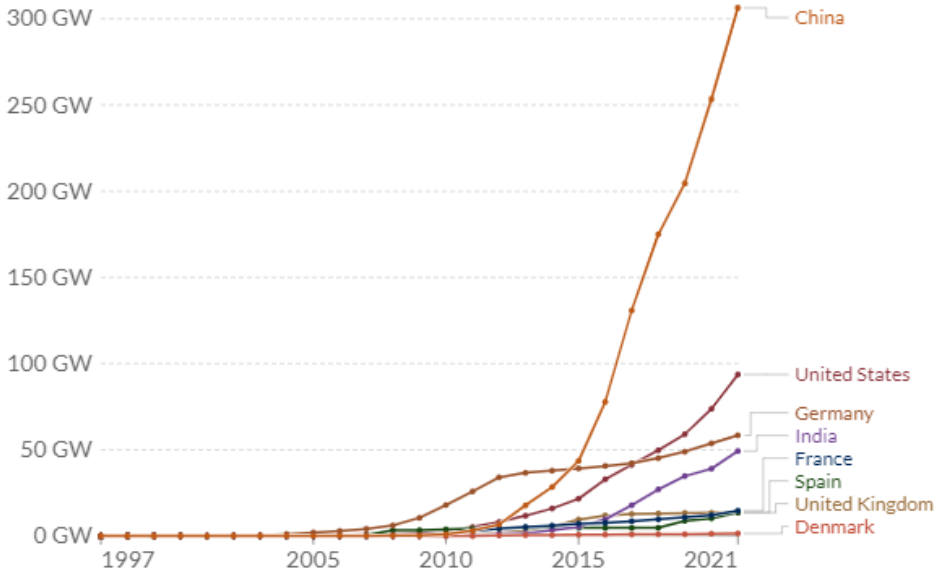

Fig. 1.3 Installed solar power capacity [9]

1.2 Future power system challenges

With the world moving to carbon neutrality, new technologies regarding the use of the increasing penetration of renewable energy, including generation, consumption, power transmission and distribution, and network topology, etc. need to be developed and understood in terms of their impact on the power system. There are several key issues to

be resolved considering the increasing demand from the utilities for more efficient, stable and reliable power systems.

1.2.1 Converter-dominated network

The conventional power generation plants in the existing power systems use synchronous generators (SGs) to connect to the rest of the system. However, renewable energy resources, especially wind and solar, utilise fundamentally different technologies for energy conversion and interfacing to the power system. All solar and most wind turbines are connected to the power grid through power electronic converters [10], [11]. Hence, the future power systems will be converter-dominated.

A power electronic converter consists of a variety of configurations of power switches and passive components, and a control system [12]. The control system establishes the gating signal for semiconductor switches through a proper control scheme to accomplish the energy conversion. Hence, an effective control system is required to regulate the energy flow from the generation source to the AC network. In contrast to SGs, power electronic converters are strictly electronic and do not contain any mechanical components [10]. As a result, they do not inherently provide the physical properties of SGs used in conventional power generations. This will arise a series of issues, including inertia and frequency stability, system strength and voltage stability, islanded operation, fault and disturbance ride-through.

Voltage source converter (VSC) technology is the most extensive solution for connecting renewable energy generation to power grid [13], [14]. Fig. 1.4 displays the structure of IGBT valves based two-level VSC. A typical VSC system operates at a high switching frequency by using pulse width modulation (PWM) to allow the conversion between DC and AC while maintaining a constant polarity of the DC voltage [15], [16]. The direction of power flow can be changed by reversing the direction of the current. It should be noted that all the converters in the rest of this thesis refer to VSCs.

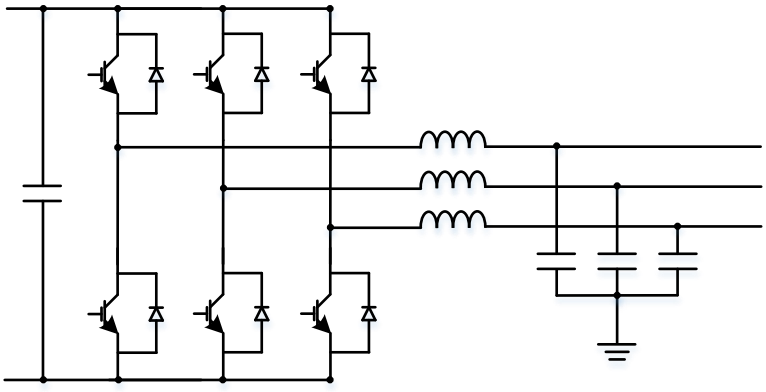

Fig. 1.4 Structure of a two-level VSC

SGs used for conventional power plants are interconnected through transmission and distribution system to provide reliability of electricity supply [10]. Hence, the existing AC power systems largely rely on the physical support of SGs to provide grid stability. However, to decarbonise the electricity sector, renewable energy resources with electric energy storage are rapidly developed and deployed for power generation, while conventional power plants using SGs are being decommissioned. As renewable energy generation is electronically coupled [17], the control design of the power electronics converters is crucial for the stability of future networks [18]. Renewable energy generation is required to control the system voltage and frequency, ride through faults and disturbances, whereas seamless transition from grid connected mode to islanded mode may also be required for some applications. Although renewable energy resources are usually connected to the power system through multiple AC-DC (e.g., wind energy), DC-DC (e.g., solar energy) and DC-AC converters, the main focus in this thesis is on the final stage that converts DC power to grid-compatible AC power (inverter-based resource or converter-interfaced generation) which interacts with the AC power system directly.

1.2.2 Power system stability

As aforementioned, with the large amounts of SGs being replaced by power electronic converters, the future power system will be the converter-dominated. Unlike SGs, power electronic converters do not contain mechanical components, e.g., stationary stator and rotating rotor. Accordingly, the mechanical properties owned by SGs will not be exhibited in the future power system. In additional, the dynamic responses of power electronic

converters are also different from SGs [19]. Eventually, it can often raise issues related to the power system stability in terms of frequency stability, voltage stability, rotor angle stability, resonance stability and converter-driven stability.

A. Frequency stability

At the view of physics, SGs can provide mechanical inertia on its rotating mass. The frequency stability relies on the total amount of mechanical inertia and speed regulation/frequency modulation control of SGs in the network. However, the input power of the prime mover is almost decoupled from the output electromechanical power of the grid side resulted from the interface of power electronic converters, which makes the power electronic converters do not own the traditional inertial response characteristics based on rotational kinetic energy [19]. Hence, system frequency stability problems can be arisen.

Specifically, when a grid disturbance occurs, the inertia slows down the frequency deviation and the kinetic energy stored in the rotating mass is released before the prime frequency controller to activate to limit the frequency deviation. Hence, the displacement of SGs with power electronic converters in future power system can result in high rate of change of frequency (ROCOF) and large frequency deviation (high frequency nadir) to be followed by tripping of relay and unintentional load shedding [20], which requires a fast acting controller to arrest frequency drop as soon as possible [21].

B. Voltage stability

It is essential to maintain voltages at all buses at the acceptable levels for a power system [10].Hence, the voltage stability can also be challenged due to the displacement of SGs in the future power system, reducing the amount of available voltage sources and reactive power capability. In this context, the voltage support given by the SGs is decreased, which stresses the voltage stability at all buses of the grid [22]. Consequently, voltage collapse can be caused by the reactive power instabilities. The voltage instability issues can be more obvious and severe during weak grids.

Since renewable generation units are usually located far from the main AC grid in order to achieve abundant wind and sun [23], [24], [25], high impedance can occur in the grid with long electric power transmission distance, which can lead to larger voltage dips with massive active and reactive power flow [26]. Typically, grid strength is defined by Short Circuit Ratio (SCR) as [27], [28]:

$$\mathrm{SCR} = \frac{1}{\left|Z_{sp.u.}\right|} \tag{1.1}$$

where $Z_{sp.u.}$ represents the grid impedance seen at the point of common coupling (PCC). With consideration of (1.1), the grid with high impedance corresponds to a low SCR and vice versa. The AC grid is classified to be "weak" with an SCR lower than 3, while it is defined to be "very weak" with an SCR lower than 2 [29], [30]. Hence, a long transmission distance can lead the interfaced grid to be weak, while a weak grid is more vulnerable to a sudden change (e.g., power, voltage and frequency) in operating conditions. In contrast, a strong AC grid has a more robust capability of withstanding any sudden changes in operating conditions [28], [31], [32]. SGs in conventional power grid can enhance the system strength locally [33], while with fewer SGs connected in the future, it will arise system instability issues.

As aforementioned, the future power systems will tend to be weak with reduced SGs and long transmission distance. In this context, the small signal stability may be a problem for the power electronic converters, which requires further analysis and investigation. The detailed assessment on the small signal stability studies will be introduced in Section 2.3.

C. Rotor angle stability

Rotor angle stability is the ability of SGs (or generation sources) to maintain rotor angle (also known as power angle) within stable boundaries to stay stable and remain in synchronism when disturbances occurs [10], [26], [34]. If the electromechanical torque vector is equal in magnitude but opposite in direction to the mechanical torque generated by the prime mover, the machine is staying in synchronism [21]. The high-penetration of power electronic converters rapidly changes the transmission system loading patterns,

which can influence the system synchronising torque [35], [36]. In addition, the risks of power oscillation can appear locally, and hence severely damage the SGs [26].

D. Resonance stability

The resonance occurs generally when the energy exchange takes periodically in the form of oscillations [21]. It normally appears with two categories, i.e., torsional resonance and electrical resonance. The torsional resonance refers to the oscillatory instability that is caused by the torsional interactions between the mechanical system of the rotating component and the electrical power grid with the series compensated lines and other converter-based equipment [19]. These oscillations are mainly sub-synchronous oscillations (SSR) that can be poorly damped or undamped, which can threaten the mechanical integrity of the generator shaft [21]. Electrical resonance refers to electromagnetic oscillations due to the dynamic interaction between the power electronic converters and power grid in a purely electrical sense [19]. These oscillations are mainly classified into self-excitation SSR that appears when the series capacitor with the effective inductance of the induction generator forms a resonant circuit at sub-synchronous frequencies, and the net apparent resistance of the circuit is negative at these frequencies [21].

E. Converter-driven stability

As introduced previously, the dynamic response of future power system with high penetration of power electronic converters is intrinsically different from the conventional power grid with SGs. The power electronic converters rely on their control loops at fast response times. In this context, the wide timescale control dynamics of the power electronic converters can lead to cross-couplings with both the electromechanical dynamics of the machine and the electromagnetic transients of the power grid, resulting in unstable oscillations of the power system over a wide frequency range [37]. With higher penetration of power electronic converters, the corresponding issue can be more severe. Specifically, high-frequency oscillations can be resulted from the mutual interaction between the control loops of the grid connected converters, while low-

frequency oscillations can appear by multiple forms of interaction between the control loops of the converters and other system components [21].

1.2.3 Islanded operation

In the event of disturbances from the main grid, such as long-time voltage dip, severe AC faults and so on, a part of isolated network may have the possibility to be disconnected from the main AC grid to avoid further deterioration and become a detached portion to ensure a high reliability level, which is recognised as an island [38], [39]. As power systems become much more distributed considering the dispersion of renewable energy in nature, many more electrical islands can exist potentially. On grid connected operation, the system dynamics are largely fixed by the connected AC grid [38], with the voltage and frequency imposed by the main grid. However, when the power network becomes islanding, the system dynamics will be dependent on the generation units, control systems and load characteristics, and are normally required to regulate voltage and frequency for the power network [38]. Hence, the power converter needs to establish its own voltage and frequency to feed the local loads. As a result, the amount of the power generation will depend on the demand of the local load. Last but not least, the control system has to ensure smooth and seamless transition from grid connected operation to islanded operation.

1.2.4 Overcurrent protection

Additional challenge due to the displacement of SGs is the overcurrent protection issue, as SGs have the capability of producing up to 6-7 times rated current during faults. Unlike traditional SGs, power electronic converters respond very differently to faults [17], and can typically only supply overcurrent of 1.2 to 1.5 pu due to the thermal limits of semiconductors, insulation levels or internal protection methods [26], [40], [41]. In the event of disturbances or faults, converters have to react quickly, and the output current must be limited under an acceptable level by additional current control loop to prevent damage to semiconductor devices. Another problem comes out of the control of active and reactive currents during different AC faults. In order to remain connected to the main grid during a transient event, the electronic converters are expected to inject active and reactive currents according to the requirements in grid code to support system during and

after fault. On the other hand, during islanded operation, the injection of active and reactive current is determined by the local loads during a disturbance, which is completely different to grid connected operation. Hence, a universal current limiting controller is distinctly important for the converter-dominated renewable energy generation systems to maintain system stability on both grid connected and islanded operation.

In addition, the response of additional current limit controller to a network fault is very much dependent on the type of fault, such as symmetrical and asymmetrical faults [17]. The performance of the controller may experience a degradation during asymmetrical faults [42]. In this context, unbalanced fault currents not only increase voltage unbalance at the PCC, but also adversely affect the converter performance of fault current limiting and voltage regulation during asymmetrical faults. As a result, overcurrent stress or current harmonics might be the main concerns, which must be carefully considered [43], [44]. Thus, converters must provide effective and flexible AC fault current limit control mechanisms. Last but not least, the converters have to provide the capability of restoring normal operation quickly after the clearance of the fault.

1.3 Scope of the thesis

1.3.1 Research motivations

As discussed previously, the conventional power plants in the existing AC power systems largely rely on the physical characteristics of SGs to support the grid. However, renewable resources are coupled to the grid through power electronic converters. Hence, with higher penetration of renewable energy, SGs used in conventional power plants will be gradually replaced by power electronic converters. Consequently, this will bring new challenges and risks for future power systems with fewer or even none SGs and more power electronic converters, which must be taken into consideration as follows [11], [45], [46]:

- Fewer SGs in the power network can reduce the level of total system inertia. Consequently, the response of the system under large disturbances can be significantly affected, and the system frequency stability will be exacerbated without proper control in place.

- SGs can enhance grid strength locally. Hence, fewer SGs result in a decline of the system strength, which greatly challenges the system voltage stability.
- A large presence of SGs can inherently slow down the system dynamic changes. With the replacement of SGs by power electronic converters, system dynamic changes become significantly faster, which brings more difficulties for converters to adequately synchronise with the system. In addition, the controllers of converters must respond more robustly to the system with faster dynamics.
- SGs can safely provide a very high fault current for a short period during a fault. Unlike SGs, power electronic converters can only provide a limited overcurrent level, which requires an effective current control in place to protect the semiconductors.

To cope with the problems brought by the displacement of SGs with converter-connected renewable generations, it is necessary to build a robust control system for the converters to ensure the continuity, quality and reliability of power supply for the power system. Existing power electronic converters used for renewable generations are mostly operating as GFL converters that track the voltage angle of the connected grid to control their outputs [33], [47]. However, the GFL converters are typically based on vector current controller, which relies on stiff external AC voltages which are usually provided by SGs. As a result, the GFLs may become unstable when the power network becomes weak or islanding. Even with fast frequency and voltage support, the frequency and voltage regulations are still dependant on the services from the remaining SGs [47]. In addition, the system stability can be further deteriorated and wide-band frequency oscillation can be induced when connecting to weak grids [48]. In recent years, the concept of “grid-forming” has been more popular and feasible for VSCs, which is considered as the key for the future power systems with high renewable penetration [33]. In contrast to GFL converters, GFM converters actively control the frequency and output voltage to improve the stability of converter-dominated power systems [49]. The desirable functionalities of GFM converters can be expressed as follows [33]:

- GFM converters can work as AC voltage sources to support the operation of the connected network with respect to its internal physical limitations, while it works

autonomously to provide voltage and frequency for the system when the network becomes islanding.

- Unlike SGs, the GFM converter can operate stably on a defined minimum system strength. When the connected grid is weak or very weak, the GFM converter has the capability of supporting the grid and other GFL converters connected in the grid.
- During transient events, the GFM converter can provide a specific operation with respect to its own limits. Once the grid returns to its normal condition, the GFM converter restores its normal operation quickly and autonomously.

Currently, the existing GFM converters, operating as voltage sources rather than current sources, mainly focus on the establishment of frequency and voltage for the power system, which results in certain limitation that the converter output current is not well regulated during large transients. Consequently, it brings challenges for the GFM converters to limit and control the current during abnormal grid conditions, such as external AC faults and overloaded operation, etc. Another type of GFM converter is based on the emulation of the inertial response like conventional SGs. This method helps enhance the system stability but fails to take advantage of the naturally fast response of VSCs to improve system dynamics [47].

Thus, this thesis aims to investigate the control and operation of GFM VSC under various grid conditions including normal grid, weak grid, islanding, overload and different external AC faults (grid connection and islanding, symmetrical and asymmetrical). This thesis mainly focuses on the development of control methods for the GFM VSC to ensure secure and reliable operations under various grid conditions mentioned previously. Small signal models will also be developed to for the system stability analysis.

1.3.2 Research contributions

The main contributions of this thesis can be summarised as follows:

- General GFL and GFM control strategies are investigated to analyse the performance and operation under different grid conditions.
- A universal GFM control strategy is proposed for the VSC to provide stable and robust operations on both grid connected and islanded operation. The converter works as a controlled AC voltage source to regulate the active and reactive power flowing to the grid and local load on grid connected mode, while it establishes the voltage and frequency during islanded mode. With a proposed current limit control, the universal GFM VSC has the capability of effective fault current limiting and distribution of active and reactive current on both grid connected and islanded operation.
- The GFM control strategy is improved with an enhanced AC fault current limit control scheme built on double synchronous frames for the VSC to ensure stable operation when connected to a weak grid. With a negative-sequence current controller, the VSC has the capability of dealing with asymmetrical AC faults and can restore normal operation quickly.
- Small signal models of the GFM and GFL VSCs are developed to conduct the impedance-based stability analysis when the converters are connected to weak networks. The admittances in the pn reference frame are derived to simplify the analysis. Based on the admittances in the pn reference frame, the GFM VSC is proved to operate more stably, and have the ability to support the operations of the GFL VSC on weak networks with specified SCRs.

1.3.3 Thesis organisations

This thesis is organised as follows:

- In Chapter 2, a comprehensive assessment of GFM control methods is stated. To enable GFM converters with the overcurrent capability, multiple current limiting techniques are introduced. To compare the small signal stability between the GFM and GFL converters, two stability assessment methods are also briefly reviewed.

- In Chapter 3, the control of GFM and GFL converter are studied. For the conventional GFL converter, the modelling and basic control schemes including PLL, vector current control and different outer control are introduced. For the typical GFM converter, the modelling and control schemes including power droop and voltage control are discussed. Simulations in MATLAB/Simulink are then carried out to validate the operations of conventional GFM and GFL control strategies.
- In Chapter 4, the overall control requirements for a universal GFM VSC are presented. The universal GFM control scheme, including GFM direct voltage control, adaptive power droop control, PLL, frequency droop control, is developed for the converter operating on both grid connection and islanding networks. An additional current limit controller is added to ensure the VSC to have the ability of fault ride-through for both grid connected and islanded operation. Simulation results in MATLAB/Simulink environment are used to verify the proposed control strategy under different grid conditions.
- In Chapter 5, a GFM VSC with an enhanced AC fault current limit control is developed to enable the converter to operate during symmetrical and asymmetrical faults. The control scheme is built on double synchronous frames to realise the separated control for positive- and negative-sequence voltage and current. The enhanced fault current limiting method is proposed for the overall fault current limiting and distribution of active and reactive current. To control the negative-sequence component current and facilitate the detection of asymmetrical faults, a negative-sequence current control scheme is also developed. Simulation results in MATLAB/Simulink verify the feasibility and effectiveness of the proposed control strategy under various fault conditions.
- In Chapter 6, a small signal model of the GFM VSC connected to a weak network is developed. Based on the developed small signal model, the total admittance including the GFM controller, filter, transformer and grid impedance in the system dq reference are derived. The admittance in the system dq reference frame is then transformed to the admittance in the pn reference frame for further stability analysis. Based on the obtained admittance, the stability improvement with the GFM VSC

on weak networks is validated by using Nyquist stability criterion. The effectiveness of the admittance derived by the small signal model is verified by the time-domain simulations in MATLAB/Simulink.

- In Chapter 7, the conclusions of the research are drawn and future work is recommended.

Chapter 2 Literature Review

In this chapter, a comprehensive assessment of the GFM control methods is stated firstly. To provide the ability of overcurrent protection for GFM converters, several current limiting techniques are reviewed subsequently. Finally, two categories of stability analysis approach including eigenvalue-based and impedance-based method are discussed.

2.1 Control methods of GFM converters

As discussed in Chapter 1, the future power system will be converter-dominated with high penetration of renewable energy generations. Broadly speaking, grid connected power electronic converters can be divided into two categories depending on the controllers and operations [10], [50], [51], i.e., GFL and GFM converters.

2.1.1 Comparison of GFL and GFM converters

A GFL converter has a control approach that regulates the power flowing to the interfaced power grid by following an established external power system. At the core of its operation, the converter is synchronised to external network voltage during operation, which forms the concept of "grid-following". Phase-locked loop (PLL) is normally utilised for the estimation of the instantaneous voltage angle at the terminals to be followed by GFL converters in real-time [10]. It is noticeable that GFL converters merely perform as voltage-following current sources and rely on stiff external AC voltages that maintain minimal amplitudes and frequency deviations [10], [47]. However, a stiff AC voltage is traditionally based on the collective behaviours of the SGs in which the system controllers and voltage regulating equipment provide a stiff voltage amplitude and frequency at any point of the grid [10]. Hence, it becomes challenging for GFL converters to maintain adequately voltage and frequency stability when the grid becomes weak with less stable grid voltage. With further displacement of SGs, the system dynamic changes become faster, which can result in the converters failing to adequately synchronise with the grid, such that a small disturbance can lead to a significant performance reduction. To address this issue, the converter control system is required to respond robustly and quickly

in case of any output disturbance. Furthermore, it is difficult for GFL converters to fulfil the requirements with the possibility for islanded operation in the future power system as there will be no external grid voltage to follow during this period.

To address the above issues brought by GFL converters, it is necessary to develop alternate converter control strategies to enable the transition to a converter-dominated power system. In recent years, GFM converters, intrinsically different from GFL converters, are seen as the key enablers for high renewable penetration in future power systems [33]. GFM converters have a control approach that actively controls their voltage and frequency outputs [47], [52], so as to form the grid voltage by the converters with support of energy storage and reserve [53]. Depending on the conditions and characteristics of the power systems, GFM converters can act as the slack-bus to establish its own voltage and frequency for islanding networks, or a power source to provide voltage and frequency support by adjusting the generated instantaneous active and reactive power for connected AC grids. In addition, with active frequency control, the dependence of the frequency dynamics on the mechanical inertia provided by SG can be decreased [47].

Some type of GFM converters can create virtual inertia by emulating physical phenomena through a special control design to enhance the dynamic response of the entire power system. Due to the extra technical requirements and costs associated with GFM converters [54], GFL and GFM converters will coexist in future power systems and hence, GFM converters should undertake the responsibility to support the operation of the GFL converters.

2.1.2 Conventional GFM control (self-synchronisation)

Conventional GFL converters use the PLL to synchronise with the grid. However, the operation of PLL relies on a stiff external voltage. As discussed previously, the growing displacement of SGs can deteriorate the operation of PLL. As investigated in [55], PLL may bring positive feedback when the grid impedance is high, resulting in an unstable system. Hence, many GFM converters remove PLL from their control schemes. The idea of self-synchronised/conventional GFM control algorithm is to utilise active power-

frequency and reactive power-voltage droop controllers to control the phase angle and voltage [56], [57]. Examples of the characteristics of the droop controllers are depicted in Fig. 2.1. Therein, ω_0 and V^0 represent the nominal values of the frequency and voltage magnitude, respectively.

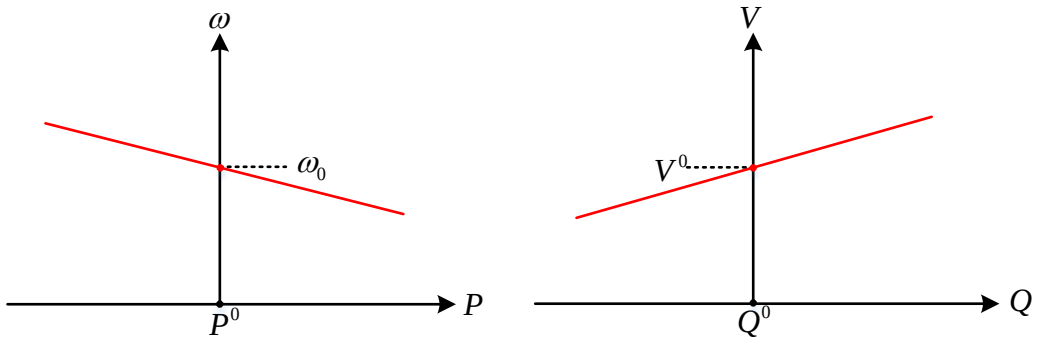

Fig. 2.1 Droop characteristics

Generally, the droop control mechanism regulates the active power by controlling the angular speed (frequency), while the reactive power is regulated by controlling the voltage amplitude. The droop controllers enable the converter to work on both grid connected and islanded operation due to the set of voltage and frequency. Instead of using PLL, the synchronisation algorithm is accomplished by the frequency-active power loop. The detailed model and design of the GFM VSC with droop controllers to control the voltage and phase angle will be discussed in Chapter 3.

As introduced in [53], the conventional droop control is improved to directly imitate the control system of a SM, which is firstly referenced as “self-synchronisation”. The control block diagram is depicted in Fig. 2.2 with the time constant of T_m and T_e for the low-pass filters. The reactive power loop produces the voltage reference V^* to be tracked by the measured voltage V through a PI regulator [53], while active power loop generates the system angular frequency ω to output the phase angle θ. As seen, an additional angle feedback proportional to the active power deviation with a proportional gain k_{pp} is added compared to the conventional droop control.

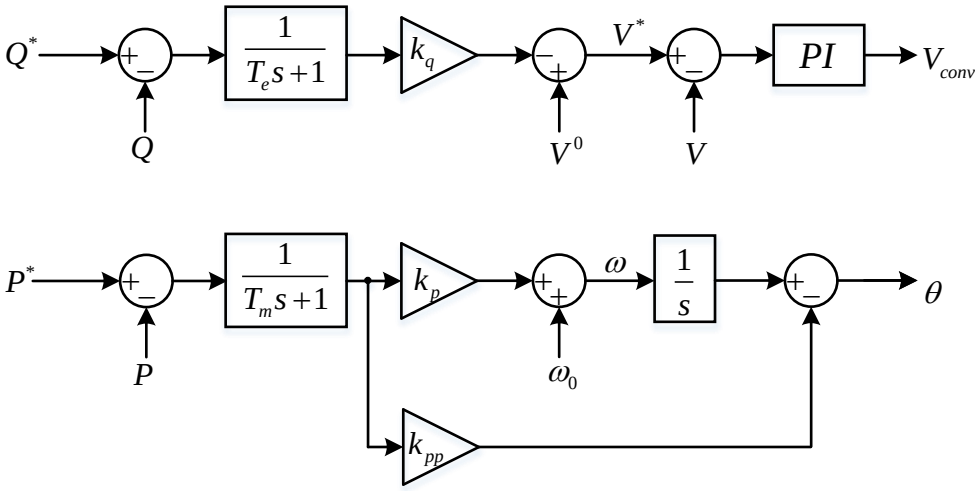

Fig. 2.2 Diagram of self-synchronised droop control

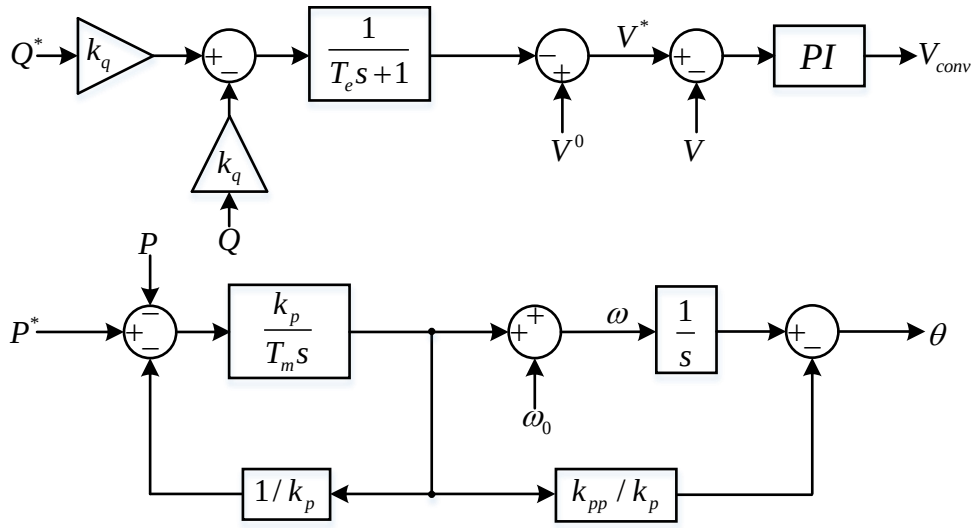

Fig. 2.3 Rearranged diagram of self-synchronised droop control

By rearranging the control parameters, a control diagram similar to a 3rd-order SM model discussed in [53] and [58] can be developed as shown in Fig. 2.3. The reactive power-voltage loop is equivalent to the internal voltage loop composed of the excitation voltage and reactive current with the reactive droop coefficient corresponding to reactance difference between the synchronous and transient value. The time constant T_e corresponds to the open-circuit time delay. Likewise, the active power-frequency/angle droop is equivalent to the model of swing equation with T_m / k_p and $1/k_p$ corresponding to the inertia constant and mechanical damping factor. Consequently, this method

provides adequate virtual inertia and damping to enhance the system stability and transient performance compared to conventional droop control. In addition, for the reactive power loop, the inner voltage controller may be removed, and then the modulation voltage is simply given as $V^*\angle\theta$. On the contrary, the converter filter bus voltage can track the voltage reference $V^*\angle\theta$ with the inner voltage control loop. Despite the increased complexity with the inner control loop, it still brings some merits, such as improved control reliability and accuracy. However, the absence of effective current control causes the converter to lack the capability of fault current limiting. Even with instantaneous current limit control loops stated in [18], [42], [59], [60], [61], the output can be distorted with high harmonic components due to crest clipping of the input sinusoidal signal. Meanwhile, it is difficult to control the fault current considering the requirement for fault detection during asymmetrical AC faults.

2.1.3 Virtual synchronous machine/generator (VSM/VSG) control

In conventional power systems, the major portion of electricity demand is supplied by SGs that provide inherent inertia and damping properties to enhance system stability [62]. Thus, the most straightforward approach is to directly emulate the SG to apply virtual machine algorithm in the controller of a converter, which forms the concept of virtual synchronous machine/generator (VSM/VSG). The first concept of VSM is labelled as VISMA in [63], which combines the dynamic converter technology and entire static and dynamic properties of SMs. As shown in Fig. 2.4, the VISMA consists of generation units, energy storage, a converter with SM model applied in the controller and a hysteresis current controller. The voltage at the PCC is measured to feed the SM model which performs the mathematical model of an electromechanical SM [64], [65], and then the stator currents of the VSM are obtained. Subsequently, the calculated stator currents are used as the reference current signals to compare with the measured phase currents by the hysteresis controller for the purpose of generating the switch signals for the converter. It is obvious that the VISMA's performance is dependent on the reference/calculated currents that come from the VSM model. Hence, the performance of the VISMA is influenced by the modelling precision of the synchronous model directly [64]. Like SMs, the VISMA adapts the reactive and active power flowing into the grid by adjusting the

converter output voltage and frequency. However, the tuning for VISMA is extremely difficult as it is a complex model. Meanwhile, the ability of the VISMA to damp oscillations has still not fully explored [66].

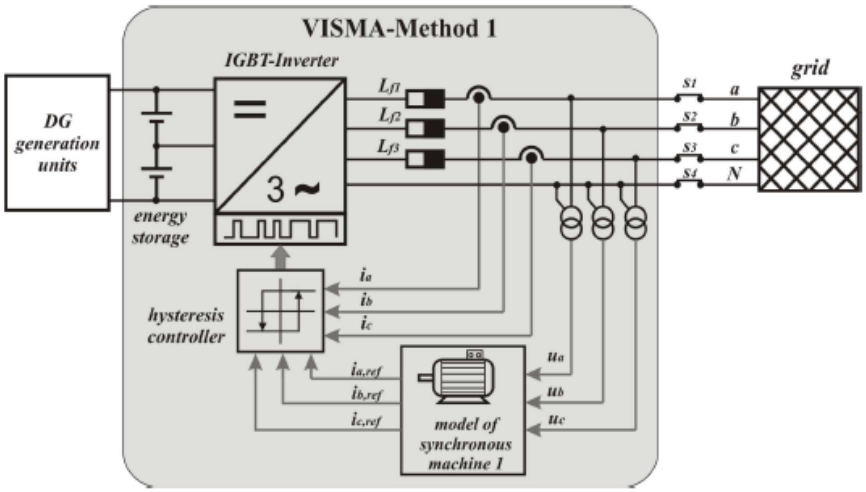

Fig. 2.4 Structure of the VISMA [67]

Another well-known method of VSM is the synchronverter in [68]. It also emulates the behaviour of a SM by specifying the controller of the converter. Energy storage devices are also necessary on the DC bus to ensure adequate power from the imaginary prime mover and virtual inertia on the imaginary rotating mass. The control strategy is based on the swing equation and mathematical equations for coupling the virtual rotor and stator [53]. Active power is regulated by the frequency droop controller with the frequency droop coefficient as the virtual mechanical friction coefficient, while reactive power is regulated by the voltage droop controller with the voltage droop coefficient. There are several further developments of synchronverter. In [69], a self-synchronverter is developed to shorten the time of synchronisation and improves the accuracy of synchronisation by taking away the dedicated synchronisation unit. To improve the damping and dynamic response speed of the active power control, an auxiliary control loop from the virtual flux to active power is added in [70]. All the synchronverter designs inherit the advantages of SGs, but also have the disadvantages of SGs, e.g., loss of stability due to lack of excitation and oscillations around the synchronous frequency [68].

Furthermore, the system inertia response can be deteriorated with the damping improved [66].

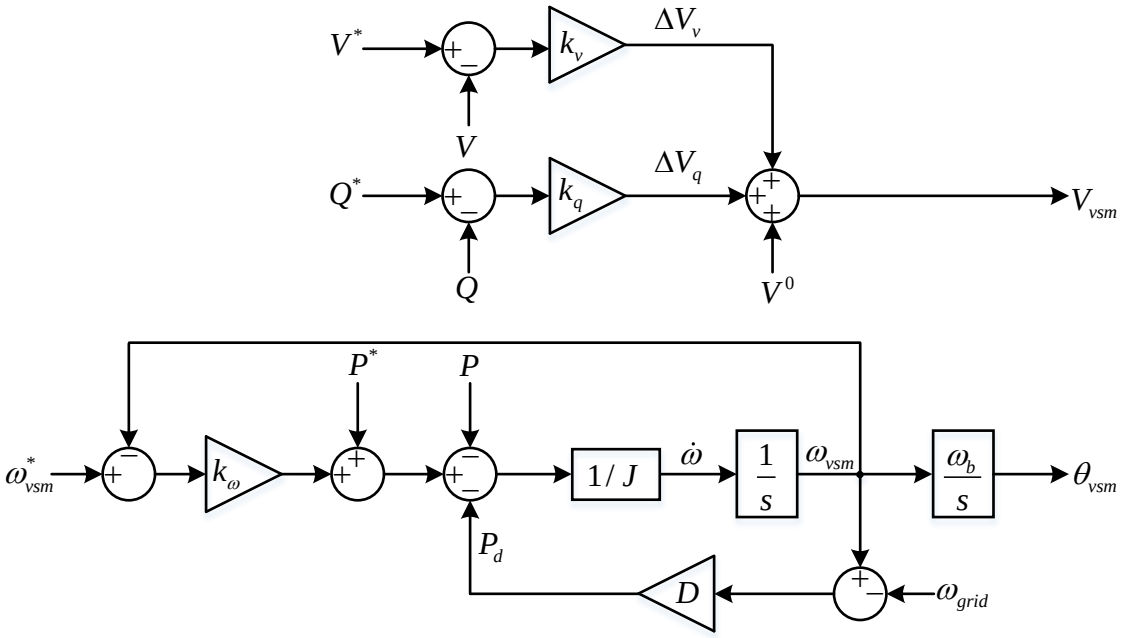

Fig. 2.5 Diagram of VSM control technique

The most extensively utilised and promoted implementation of VSM/VSG is to combine the swing equation with droop mechanism for inertia emulation, voltage and frequency regulation, and synchronisation algorithm [71], [72], as shown in Fig. 2.5. As seen, the active power loop emulates the inertia and mechanical damping of a traditional SM, while the outer frequency droop control loop corresponds to the steady-state characteristics of the speed governor of a traditional SM [72]. The reactive power-voltage control loop mimics the excitation regulation function of a SM, which is supplemented by an extra voltage loop to realise the droop characteristics between the voltage amplitude and reactive power [73]. However, the same issues to the use of self-synchronised GFM VSC occur due to the lack of current limiting control loop. In addition, the emulation of virtual inertia means that the system does not take advantage of much faster converter response to improve system dynamics [47].

2.1.4 Power synchronisation control

Another GFM technique is the so-called power synchronisation control as shown in Fig. 2.6, which was firstly introduced in [74]. In essence, it is similar to the previous described GFM designs that use voltage and angle to control the reactive and active power directly as displayed in Fig. 2.7.

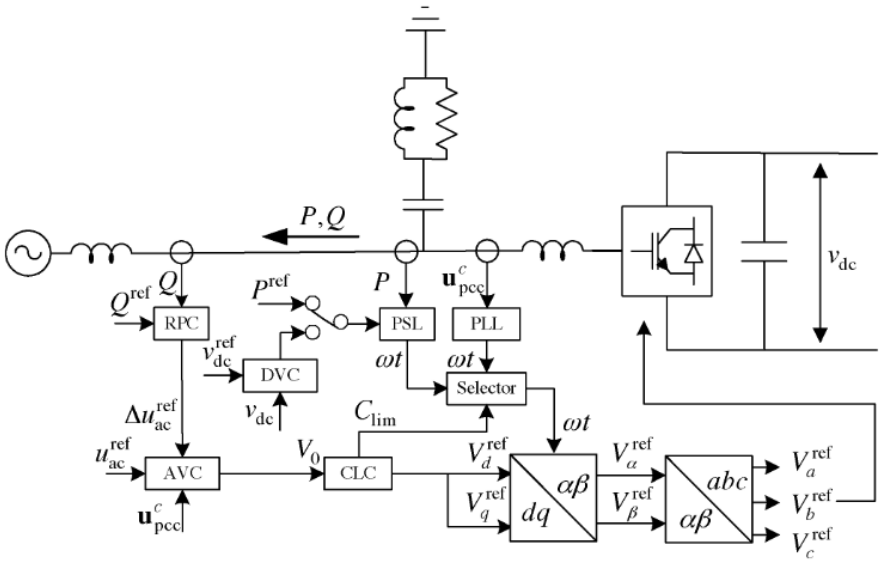

Fig. 2.6 Diagram of VSC based on power synchronisation loop [74]

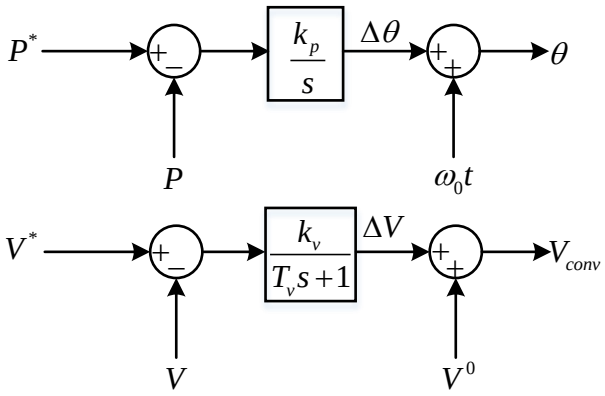

Fig. 2.7 Diagram of power synchronisation control loop

With consideration to the angle regulation loop, it not only accomplishes the synchronisation between the VSC and AC grid, but also acts as an active power control loop. As for the voltage regulation loop, it has a droop characteristic due to the

proportional controller [53], [74]. The VSC uses power synchronisation control performs almost in the same way as a traditional SM. Hence, it provides sufficient voltage support to improve the capability of power transfer on a weak grid. As the power synchronisation control maintains synchronism by a transient power transfer, an unknown current determined by the interconnecting network will be involved [74]. Hence, the power synchronisation mechanism has conflicts with current control. To limit the current during external AC faults, it switches to a current limitation controller to prevent the converter form overcurrent damage. In this context, a backup PLL is switched in to keep the VSC synchronising with the AC grid. However, such a control mode switching increases the complexity of the system and may cause the system to be unstable. The detailed current limiting control will be described in Section 2.3.

2.2 Current limiting control

For all the different control methods of GFM converters, the most common problem facing them is the lack of capability of fault current limiting. Conventional GFL converters have the ability to limit and control fault current due to the inherent internal current control loop. Although GFM converters imitate the characteristics of SGs, they are much more sensitive to transient disturbances due to limited overcurrent and overvoltage capability of the semiconductor devices. However, GFM converters are required to ride through network faults and large disturbances, while in the meantime, provide grid support during such transient events. In order to protect the GFM from overcurrent and ride through the transient disturbances, an additional current limiting control loop is essential. Due to the existence of the additional current limiting control loop, the response of the converter during an external AC fault is dependent on the type of fault [17], such as faults during grid connection and islanding networks, symmetrical and asymmetrical faults, etc. This brings a big challenge to assure fault-resiliency for the GFM converters. There are several control strategies considering the fault current limiting of GFM converters, which are reviewed in this subsection.

2.2.1 General current limiting techniques

In this section, several current limiting techniques are discussed. The most straightforward way is to switch the GFM control scheme to the GFL control scheme once the current threshold is exceeded during a fault, e.g., the previously discussed power synchronisation control [74]. In this scenario, the system loses all functionalities of GFM and the outer power loop saturates. When the fault is cleared, it switches back to the GFM control scheme. The method of control mode switching has also been applied for other type of GFM converters, such as synchronverter [75], VSM [76], [77], and conventional GFM [78], [79]. During a transient overcurrent event, the GFL control scheme controls the current by limiting the current at a pre-designed value directly. However, this can cause wind-up in the outer power loop [80]. Subsequently, the system can lose synchronisation with the power network when the power angle exceeds the critical clearing angle under the voltage sag, leading to instability. In addition, large transient current may occur at the moment of the control mode switching, which can potentially damage the semiconductor switches.

Another approach to deal with the overcurrent issue for GFM control is to employ nested control loops (also named cascaded control loops) as shown in Fig. 2.8, which is discussed in [81], [82]. The control plant can be perceived as two first-order systems [83]. The inner current control is used to control the converter output current via a PI regulator. The current reference generated by the voltage control loop is limited through a limiter to avoid excessive fault current during an external AC fault as depicted in Fig. 2.8. The current reference is given as:

$$I^* = \begin{cases} -I_{\text{lim}}, & I^* \le -I_{\text{lim}} \\ I^*, & otherwise \\ I_{\text{lim}}, & I^* \ge I_{\text{lim}} \end{cases} \tag{2.1}$$

where I_{lim} is the maximum permissible current threshold, which can be used to limit each phase independently. The controller can be applied in the natural abc frame [84], [85], rotating $\alpha\beta$ frame [41], [79], [86] and synchronous dq frame [17], [81], [82], [83], [87], [88]. The nested control loops provide a relatively fast response. In addition, the transient

response in the case of a load disturbance is further improved [83]. However, there are still some weaknesses while applying this control scheme. A well-perceived weakness is the risk of instability on weak grids [74], [89], since it assumes that the grid strength is adequate and the impact of the converter to the grid is neglected [90], [91]. Such assumption has been proved invalid due to the constraint of power flow and small signal damping [90], [92], [93]. Furthermore, while the controller is applied in the abc or $\alpha\beta$ frame, distorted converter bridge current can be simultaneously generated, which seriously affects the controllability of the system. Another weakness is resulted from the saturation of voltage control loop during a fault, which also makes the converter lose all the functionalities of the GFM control. In addition, the saturation of voltage control loop can lead to postfault instability issue as the integral keeps accumulating errors and causes wind-up during this period.

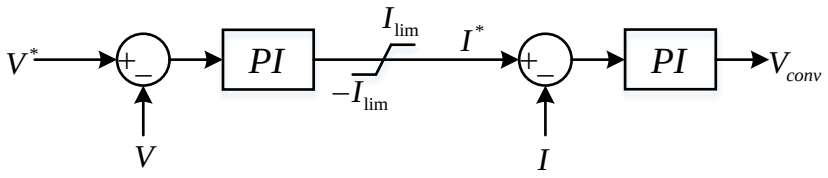

Fig. 2.8 Nested voltage and current control loops

To deal with the saturation of voltage control loop during faults, additional virtual impedance can be employed to limit the voltage reference as investigated in [82], [84], [86], [94]. The general principle of this method is to add a virtual impedance between the converter and the grid once the converter output current exceeds a certain current threshold I_{th}. The equivalent circuit of a GFM converter with the virtual impedance current limiting strategy is depicted in Fig. 2.9. During an external fault, the virtual impedance is inserted into the control system. The reference voltage applied to the converter filter bus can be derived as follows:

$$V^{**} = V^* - Z_{vir}\left(I - I_{th}\right) \tag{2.2}$$

where V^* is the original reference voltage and V^{**} is the corrected reference voltage by the virtual impedance, while I refers to the actual current flow and Z_{vir} represents the inserted virtual impedance. Depending on the control requirements, the virtual impedance

can be a pure resistance or reactance, or both. The control diagram is illustrated in Fig. 2.10. By reducing the voltage reference, it retains the voltage control loop, hence the functionalities of the GFM control. However, the performance of this method is sensitive to the grid impedance [79], [95]. In addition, the aforementioned risk of instability issue on weak grids still exists as the inner current control is remained.

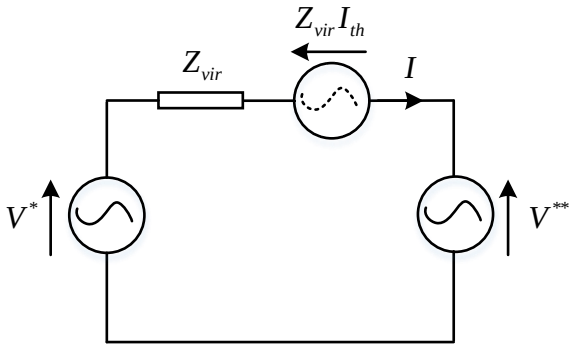

Fig. 2.9 Equivalent circuit of a GFM with the virtual impedance current limiting strategy

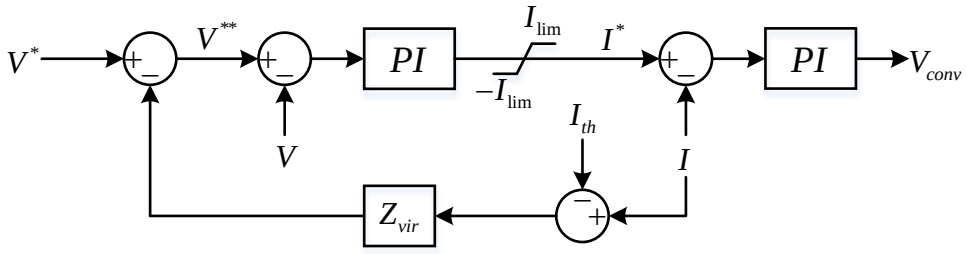

Fig. 2.10 Nested voltage and current control loops with virtual impedance

2.2.2 Unbalanced condition

The presence of unbalanced network condition (e.g., during asymmetrical faults) not only gives rise to the output power fluctuation of the converter, but also increases the output current harmonics and voltage distortion at the PCC if adequate converter control is not in place. The current harmonics can significantly influence the reliability of the system, while the power oscillations may affect the continuity of power supply [96]. According to [97], the majority of AC faults are unbalanced. During an asymmetrical AC fault, negative-sequence current components will occur, so one solution is to control the positive- and negative-sequence current components separately once an asymmetrical fault is detected, which can be realised in the synchronous (dq) reference frame as

displayed in Fig. 2.11 (a). The control design for inner current loop under asymmetrical faults in the double decoupled dq reference frames is introduced in [40], [98], [99]. The current references can be set as the requirements in the grid code. In this method, the parameters of the PI regulators for the positive- and negative-sequence controllers can be set individually, which provides sufficient control flexibility. However, PI regulators have relatively poor capability of disturbance rejection [100], which makes the system sensitive to any disturbance in the network. Due to the bandwidth limitation, the control system will require additional low-pass filters to remove the low-order harmonics, which can introduce a delay and make the control response sluggish during transients [101], [102].

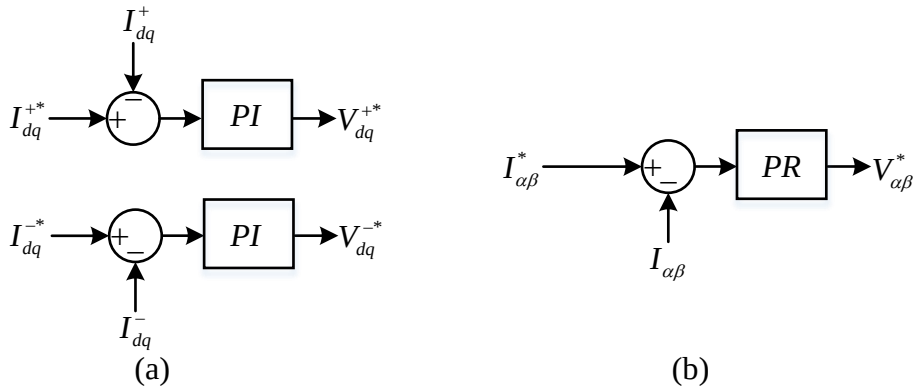

Fig. 2.11 Control architecture of current control: (a) double synchronous reference frame (b) stationary reference frame

Besides the synchronous (dq) reference frame, the current control can also be designed for the stationary ($\alpha\beta$) reference frame under asymmetrical faults [96], [102], [103], as shown in Fig. 2.11 (b). The converter current is transformed from the abc reference frame to the stationary $\alpha\beta$ reference frame using Clarke transformation. Proportional-Resonant (PR) regulators can be used to track the sinusoidal references with zero steady-state error and disturbance rejection capability [104]. However, the parameters setting of the PR regulator is complicated, which makes the parameters tuning extremely difficult.

During an asymmetrical fault, the required converter output voltage is the combination of positive- and negative-sequence components generated by the corresponding current controller. In this context, the converter output voltage may exceed the voltage limitation

if trying to maintain the positive-sequence component voltage at the nominal value [105]. As a result, overvoltage issues on the healthy phases may occur while both positive- and negative-sequence control loop will be saturated, which can lead to the over-modulation behaviour of PWM to exacerbate the controllability and performance of converter.

2.3 Stability analysis

With the increasing penetration of renewable generation in the power system and more complex control structures, the stability of the system is facing enormous challenges [106]. As time domain simulations cannot reveal the insight of the impact of system control and parameters on system stability [107], small signal model has become an important and useful tool on system stability assessment. There are two widely used stability analysis methods based on small signal model, i.e., eigenvalue-based analysis method and impedance-based analysis method. Both methods can effectively determine the stability of the system by covering the impact of dynamic controllers, grid impedance and DC line impedance [108].

2.3.1 Eigenvalue-based analysis method

The eigenvalue-based analysis method is an approach that determines the stability of a system regardless of the location of the source of instability [109]. It has been extensively utilised to analyse the stability of wind turbine systems [110], and stability of HVDC systems [106], [111], [112]. As power system is a typical nonlinear dynamic system, the equations representing the system are linearised and expressed in state-space model with consideration of a small disturbance [111]. By calculating the eigenvalues of the linearised state-space model, the small signal stability of the system can be evaluated. The impact of the system operating conditions and controllers' parameters on system dynamic performance can be analysed by observing the loci of the eigenvalues.

To compare GFM and GFL converters for a power system with high converter penetration, an example by using eigenvalue-based small signal analysis method is conducted in [47]. The system is modelled by a simple aggregated two-source reduced-order power system model to investigate the interactions between a generator and a

converter, as displayed in Fig. 2.12. The eigenvalue trajectories at varying converter penetration levels for both GFL and GFM converters are depicted in Fig. 2.13.

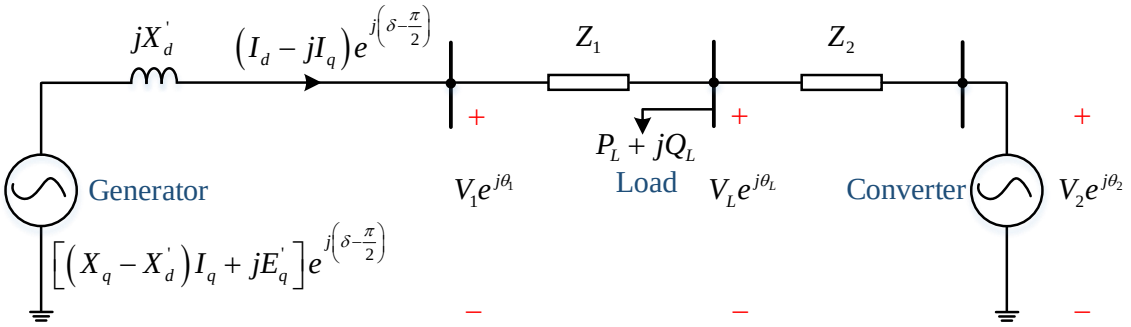

Fig. 2.12 Diagram of a two-source system model

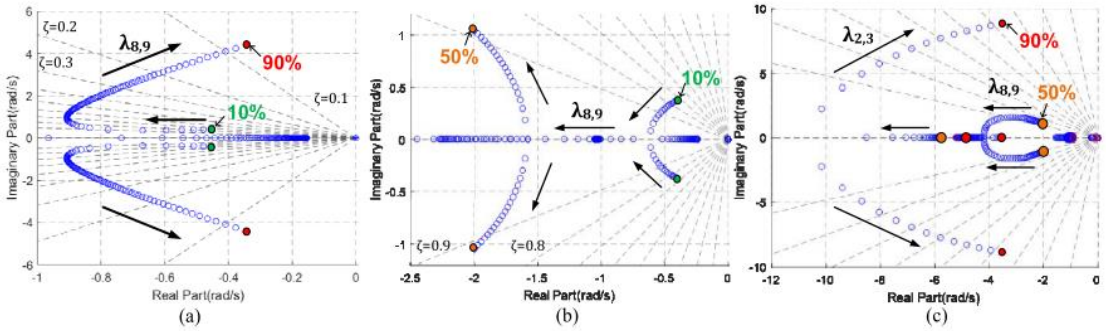

Fig. 2.13 Eigenvalues trajectories for varying penetration levels: (a) GFL converter, 10% to 90% penetration (b) GFM converter, 10% to 50% penetration (c) GFM converter, 50% to 90% penetration [47]

For the case of the GFL converter in Fig. 2.13 (a), the eigenvalues begin to move to the right with increase of the penetration level of the GFL converter, which indicates reduced damping and deteriorating stability. For the case of the GFM converter in Fig. 2.13 (b) and (c), the electromechanical modes $\lambda_{8,9}$ become better damped, which indicates much higher damping than that for the case of GFL converter. In this context, the system dynamic performance is improved with the GFM converter. By comparing the results shown in Fig. 2.13 (a), (b) and (c), the GFL converter negatively affects the system eigenvalues, hence the system stability. The GFM converter has positive impact on the system eigenvalues, hence the system stability.

2.3.2 Impedance-based analysis method

Impedance-based stability analysis method has been firstly developed to evaluate the interaction between a DC-DC converter and its input filter [113], and then became popular for the stability analysis of grid-connected converters at the interfacing point to the connected network [114], [115]. It partitions the system into a source and a load subsystem, and then the small signal stability of the system can be analysed in application of the Nyquist criterion to the ration between the source output impedance and the load input impedance [114], [116], [117]. By applying impedance-based method, the measured impedance essentially simulates all circuit components, including physical components and control systems [118]. Furthermore, it conducts a way to study interaction points and possibly undesirable operation by using easily measured quantities [119].

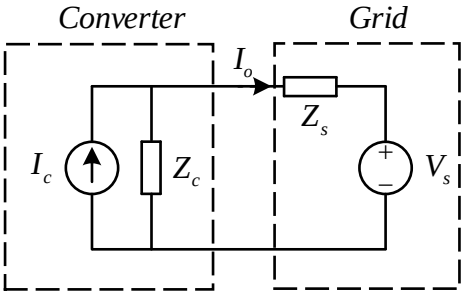

Fig. 2.14 Impedance representation of a grid connected converter system

As shown in Fig. 2.14, the grid source is modelled by a Thevenin circuit as an ideal voltage source V_s in series with a grid impedance Z_s, while the grid connected converter is modelled by a Norton circuit in form of a current source I_c in parallel with an output impedance Z_c. This can be seen as a hybrid system consisting of a voltage source and a current source [120]. The converter output current flowing into the grid can be obtained by:

$$I_o(s) = \frac{I_c(s)Z_c(s) - V_s(s)}{Z_c(s) + Z_s(s)} = \left[I_c(s) - \frac{V_s(s)}{Z_c(s)} \right] \bullet \frac{1}{1 + Z_s(s)/Z_c(s)} \tag{2.3}$$

For system stability analysis, the converter is assumed to be stable when the grid impedance is zero and the grid voltage is stable without the converter [120]. Based on

this assumption, the grid connected converter can operate stably if the impedance ratio (loop gain) $Z_s(s)/Z_c(s)$ satisfies the Nyquist stability criterion [113], [114], [120], [121]. This indicates that the output impedance is an important index for grid connected converters at the view of system stability.

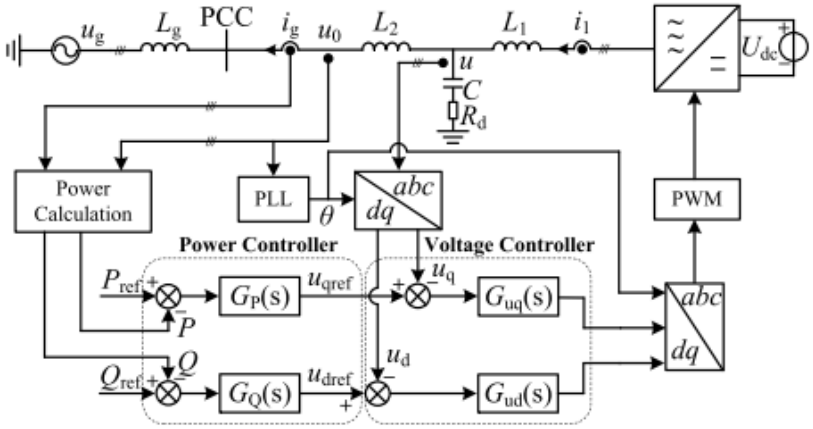

Fig. 2.15 Configuration of the power-voltage control based GFM in weak grids [122]

To compare the GFL and GFM converter on a weak grid, the stability analysis using dq impedance-based method is conducted in [122]. The system is modelled by a voltage source converter connected to a weak grid (i.e., high grid impedance) through an LCL filter, as illustrated in Fig. 2.15. The DC side is represented by a fixed DC voltage source so the impact of the DC side is neglected. As seen, the GFM converter takes the power-voltage control strategy, which adopts PI regulators. $G_P(s)$ and $G_Q(s)$ refer to the active and reactive power controllers respectively, while $G_{ud}(s)$ and $G_{uq}(s)$ represent the dq-axes voltage controllers. For comparison, instead of the voltage control loop, the GFL converter takes the power-current control strategy which employs conventional vector-current control as the inner loop.

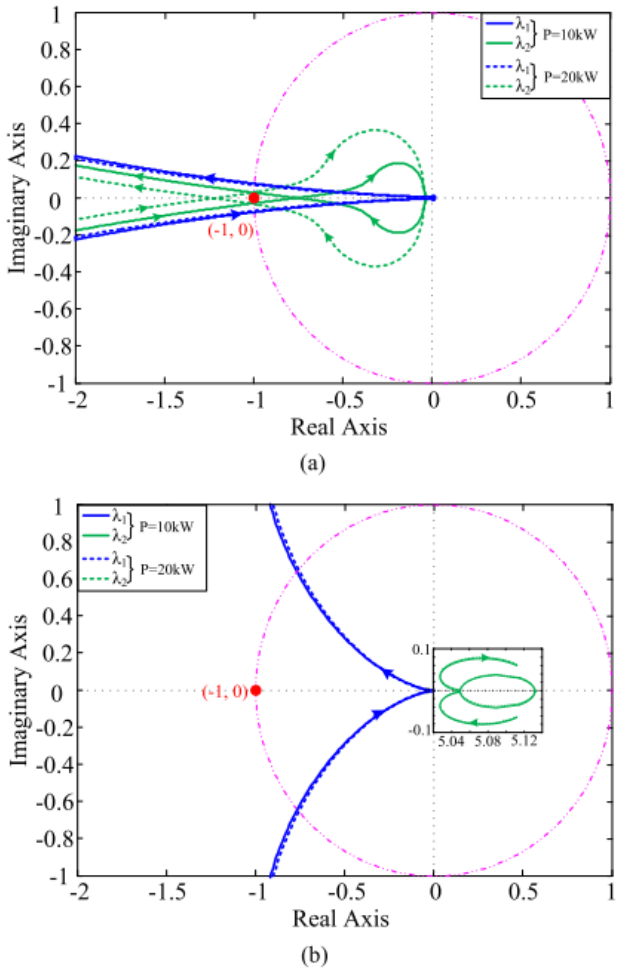

Fig. 2.16 Nyquist plots on a weak grid with an SCR of 3 (a) GFL converter (b) GFM converter [122]

The Nyquist plots of the GFM and GFL converter on a grid with an SCR of 3 are displayed in Fig. 2.16. For the case of the GFL converter with power-current control in Fig. 2.16 (a), the character loci λ_2 encircles (-1, 0) as the active power follow increases, which indicates a unstable converter system with higher active power generation. However, for the case of the GFM converter with power-voltage control in Fig. 2.16 (b), neither of the character loci λ_1 and λ_2 encircles (-1, 0) with the increase of active power flow, which indicates a stable system. Similar works have also been done to highlight the reduced stability of GFL converters on weak grids in [123], [124].

Despite the improved stability brought by the integration of GFM converters compared to GFL converters, GFM converters still suffer from stability issues. On a weak grid with

a low SCR, there are still risks of the wideband oscillations in the voltage and current waveforms that is around the grid fundamental frequency [125], [126]. On the other hand, there are also small signal stability issues for the GFM converters when subjected to grid disturbances on a strong grid [127]-[128]. On a strong grid, the biggest difficulty for the GFM converters is to regulate the voltage at the PCC [48]. As a result, both sideband oscillations (low-frequency oscillations) and synchronous oscillations (near nominal frequency oscillations) can occur to deteriorate the system stability [37].

2.4 Summary and thesis contributions

This chapter reviews the future network challenges, GFM control methods, current limiting control strategies and stability assessment methods. Different challenges and requirements resulted from the converter-dominated network, i.e., frequency and voltage stability, islanded operation and overcurrent protection, are reviewed. The GFM and GFL converters are compared, and different GFM control strategies, i.e., self-synchronisation, VSM/VSG and power synchronisation control, are introduced. Various current limiting control methods including general overcurrent limiting and unbalanced current control techniques are also discussed. In addition, to compare the GFM and GFL converters for small signal stability, two assessment methods including eigenvalue-based and impedance-based analysis methods are reviewed.

Chapter 3 Control of grid-following and grid-forming converter

Depending on the operation and control structure, power electronic converters can be classified into two categories, i.e., GFL and GFM converter [10]. The GFL converter is mainly designed to deliver active and reactive power into the AC grid, while the GFM converter is controlled as an AC voltage source with the setting voltage magnitude and frequency of the connected AC grid [50]. In this chapter, the modelling of grid connected VSC is introduced. Based on the general model of grid connected VSC, the control strategies of GFL and GFM converter are discussed. The feasibility and validity of the control strategies are demonstrated by simulation results in MATLAB/Simulink environment.

3.1 Modelling of grid connected VSC

3.1.1 General structure

Fig. 3.1 shows the simplified schematic diagram of a grid connected VSC. As this thesis mainly focuses on the performance of the AC side, the impact of the DC side of the VSC is assumed to be negligible, i.e., DC side is represented by a fixed DC voltage source. As seen in Fig. 3.1, the VSC with a fixed DC voltage source is connected to an AC grid having the grid impedance (inductance L_s and resistance R_s) through an LC filter (reactance L_f and capacitance C) which is used to suppress the harmonics resulted from the converter switching during operation [129]. A step-up transformer is used after the LC filter to boost the converter output voltage to match the connected AC network.

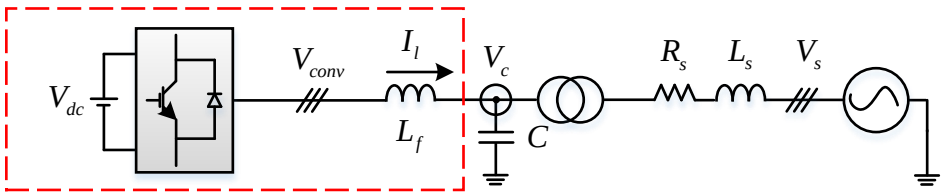

Fig. 3.1 Schematic diagram of a grid connected VSC

3.1.2 System model

The system model is built based on the part in the red box shown in Fig. 3.1, so the equivalent AC circuit of the grid connected VSC in a rotating dq reference frame at the angular speed of ω without considering the capacitor C, transformer and grid impedance (R_s and L_s) can be shown in Fig. 3.2.

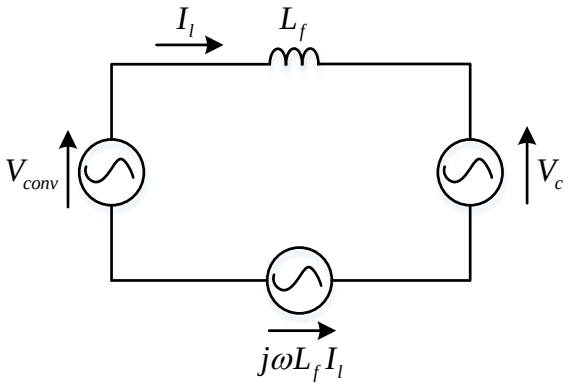

Fig. 3.2 Equivalent circuit of the grid connected VSC

According to Kirchhoff's Voltage Law (KVL), the relationship of the converter filter bus voltage V_c, the converter output voltage V_{conv}, the converter output current I_l and the phase reactance L_f in the model of Fig. 3.2 can be obtained as:

$$V_{conv} = V_c + L_f \frac{dI_l}{dt} + j\omega L_f I_l \tag{3.1}$$

Equation (3.1) can be expressed using dq-axes components as:

$$\begin{bmatrix} V_{convd} \\ V_{convq} \end{bmatrix} = \begin{bmatrix} V_{cd} \\ V_{cq} \end{bmatrix} + \begin{bmatrix} 0 & -\omega L_f \\ \omega L_f & 0 \end{bmatrix} \begin{bmatrix} I_{ld} \\ I_{lq} \end{bmatrix} + \begin{bmatrix} L_f & 0 \\ 0 & L_f \end{bmatrix} \frac{d}{dt} \begin{bmatrix} I_{ld} \\ I_{lq} \end{bmatrix} \tag{3.2}$$

where V_{convd} and V_{convq} are the dq-axes converter output voltage, V_{cd} and V_{cq} are the dq-axes converter filter bus voltage, I_{ld} and I_{lq} are the dq-axes converter output currents.

3.2 Control of GFL converter

Conventional GFL converters are used to deliver power to an energised AC grid, and can be typically represented as controllable current sources with relatively high output-impedance connected in parallel as shown in Fig. 3.3 [50]. As depicted in Fig. 3.3, P^* and Q^* refer to the active and reactive power reference for the GFL, respectively. To ensure accurate power exchange between the converter and grid, the GFL must be synchronised with the connected power network [50], [130], [131]. In this section, the general control strategies of GFL converters are introduced.

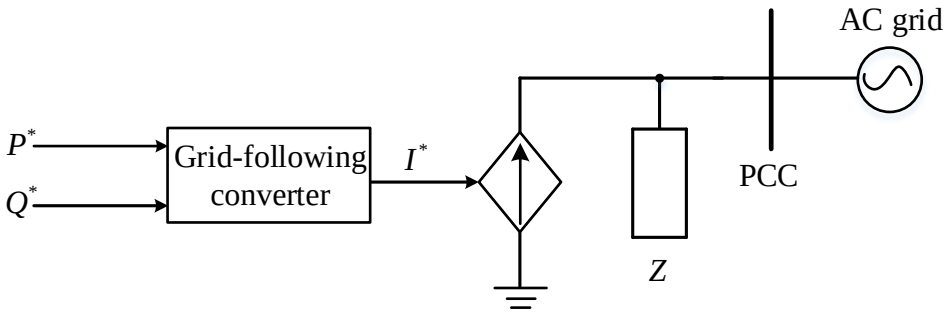

Fig. 3.3 Simplified representation of a GFL

3.2.1 Vector current control

According to (3.2), the converter output current I_{ldq} can be regulated by the converter output voltage V_{convdq} through PI regulators, which describes the principle of the vector current controller shown in Fig. 3.4 and can be expressed as:

$$\begin{cases} V_{convd} = V_{cd} - \omega L_f I_{lq} + \left[k_{pi}\left(I_{ld}^* - I_{ld}\right) + k_{ii}\int\left(I_{ld}^* - I_{ld}\right)dt \right] \\ V_{convq} = V_{cq} + \omega L_f I_{ld} + \left[k_{pi}\left(I_{lq}^* - I_{lq}\right) + k_{ii}\int\left(I_{lq}^* - I_{lq}\right)dt \right] \end{cases} \tag{3.3}$$

where I_{ld}^* and I_{lq}^* are the current orders which can be given by outer P and Q controllers. k_{pi} and k_{ii} are the proportional and integral gain of the PI regulator, which may be designed using:

$$\begin{cases} k_{pi} = 2\xi_i \omega_i L_f \\ k_{ii} = \omega_i^2 L_f \end{cases} \tag{3.4}$$

where ξ_i and ω_i are the damping ratio and natural frequency of the vector current controller, respectively. The natural frequency ω_i for the vector current controller is usually set from 20π to 40π rad/s, while the damping ratio ξ_i is normally set from 0.5 to 1.

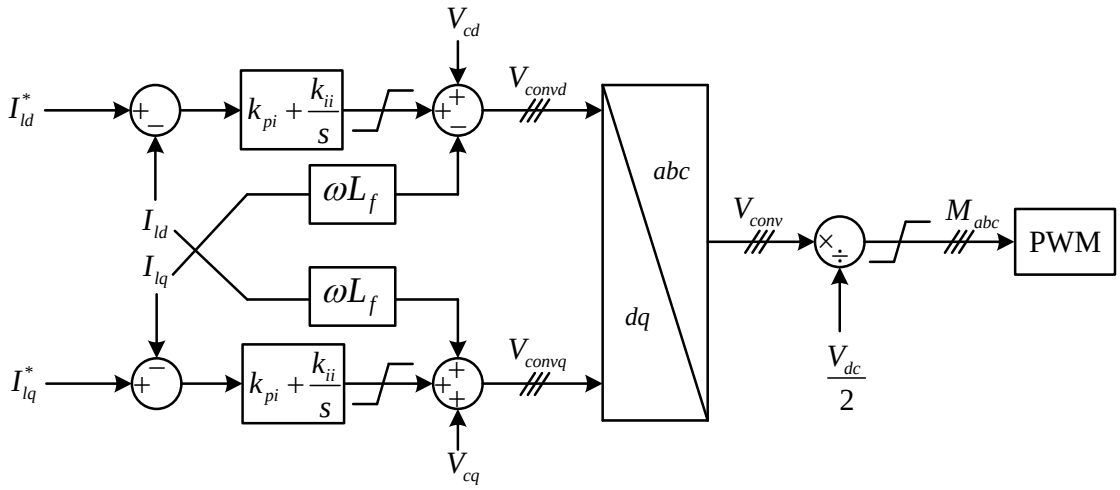

Fig. 3.4 Control block diagram of vector current control

Referring to Fig. 3.4, the converter output voltage V_{conv} needs to be transformed from the dq reference frame into three-phase reference frame using inverse Park Transformation stated in [12]. The modulation signal M_{abc} is then derived as [129], [132]:

$$M_{abc} = V_{conv} \div \frac{V_{dc}}{2} \tag{3.5}$$

As shown in Fig. 3.4, The active current I_{ld} and reactive current I_{lq} are controlled to track their respective references by the PI regulators in the vector current controller. The vector current control is broadly adopted for the power converters for connecting renewable energy generation and energy storage system due to the sufficient capability of overcurrent protection, precise control of instantaneous current waveforms and extremely good dynamics [50], [133], [134]. It is commonly used as the inner controller.

With additional outer controllers, the active and reactive power flowing into the AC grid can be regulated, which will be introduced later in this section.

3.2.2 Phase-locked loop (PLL)

On grid connected operation, the estimation of the AC grid voltage properties, such as voltage magnitude, frequency and phase angle, has to be precise to conduct an accurate control of the active and reactive power flowing into the AC grid [50]. To synchronise the power converters with the network in three-phase systems and to conduct the dq transformation, the phase of the AC grid voltage is required, which is usually acquired by using the phase-locked loop (PLL) [24], [50], [135], [136]. The block diagram of a normal PLL is depicted in Fig. 3.5. The value of V_{cq} reflects the angular position error of the d-axis of the reference frame and the actual network voltage which will be explained explicitly in Chapter 6, so the PI regulator shown in Fig. 3.5 will produce the frequency deviation $\Delta\omega$ compared to the rated (pre-set) frequency ω_0. Then the estimated grid frequency ω is obtained which generates the estimated phase angle θ (equivalent to ωt) [50], [135].

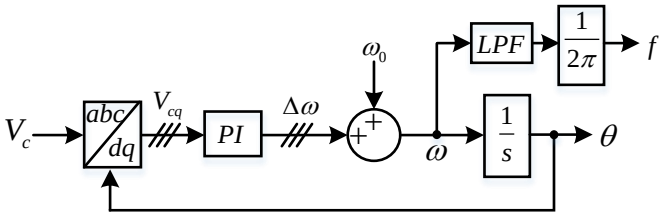

Fig. 3.5 Block diagram of PLL

3.2.3 Outer control

As aforementioned, the current orders for the vector current controller are usually provided by outer controllers. For different applications, various approaches can be used. In this subsection, the commonly used outer controllers are introduced.

A. Power control

If active and reactive power are to be controlled, the dq-axes current orders can be generated by the power controller. The active and reactive power generated from the VSC calculated by the voltage and current in the dq reference frame can be given by:

$$P = \frac{3}{2}\left(V_{cd}I_{ld} + V_{cq}I_{lq}\right) \tag{3.6}$$

$$Q = \frac{3}{2}\left(V_{cq}I_{ld} - V_{cd}I_{lq}\right) \tag{3.7}$$

where P and Q are the measured active and reactive power, respectively. As the d-axis converter filter bus voltage V_{cd} is aligned with the actual grid voltage vector at the PCC by PLL, the q-axis voltage V_{cq} is equivalent to 0. Thus, (3.6) and (3.7) can be simplified as:

$$P = \frac{3}{2}V_{cd}I_{ld} \tag{3.8}$$

$$Q = -\frac{3}{2}V_{cd}I_{lq} \tag{3.9}$$

Thus, the simplest method to provide the current orders for the vector current controller is to directly calculate the current orders based on the given power orders, as:

$$I_{ld}^{*} = \frac{2P^{*}}{3V_{cd}} \tag{3.10}$$

$$I_{lq}^{*} = \frac{2Q^{*}}{3V_{cd}} \tag{3.11}$$

where I_{ld}^{*} and I_{lq}^{*} are the active and reactive current order for the vector current controller, respectively. P^{*} and Q^{*} are the active and reactive power references, respectively.

Alternatively, close loop active and reactive power control using PI regulators can also be implemented as [137]:

$$I_{ld}^{*} = k_{pp}\left(P^{*} - P\right) + k_{ip}\int\left(P^{*} - P\right)dt \tag{3.12}$$

$$I_{lq}^{*} = k_{pq}\left(Q^{*} - Q\right) + k_{iq}\int\left(Q^{*} - Q\right)dt \tag{3.13}$$

where k_{pp} and k_{ip} are the proportional and integral gains of the PI regulator for active power, whereas k_{pq} and k_{iq} are the proportional and integral gains of the PI regulator for reactive power.

B. AC voltage control

Quite often, AC voltage regulation using the connected VSC is required, especially when the converter is connected to a weak grid, in which the converter needs to regulate the AC voltage with reactive power compensation to enable active power flow [24], [138], [139].

AC voltage control can be achieved by directly controlling the reactive current I_{lq}, to maintain the voltage magnitude at a certain level. There are generally two designs to control the AC voltage as depicted in Fig. 3.6. As shown, one uses a PI regulator, and the other one uses a droop controller (essentially a proportional controller with a proportional gain k_{pvi}).

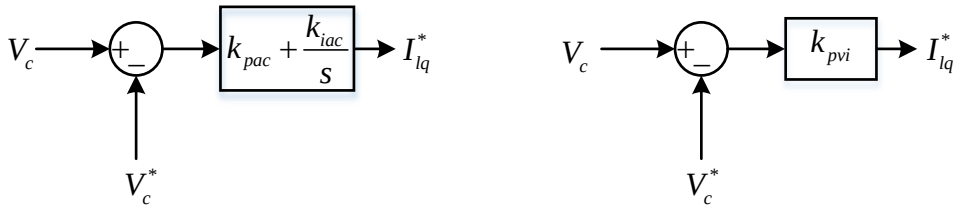

(a) (b)

Fig. 3.6 Control diagram of the AC voltage controller (a) PI controller (b) Droop controller

The AC voltage controller using a PI regulator shown in Fig. 3.6 (a) can be expressed as [24], [140]:

$$I_{lq}^{*} = k_{pac}\left(V_c - V_c^{*}\right) + k_{iac}\int\left(V_c - V_c^{*}\right)dt \tag{3.14}$$

where k_{pac} and k_{iac} are the proportional and integral gain of the PI controller, respectively. V_c^{*} and V_c are the reference and measured voltage magnitude at the converter filter bus, respectively. By this way, the AC voltage can be regulated to the set point with zero steady-state error providing the converter reactive power capability. On the other hand, when using droop controller, the generated reactive current (power) is dependent on the AC voltage error (the error between the set point and active AC voltage) through the droop constant k_{pvi}.

Vector current control based GFL converter has the capability to regulate the active and reactive power exchanged between the power converter and AC network. However, it is heavily dependent on the synchronisation with the AC grid by PLL. In the event of a very weak grid or when the system operates in islanded mode (i.e., no external voltage source), GFL converter using PLL may experience significant issues, e.g., lose synchronisation, system instability, etc [24], [25], [141], [142].

3.3 Control of GFM converters

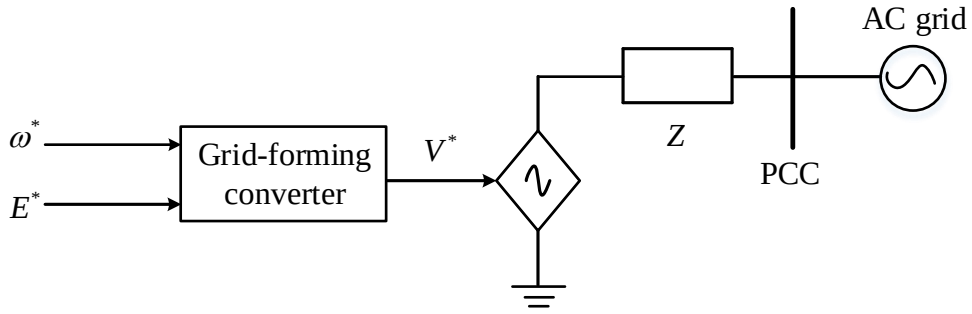

Fig. 3.7 Simplified representation of a GFM

As previously described, the operation of GFL converters relies on the presence of stiff external AC voltage which is usually provided by synchronous generators [33], [47]. However, system with large renewable generation and reduced power generation based on synchronous generators leads to power networks with significantly reduced stiffness. The purpose of GFM converters can be considered as to support the operation of an AC

power system during normal, islanded and weak grid conditions without relying on the services from SGs [33]. A conventional GFM converter can be represented as an ideal AC voltage source with a low-output impedance in series to the AC grid [50]. The simplified representation of a GFM converter is depicted in Fig. 3.7, where ω^* and E^* represent the setting angular frequency and voltage of the grid. The GFM converter has the ability to work both on grid connection and islanding networks, which cannot be achieved by the GFL converters discussed previously. In this section, the principles of the commonly adopted GFM control strategy are described.

3.3.1 Power droop control

Power droop control is commonly used to regulate the active and reactive power exchanged between the power converter and the AC grid in order to keep the grid voltage magnitude and frequency under control [50]. As described in [50], [85], [143], [127], the key concept of the power droop control is to mimic the general operation of an SG. An SG increases its frequency when the generated active power is reduced, and vice versa. The characteristics for the reactive power and the voltage magnitude are similar to those for the active power and frequency. By following this characteristics, the power converters can take the voltage magnitude and frequency as the inputs for the control system to adjust the generated active and reactive power to maintain the stability at all times [144], [145]. The schematic diagram of a GFM VSC connected to an AC grid is depicted in Fig. 3.8. In the representation, the GFM VSC is connected to the AC grid through an LC filter, a transformer and a local load Z_L.

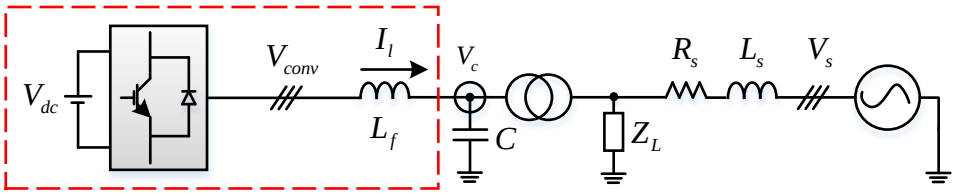

Fig. 3.8 Schematics of the GFM VSC connected to an AC grid

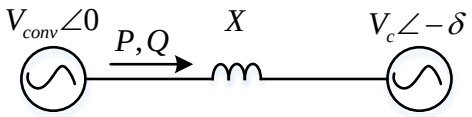

Fig. 3.9 Schematics of power flow through an inductive line

The power flow between the converter and the converter filter bus shown in the red box of Fig. 3.8 can be simplified into Fig. 3.9 by assuming the impedance is inductive. The active and reactive power through the inductive element L_f can be expressed as:

$$P = \frac{V_{conv} V_c \sin\delta}{X} \tag{3.15}$$

$$Q = \frac{V_{conv}\left(V_{conv} - V_c \cos\delta\right)}{X} \tag{3.16}$$

where X is the reactance of L_f between the two voltages, and δ refers to the power angle shift between the two voltages. By assuming the reactance X is very small (high SCR), then δ is also small, which gives $\sin\delta \approx \delta$ and $\cos\delta \approx 1$. Thus, (3.15) and (3.16) can be simplified into:

$$P = \frac{V_{conv} V_c \delta}{X} \tag{3.17}$$

$$Q = \frac{V_{conv}\left(V_{conv} - V_c\right)}{X} \tag{3.18}$$

According to (3.17) and (3.18), the power angle δ which is directly determined by the angular frequency ω predominantly influences the active power flow P, while the voltage difference $V_{conv} - V_c$ predominantly influences the reactive power flow Q [143], [146]. Thus, the basic principle of the droop control algorithm can be expressed as:

$$\begin{aligned} \omega^* &= \omega_0 + k_p\left(P^* - P\right) \\ V_c^* &= V_c^0 - k_q\left(Q^* - Q\right) \end{aligned} \tag{3.19}$$

where k_p and k_q are the respective droop coefficients. V_c^* and V_c^0 are the reference and nominal voltage at the converter filter bus, respectively. ω^* and ω_0 represent the reference and nominal frequency of the power converter, respectively. P^* and Q^* represent the reference active and reactive power of the power droop controller, while P and Q refer to the measured/actual active and reactive power of the power converter. The control block diagram is illustrated in Fig. 3.10.

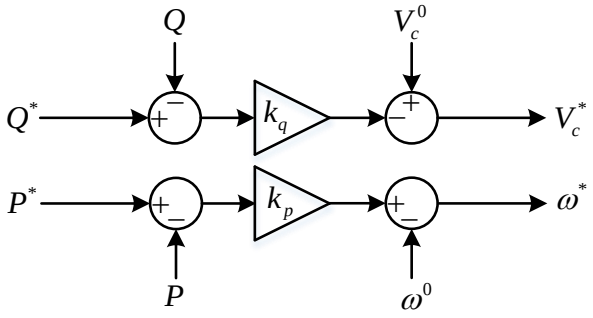

Fig. 3.10 Control diagram of the power droop controller

3.3.2 Voltage control

The principle of voltage control can be implemented to mimic the operation of the automatic voltage regulator for an SG [60]. The mathematical expression of the voltage controller can be given when a PI regulator is used, as:

$$\begin{cases} |V_{conv}| = k_{pg}\left(V_c^* - |V_c|\right) + k_{ig}\int\left(V_c^* - |V_c|\right)dt \\ \theta_{conv} = \int \omega^* dt \end{cases} \tag{3.20}$$

where $|V_{conv}|$ and $|V_c|$ are the magnitudes of the converter output and filter bus voltage, respectively. θ_{conv} represents the phase angle of the power converter, which is obtained by integrating ω^* that is given by (3.19). k_{pg} and k_{ig} refer to the proportional and integral gain of the PI regulator of the voltage controller, respectively.

The reference voltage at the converter filter bus V_c^* and reference angular frequency ω^* are produced by the power droop controller discussed previously. The control block

diagram of the voltage controller is illustrated in Fig. 3.11. The PI regulator is used to keep the voltage magnitude at the converter filter bus $|V_c|$ tracking the reference voltage magnitude V_c^* fed by the reactive power droop controller, as shown Fig. 3.11. The output of the PI regulator $|V_{conv}|$ has to be limited to avoid control saturation. The produced outputs of the voltage controller ($|V_{conv}|$ and θ_{conv}) will be fed into the PWM module to trigger the switch of the power converter.

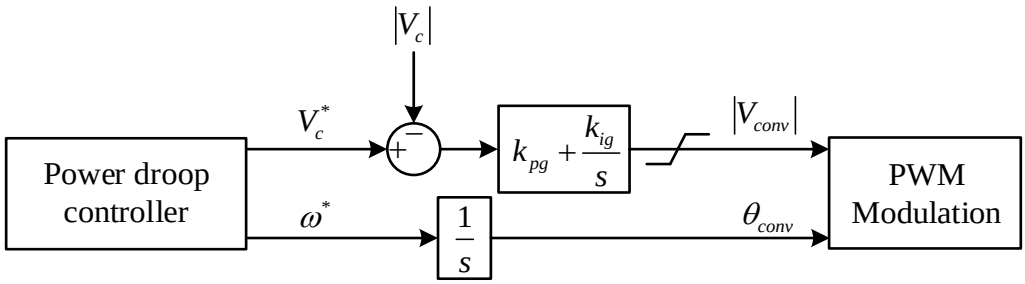

Fig. 3.11 Control diagram of the voltage controller

The GFM based on the control of voltage magnitude and phase angle has the ability to handle both grid-connected and islanded operation due to the good regulation of AC voltage and frequency. However, it lacks the capability of fault current limiting due to the absence of vector current control loop. This will be further investigated in later chapters.

3.4 Simulation Results

To validate the feasibility of the GFL and GFM converters with the discussed control strategies, time-domain models of Fig. 3.1 and Fig. 3.8 are developed in MATLAB/Simulink environment. The DC sides of both converters are connected to constant DC voltage sources with the DC voltage of V_{dc}, and two-level switching converter models are used.

3.4.1 Simulation of GFL converters

To verify the behaviours of the GFL converters with different outer controllers, two cases are tested, including power step performances on a relatively strong AC grid and

power ramp performances on a weak AC grid. The system and control parameters are depicted in Table 3.1.

Table 3.1 System and control parameters of the GFL converter

System initial parameters			
Power rating			100 MW
Nominal frequency ω_0 (f^0)			100π rad/s (50 Hz)
AC grid nominal voltage			110 kV
LC filter	Capacitance C		0.15 pu
	Reactance L_f		0.2 pu
Transformer	Y/Y		55 /110 kV
	Inductance		0.05 pu
GFL VSC control parameters (pu)			
PLL	Proportional gain k_{ppll}		0.4
	Integral gain k_{ipll}		12.57
Vector current control	Proportional gain k_{pi}		0.24
	Integral gain k_{ii}		22.62
Outer AC voltage controller	Droop control	Droop coefficient k_{pvi}	1.21
	PI control	Proportional gain k_{pac}	1
		Integral gain k_{iac}	48.4

A. Power step performances on a relatively strong AC grid

To test the behaviours of transient performances for the vector current control based GFL converters, the GFL converters using power controller, and AC voltage regulation using droop and PI controllers, are simulated on the system shown in Fig. 3.1. The GFL converter is connected to relatively strong AC networks with an SCR of 5 (based on 100 MW). For power control, the active power order P^* is increased from 0 pu to 1 pu at 2 s, while the reactive power order Q^* is remained at 0 pu. With AC voltage control, the

voltage reference V_c^* is fixed at 1 pu. Fig. 3.12 illustrates the waveforms of power step performances of the GFL converters with three different outer controllers. As can be seen in Fig. 3.12, all the three different outer loop controllers can settle down the system to steady-states quickly due to the use of fast vector current control loop. As the network is strong (SCR=5), the AC voltage change during the transient is relatively small, so the three outer control loop settings results in largely similar performances.

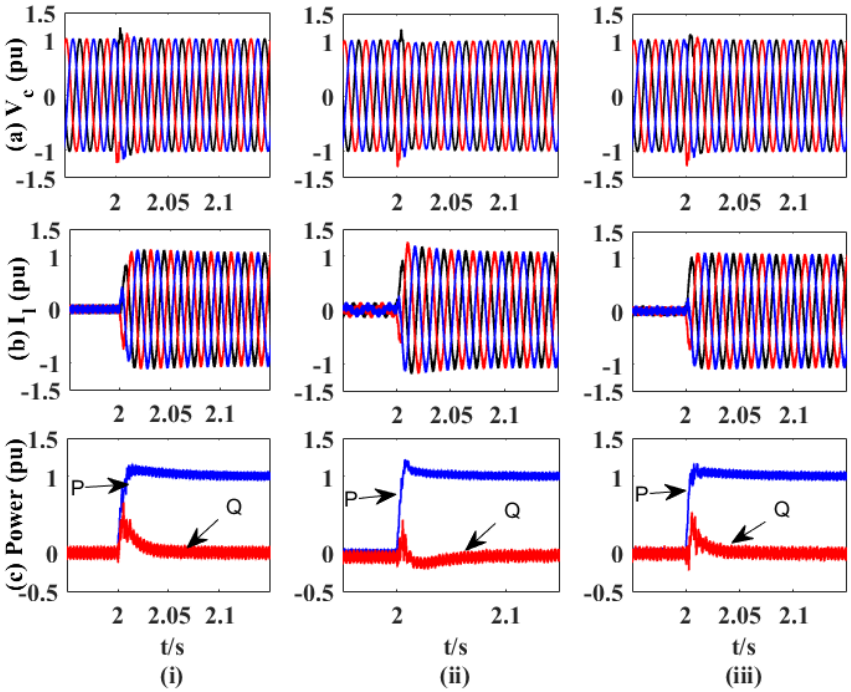

Fig. 3.12 Waveforms of power step performances of the GFL converters with different outer controllers: (i) Power control (ii) PI control for AC voltage regulation (iii) Droop control for AC voltage regulation

Fig. 3.13 displays the dq-axes currents and filter bus voltage magnitude of the GFL converters with the discussed control schemes, where the blue lines denote the reference signals, and red lines represent the measured/actual signals. As shown in Fig. 3.13, at the transient of power step, the change of active power causes the change of converter filter bus voltage and active current, which leads to the fluctuation of reactive current, hence the change of reactive power. After the power step transient, the converter filter bus voltage settles down, and the active power order P^* reaches 1 pu, which makes active and reactive current order be 1 pu and 0 pu, respectively. Then the PI regulators of vector

current controller operates to keep the actual active and reactive currents tracking their respective current orders. It should be noted that the reactive current order for the converter with power control is maintained at 0 as the reactive power reference is fixed at 0, as shown in Fig. 3.13 (i) (a).

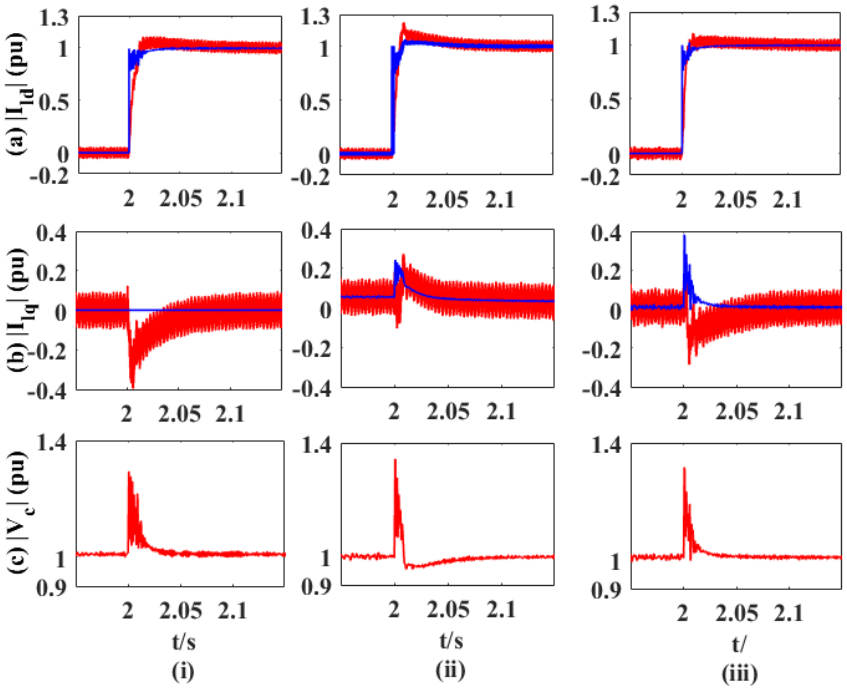

Fig. 3.13 Waveforms of dq-axes currents and filter bus voltage magnitude of the GFL converters with different outer controllers (i) Power control (ii) PI control for AC voltage regulation (iii) Droop control for AC voltage regulation

With the consideration of the simulation results shown in Fig. 3.12 and Fig. 3.13, it can be concluded that all the three categories of GFL converters behave adequately during a power step on a relatively strong grid.

B. Power ramp performances on weak AC grids

To verify the behaviours of the GFL converters using different outer controllers on weak networks, the GFL converter is connected to weak AC grids with SCR of 1.6 and 1.2 (based on 100 MW), respectively. The active power order P^* is ramped up from 0 pu to 1 pu within 0.3 s at 0.2 s, and the simulation results are shown in Fig. 3.14, Fig. 3.15 and Fig. 3.16.

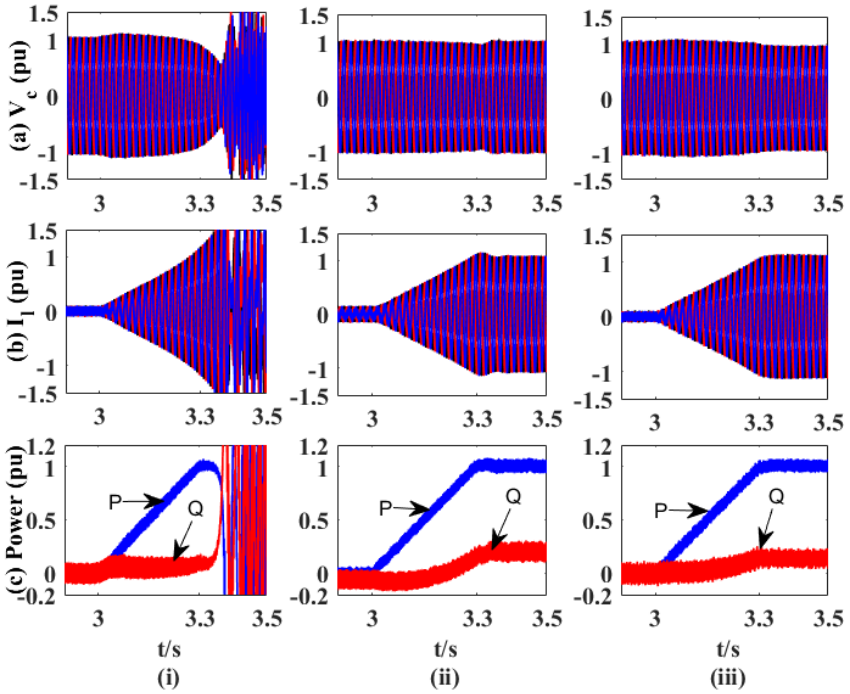

Fig. 3.14 Waveforms of the GFL converters on a weak grid with an SCR of 1.6 (i) Power control (ii) PI control (iii) Droop control

As can be seen in Fig. 3.14, the GFL converter with power control only loses control and becomes unstable before the generated active power level reaches 1 pu when connected to a weak grid with an SCR of 1.6, while the other two cases can settle down stably after the power ramp. This is because there must be sufficient voltage at the converter filter bus to support the active power flow [24], [138]-[139], which requires effective outer controller to control the voltage at the PCC. Fig. 3.14 (i) shows that with power control, the AC voltage is reduced when active power increases, and consequently, the system becomes unstable. Fig. 3.14 (ii) and (iii) show that with effective AC voltage control, the AC voltage is supported by reactive power compensation. This is depicted more clearly in Fig. 3.15, where the blue signals denote the reference signals, while the red lines represent the actual signals. As seen, the voltage magnitude at the converter filter bus is well controlled at the set level (1 pu) for the converter using PI control for AC voltage regulation, while the converter using AC voltage droop control drops the voltage magnitude from 1 pu to 0.95 pu during the operation. The voltage dip is determined by the set of droop coefficient k_{pvi} and the voltage reference V_c^*.

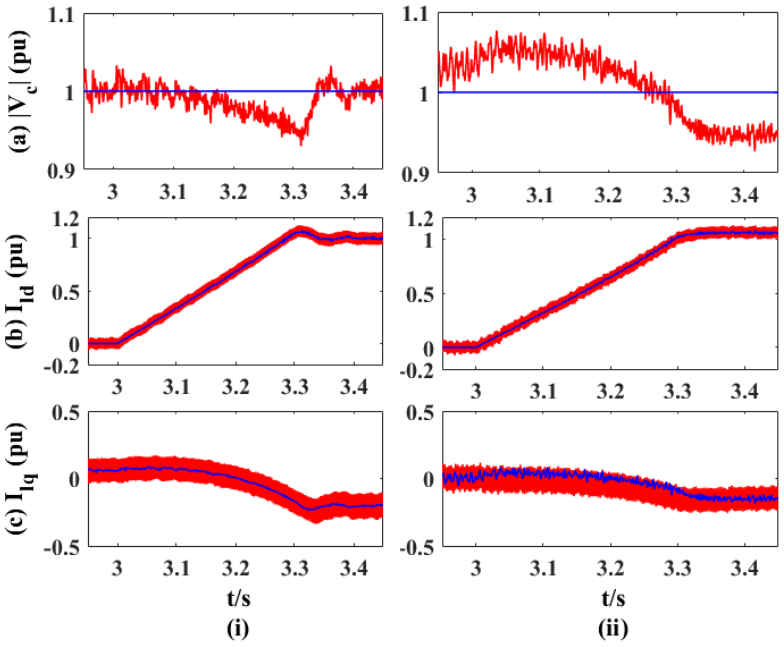

Fig. 3.15 Waveforms of dq-axes currents and filter bus voltage magnitude of the GFL converters with different outer controllers: (i) PI control for AC voltage regulation (iii) Droop control for AC voltage regulation

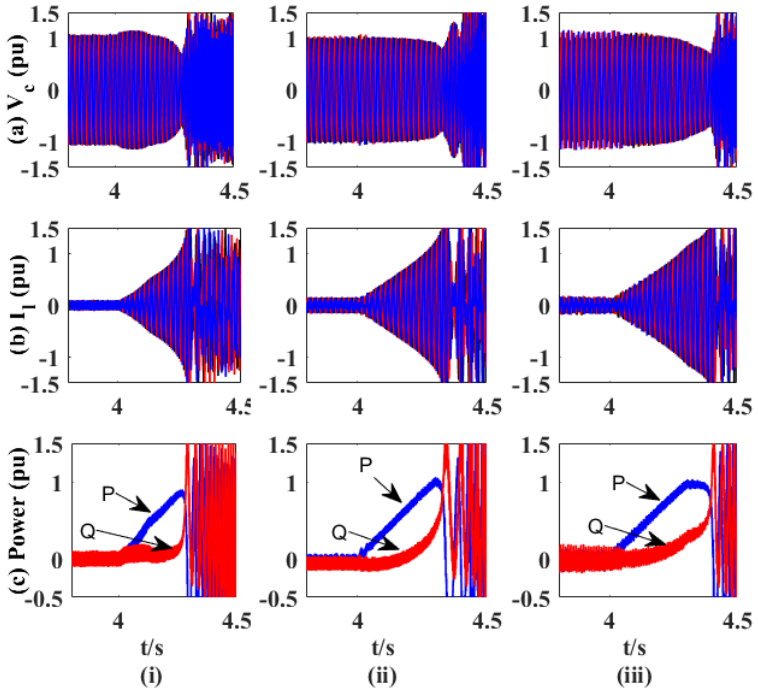

Fig. 3.16 Waveforms of the GFL converters on a weak grid with an SCR of 1.2 (i) Power control (ii) PI control (iii) Droop control

As displayed from the simulation results in Fig. 3.16, all three GFL converters lose control and become unstable while trying to generate bulk active power with the SCR of the connected grid at 1.2, which validates the constraint of power flow during a very weak grid.

3.4.2 Simulation of GFM converters

To validate the feasibility of the introduced GFM control strategies, the GFM converter based on the model in Fig. 3.8 is simulated. As way of example, three cases are illustrated including power step during grid connected operation, transition from grid connected operation to islanded operation, and load steps on an islanding network. The system and control parameters are listed in Table 3.2.

Table 3.2 System and control parameters of the GFM converter

System parameters		
Power rating		100 MW
SCR		5
Nominal local load demand P_L		50 MW (0.5 pu)
Nominal frequency ω_0 (f^0)		100π rad/s (50 Hz)
AC grid nominal voltage		55 kV
LC filter	Converter reactance L_f	0.2 pu
	Capacitance C	0.15 pu
Transformer	Y/Y	55 /110 kV
	Inductance	0.05 pu
GFM VSC control parameters (pu)		
Power droop control	Active power droop coefficient k_p	0.01
	Reactive power droop coefficient k_q	0.05
Voltage control	Proportional gain k_{pg}	8
	Integral gain k_{ig}	80

A. Performance of power step on grid connected operation

To verify the behaviour of transient performance of the GFM control, the active power reference of the power droop control shown in Fig. 3.10 is changed from 0 pu to 1 pu at 2 s, while the reactive power reference is fixed at 0 pu.

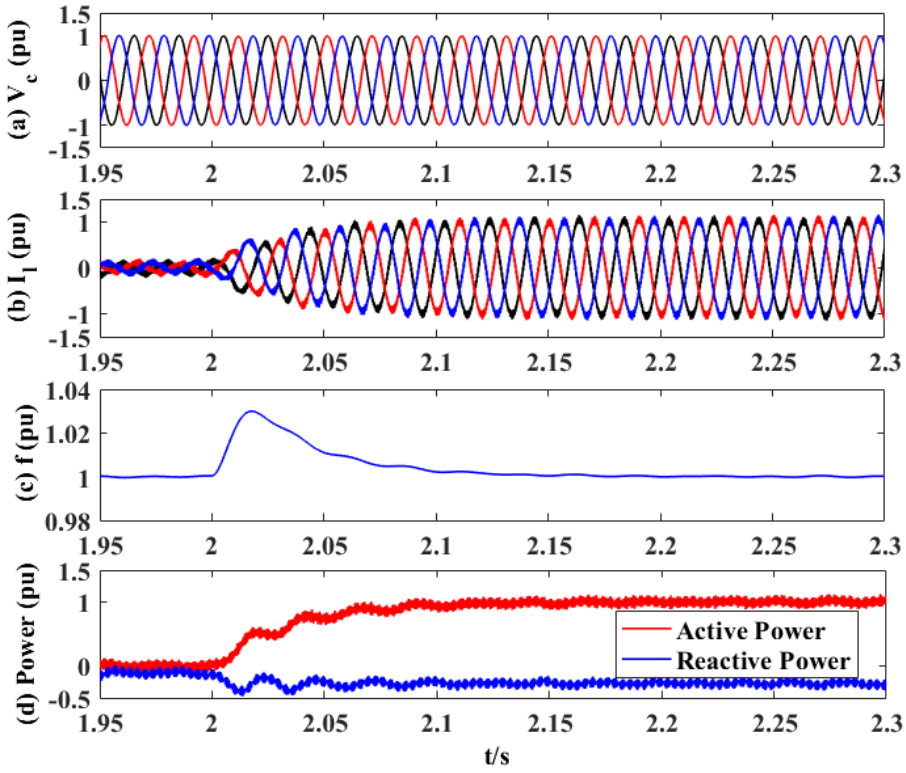

Fig. 3.17 Waveforms of power step performance on grid connected operation (a) Converter filter bus voltage (b) Converter output current (c) Frequency (d) Delivered power

Fig. 3.17 illustrates the waveforms of power step performance of the GFM converter on grid connected operation. As displayed in Fig. 3.17 (a), the AC voltage is well controlled before, at and after the power step transient. The generated active power is gradually increased from 0 pu to 1 pu with a time duration of 0.15 s as well as the converter output current I_l as displayed in Fig. 3.17 (b) and (d). As shown in Fig. 3.17 (d), both active and reactive power experience oscillations, which is the trade-off between the function of the GFM and the transient stability. The frequency experiences a small increase to about 1.03 pu at the power step transient in order to increase the active power

output, and then settles back to 1 pu at 2.15 s. The simulation results verifies that the conventional GFM converter can settle down to steady-state quickly with a power step on grid connected operation.

B. Performance of transition from grid connected operation to islanded operation

To test the operations of the GFM converter during both grid connected and islanded operation, the system shown in Fig. 3.18 is disconnected from the AC grid by opening the Switch S at 4 s. In this scenario, the converter transits from grid connected operation to islanded operation. The simulation results are depicted in Fig. 3.19. As shown, the converter with GFM control provides stable voltage control on both grid connection and islanding networks. On islanded operation, the converter only generates the active power to the local load (50 MW or 0.5 pu). Hence, the converter active power and output current drop down to 0.5 pu as displayed in Fig. 3.19 (b) and (d). As illustrated in Fig. 3.19 (c), the system frequency increased to 1.005 pu due to the active power droop controller, and the active power droop controller increases the system frequency in order to decrease the generated active power for the demand of the local load.

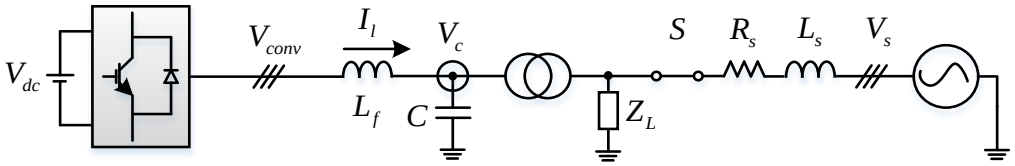

Fig. 3.18 Schematic diagram of the GFM VSC for the transition from grid-connected operation to islanded operation

The simulation results prove that the converter with GFM control has the ability to provide an autonomous and smooth transition from grid connected operation to islanded operation.

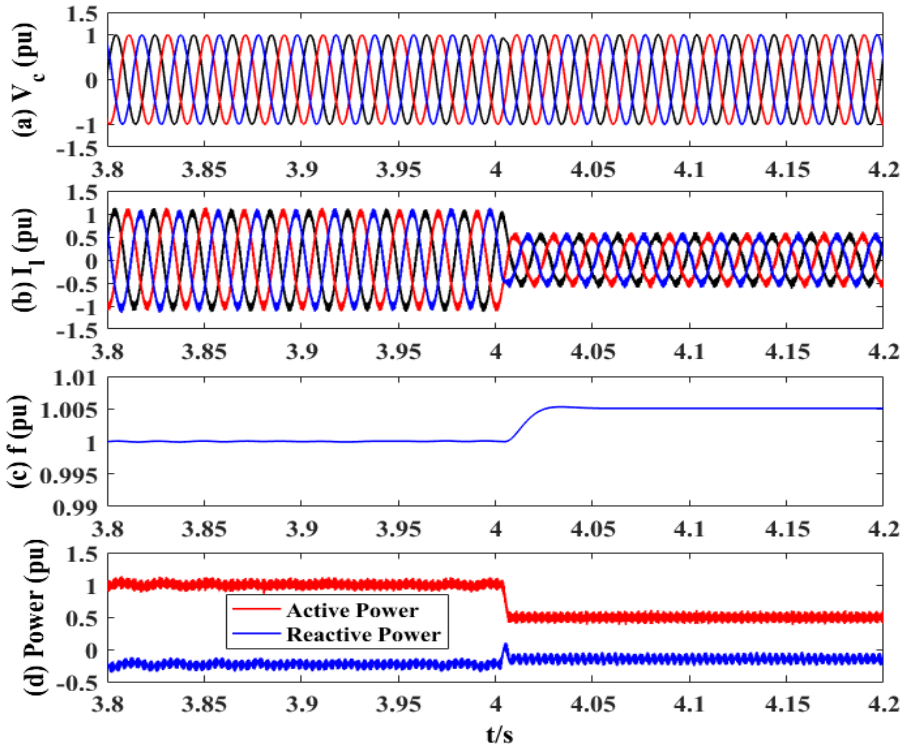

Fig. 3.19 Waveforms of performances of the GFM VSC on both grid connected and islanded operations: (a) Converter filter bus voltage (b) Converter output current (c) Frequency (d) Delivered power

Table 3.3 Sequences of load steps during islanded operation

Time	Events
4.1-4.2 s	Nominal local demand of 50 MW (0.5 pu)
4.2-4.3 s	An additional resistive load (25 MW, 0.25 pu) is connected.
4.3-4.5 s	The additional load (25 MW, 0.25 pu) is disconnected
4.5-4.6 s	An additional resistive load (125 MW, 1.25 pu) is connected, and the converter is overloaded.
4.6-4.7 s	The extra load (125 MW, 1.25 pu) is disconnected, the converter generates active power to feed the nominal load.

C. Performances of load steps on islanded operation

As tested previously, the generated power of the converter is determined by the demand of the local load when the converter is working on an islanding network. To verify this capability of the conventional GFM converter, load step tests are simulated. The sequences of load steps are depicted in Table 3.3.

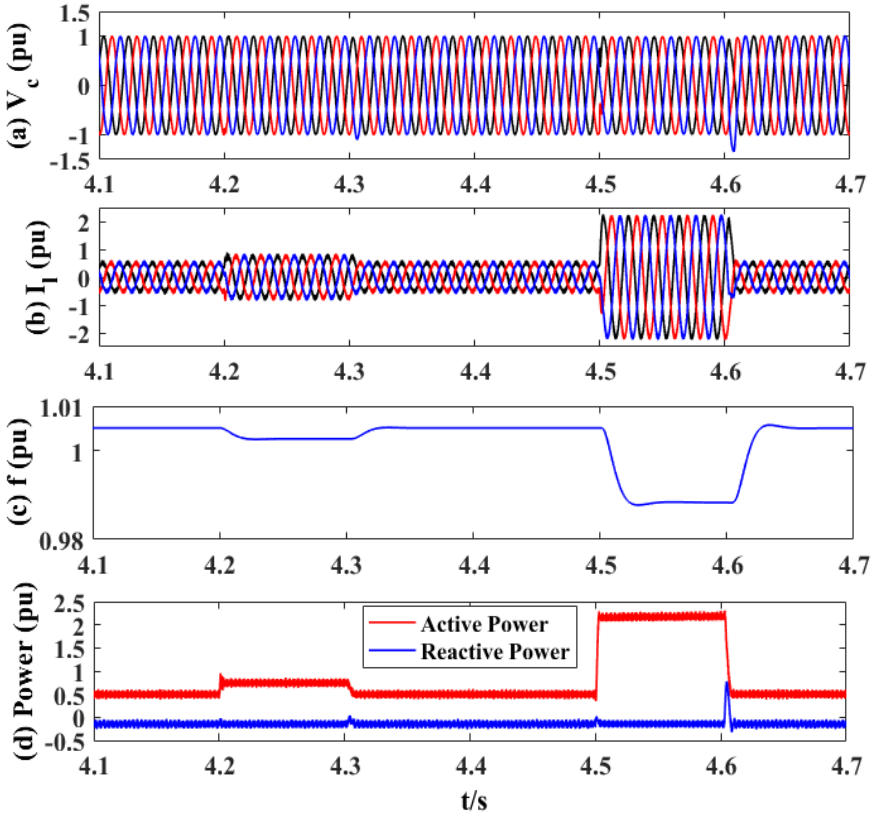

Fig. 3.20 Waveforms of load step performances of the GFM on islanded operation

Fig. 3.20 displays the waveforms of load step performances of the GFM converter on islanded operation. The voltage is well controlled without any obvious fluctuation during the load steps as shown in Fig. 3.20 (a). The frequency is decreased from 1.005 pu to 1.002 pu due to the additional load step at 4.2 s (25 MW, 0.25 pu), and recovers back to 1.005 pu after the disconnection of the additional load since 4.3 s, which is resulted from the operation of the active power droop controller, as displayed in Fig. 3.20 (c) and (d). When an extra load (150 MW) is connected from 4.5 s to 4.6 s, the total demand of the local side goes to 2.25 pu and the system is overloaded. As seen in Fig. 3.20 (b), the converter output current exceeds 2 pu which is not acceptable due to the low thermal

inertia of VSC. Hence, the converter with the introduced GFM control needs additional current limit control for the condition of overload and external AC faults, to avoid the damage of semiconductors [147]-[148].

The simulation results shown in Fig. 3.20 verify that the converter with the discussed GFM control can provide a stable operation on an islanded network but lacks the capability of overcurrent protection.

3.5 Summary

This chapter introduces the control strategies of GFL and GFM converters. The control schemes of the GFL converter include the vector current control, PLL and different outer controllers, while the control schemes of the GFM converter consist of power droop and voltage control to control the voltage magnitude and phase angle. The GFL converter uses PLL to synchronise with the AC grid to regulate the active and reactive power flow, so it could potentially experience problems during weak grid operation, especially with simple power control as the outer controller. To address the issues resulted from the use of GFL converters, GFM converters are developed to support the terminal voltage and frequency.

With respect to the reviewed GFM control methods in Chapter 2 and this chapter, most of them control the voltage magnitude and power angle to support the terminal voltage. Hence, the control accuracy is adversely affected by the coupling effect resulted from the time-varying mutual inductances. In addition, the most common problem faced by existing GFM converters is the limited capability of overcurrent limiting. Although several current limiting techniques introduced in Chapter 2 can be used to improve the overcurrent capability of the GFM converters, there are still limitations considering different fault and grid conditions. The first issue is the distribution of the active (d-axis) and reactive (q-axis) current during a fault. On grid connection network, the active and reactive current are required to follow appropriate points at times to support the GFM converter during and after the fault. However, the active and reactive current are completely dependent on the impedance of the local load during islanding network. This indicates that the current and voltage responses for grid connection and islanding network are completely different, which has not been addressed by existing GFM converters. In

Chapter 4, a universal GFM VSC control is developed to deal with this issue. Furthermore, the constraint of current controller on weak grids brings significant difficulties for the GFM converter to control both symmetrical and asymmetrical AC faults, and provide grid support functionality in the meantime. Hence, it requires to activate the entire current control loop only during faults, and retain the GFM control scheme in the meantime. Most of existing methods use control mode switching to avoid this issue without remaining the GFM functionality, while some of the methods retain the current controller that can cause instability issues during weak grid connection. In addition, the coordination between the positive- and negative-sequence current control loop is also complicated, which is solved by the proposed GFM VSC with enhanced AC fault current control in Chapter 5.

Chapter 4 Universal grid-forming VSC control for grid connected and islanded operation

As discussed in Chapter 3, the GFL VSC using vector current control loop is mostly used for connecting renewable generations due to its fast response and effective fault current limiting during large external transients [133], [134]. However, it lacks the capability of working on islanded operation due to the absence of effective AC voltage regulation, which is increasingly becoming important for VSCs used for renewable generations. The conventional GFM VSC introduced in Chapter 3 is able to solve this issue. Nevertheless, the capability of overcurrent limit due to the absence of current control loop needs further investigation. Thus, a universal control strategy for the power converters will be beneficial, which can combine the advantages of the conventional GFL and GFM VSC, to operate stably on both grid connection and islanding networks, even during large external transients.

With grid connection, the operation of the VSC requires the active (d-axis) and reactive (q-axis) current to follow varying reference points [149], whereas, the active and reactive current are determined by the local load during islanding. This brings a big challenge for the design of the VSC control scheme, which requires a universal current controller for the transient events on both grid connected and islanded operation.

In this chapter, a universal GFM VSC control strategy for grid connected and islanded operation is proposed. The strategy includes the adaptive power droop control, frequency droop control, GFM direct voltage control, PLL and current limit control. The proposed control strategy can provide effective overcurrent protection and sharing of the active and reactive currents during AC faults on both islanded and grid connected operation. Time-domain simulations in MATLAB/Simulink verify the feasibility of the proposed control strategy.

4.1 Control requirements

The universal converter control scheme enables the VSC to operate on controlled voltage source (GFL mode) synchronised with the grid to regulate the active and reactive power flowing into the connected AC network during a strong grid connection, while as a GFM VSC to establish its own AC voltage magnitude and frequency when the network becomes islanding. The overall control requirements of the VSC are as follows:

- Precise grid synchronisation. It is essential to provide precise grid synchronisation for the VSC to ensure accurate and stable operations when the converter is connected to an AC grid.
- Active and reactive power control. For universal operation on both grid connection and islanding networks, the VSC is required to control the generated power to the AC grid, and to maintain the power balance of the entire system [84], [144] , [150].
- AC voltage and frequency control. On an islanding network, the VSC needs to regulate the voltage magnitude and frequency for the network to maintain a stable islanded operation.
- Current limiting. The VSC should have the capability to limit overcurrent caused by the external faults and overloaded condition, for both grid connected and islanded operation. It is also desirable to control the active and reactive current sharing during such transient events.

Fig. 4.1 illustrates the overall control structure of the proposed universal GFM VSC. The general GFM control scheme is boxed by the red dotted line, while the universal current limit control scheme is boxed by the pink dotted line. The converter is connected to the AC grid through an LCL filter and a local load with an impedance of Z_L. Switch S is connected between the AC grid and converter to perform the VSC on grid connected and islanded operation. The impact of the DC side of the VSC is neglected, i.e., DC side is connected to a fixed DC source. The detailed functions and designs of the individual control block will be introduced in the following sections.

4.2 Direct voltage control

As aforementioned, the system model in the dq reference frame for the circuit displayed in Fig. 4.1 can be expressed as:

$$\begin{bmatrix} V_{convd} \\ V_{convq} \end{bmatrix} = \begin{bmatrix} V_{cd} \\ V_{cq} \end{bmatrix} + \begin{bmatrix} 0 & -\omega L_f \\ \omega L_f & 0 \end{bmatrix} \begin{bmatrix} I_{ld} \\ I_{lq} \end{bmatrix} + \begin{bmatrix} L_f & 0 \\ 0 & L_f \end{bmatrix} \frac{d}{dt} \begin{bmatrix} I_{ld} \\ I_{lq} \end{bmatrix} \tag{4.1}$$

where V_{cdq}, V_{convdq} and I_{ldq} are the filter bus voltage, converter output voltage and output current in the dq reference frame, respectively. ω is the estimated angular frequency of the network by PLL.

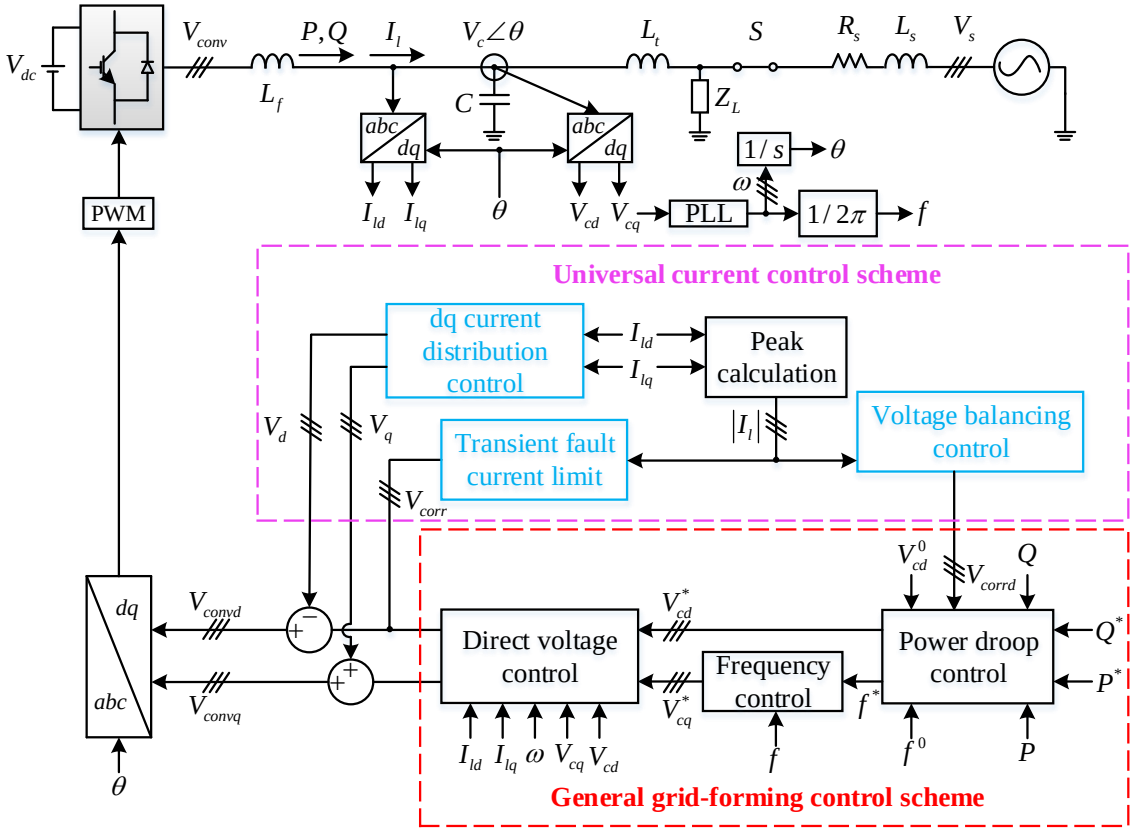

Fig. 4.1 Overall structure of the control system

To directly control V_{cdq} without inner current loops, the converter output voltage V_{convdq} can be regulated by considering the error between the actual V_{cdq} and their respective voltage orders. According to (4.1), $L_f dI_{ldq}/dt$ is negligible on steady-state

while the disturbances resulted from I_{ldq} and V_{cdq} can be compensated by using PI regulators. Hence, the VSC direct voltage control in the dq reference frame can be described as:

$$\begin{cases} V_{convd} = k_{pv}\left(V_{cd}^{*} - V_{cd}\right) + k_{iv}\int\left(V_{cd}^{*} - V_{cd}\right)dt - \omega I_{lq}L_f + V_{cd} \\ V_{convq} = k_{pv}\left(V_{cq}^{*} - V_{cq}\right) + k_{iv}\int\left(V_{cq}^{*} - V_{cq}\right)dt + \omega I_{ld}L_f + V_{cq} \end{cases} \tag{4.2}$$

where V_{cd}^{*} and V_{cq}^{*} are the voltage orders in the dq reference frame. k_{pv} and k_{iv} are the proportional and integral gains of the PI regulators used in the direct voltage controller, respectively. The control block diagram of the direct voltage control is depicted in Fig. 4.2.

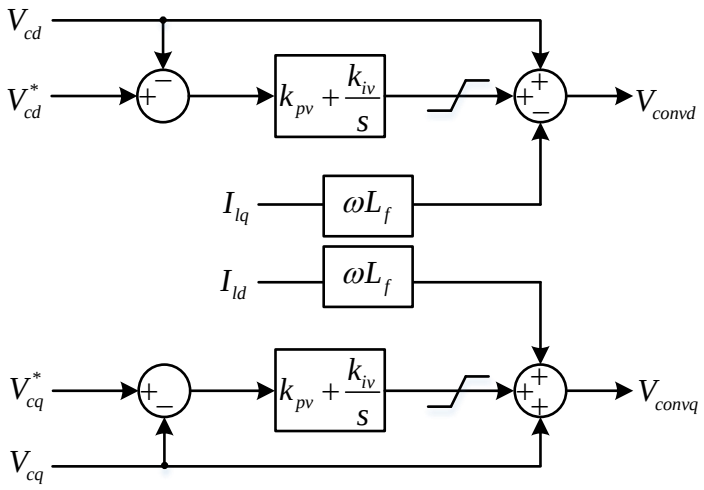

Fig. 4.2 Diagram of the direct voltage control

The direct voltage control used for the universal GFM VSC is completely different from the voltage control introduced in Chapter 3 and other methods stated in [61], [68], [69], [73], [141], [151], [152], where it is based on the control of two independent voltage components (d- and q-axis). The dq reference frame based direct voltage controller removes the coupling effect resulted from the time-varying mutual inductances [12]. By setting separated dq-axes voltage components, the d-axis control loop controls the voltage magnitude, while the q-axis control loop specifically controls the frequency which will be covered later in this chapter. Moreover, since both voltage and current variables are transformed to the dq reference frame, active and reactive current can also be controlled

individually to avoid coupling effect between them, so as to make it easier to realise fault current limiting and sharing of active and reactive current compared to the conventional GFM using instantaneous current limit control strategies as stated in [18], [42], [59], [60]. The detailed current limit controller will be introduced later in this chapter.

4.3 PLL

The conventional GFM converters introduced in Chapter 3 and those used in many other methods do not use PLL, whereas the synchronisation with the network is achieved by the power droop controller. However, this could bring significant challenges as the converter may completely lose synchronisation with the grid during a severe external AC fault, resulting in difficulties in controlling fault current. However, in the event of a severe AC fault close to the VSC AC terminal, the terminal voltage could be reduced to almost zero, during which PLL has no external voltage to lock to and potentially cause the frequency to diverse. Consequently, after fault clearance and network voltage recovery, the actual system frequency/angle can have a significant difference with the values produced by PLL, leading to a large transient current.

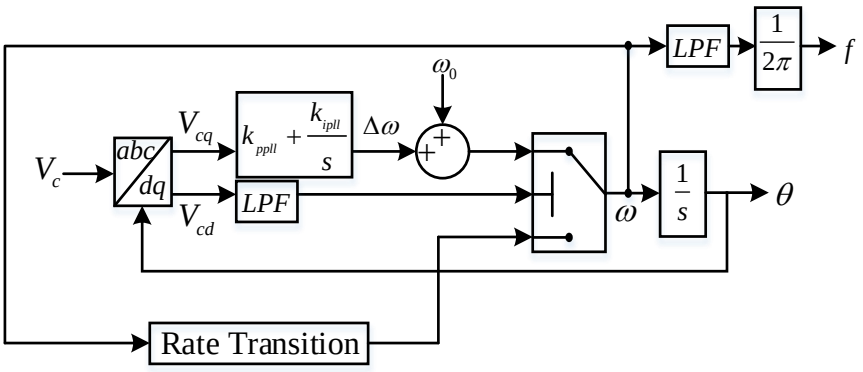

Fig. 4.3 Diagram of PLL

To address the issue, the principle adopted by PLL in this thesis is shown in Fig. 4.3. As shown, when the voltage magnitude V_{cd} drops below the pre-set level of 0.15 pu, PLL fixes the frequency to the value measured 0.2 s ago (through the rate transition) and the PI regulator stops calculation. Once the voltage magnitude V_{cd} recovers to a level above

0.15 pu, PLL goes back to its normal operation. By this way, the system is ensured to maintain a smooth transient during zero (close to zero) network voltage.

4.4 Frequency droop control

To achieve a stable islanded operation, it is essential for the VSC to establish the voltage and frequency for the islanding network, which forms the concept of "grid-forming". The voltage regulation is given by the direct voltage control loop discussed in the previous section. According to the control diagram shown in Fig. 4.3, the frequency f estimated by PLL can be expressed mathematically as [134], [147], [153]:

$$f = f^0 + k_{ppll} V_{cq} + k_{ipll} \int V_{cq} dt \tag{4.3}$$

where f^0 is the nominal grid frequency (given by $\omega_0 / 2\pi$). k_{ppll} and k_{ipll} represent the proportional and integral gains of the PI regulator in the modified PLL shown in Fig. 4.3, respectively. The natural frequency of the k_{ppll} and k_{ipll} is usually tuned between 20π rad/s and 30π rad/s, while the damping ratio is normally set from 0.5 to 1. V_{cq} in (4.3) is the measured/actual q-axis voltage at the converter filter bus. The relationship between the angular frequency ω and q-axis voltage V_{cq} can be illustrated in Fig. 4.4.

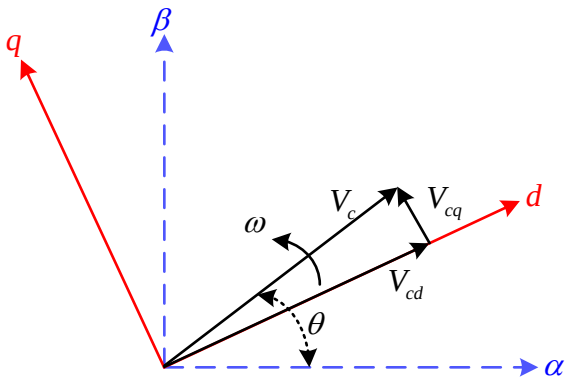

Fig. 4.4 Converter filter bus voltage vector in dq frame

As introduced in Chapter 3, the value of V_{cq} reflects the angular position error of the d-axis of the reference frame and the actual network voltage. For example, if V_{cq} is greater than 0, the angular speed ω of the d-axis by PLL will increase, and vice versa.

This indicates that controlling the q-component voltage V_{cq} at the converter filter bus can regulate the system angular speed ω, hence the system frequency f. Based on this inference, the q-axis voltage order can be depicted as:

$$V_{cq}^{*} = k_f \left(f^{*} - f \right) \tag{4.4}$$

where k_f and f^{*} represent the droop coefficient and the frequency order of the frequency controller, respectively. The principle of the frequency droop controller can be displayed in Fig. 4.5.

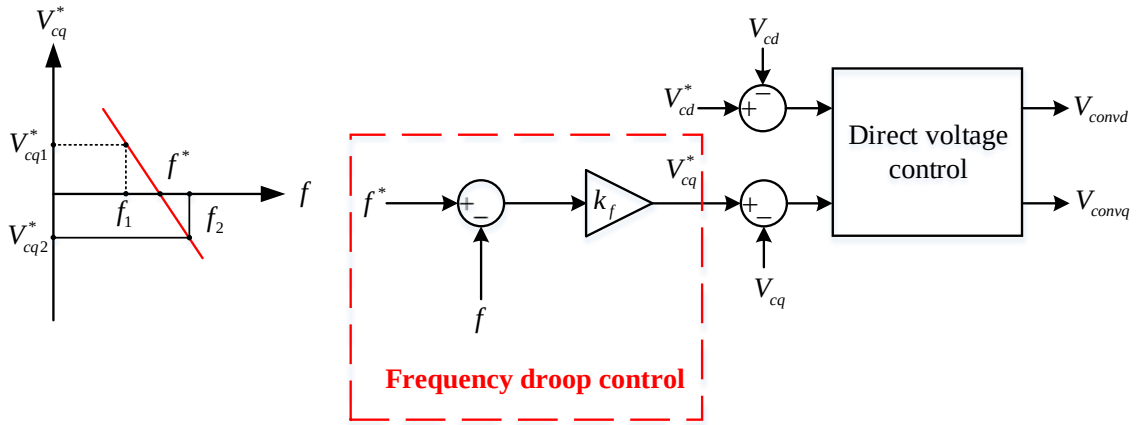

(a) (b)

Fig. 4.5 Principle of the frequency control (a) Characteristics (b) Control diagram

As shown in Fig. 4.5, when the frequency f (f_1 in Fig. 4.5 (a)) measured by PLL is smaller than the frequency order f^{*}, the frequency droop controller will produce a positive q-axis voltage order V_{cq1}^{*} which will be fed into the q-axis control loop of the direct voltage controller shown in Fig. 4.5 (b). Hence, a positive V_{cq} will appear at the filter bus AC voltage. Consequently, this positive V_{cq} is detected by the PLL and the output frequency from PLL is thus increased. As the output frequency of the PLL (and the angle) is used to synchronise the converter output voltage, the output frequency from the converter is thus increased to match the frequency reference f^{*}. Similar process can be considered when the actual frequency is higher than the frequency reference.

The frequency droop controller combined with the aforementioned direct voltage controller can regulate the system frequency to the reference f^*. Considering the need for the VSC to operate on grid connected and islanded operation, the frequency reference f^* needs to be set properly according to the operation requirements.

4.5 Adaptive power droop control

As discussed in Chapter 3, power droop control is normally used to regulate the active and reactive power flowing into the connected AC grid and to maintain the grid voltage and frequency under control. One problem arises during external AC voltage dip during which the converter might not be able to deliver the required active and reactive power. Consequently, the errors produced by $P^* - P$ and $Q^* - Q$ will cause saturations of the PI regulators in the direct voltage controller. To address this issue, the adaptive power droop control loop is designed as shown in Fig. 4.6.

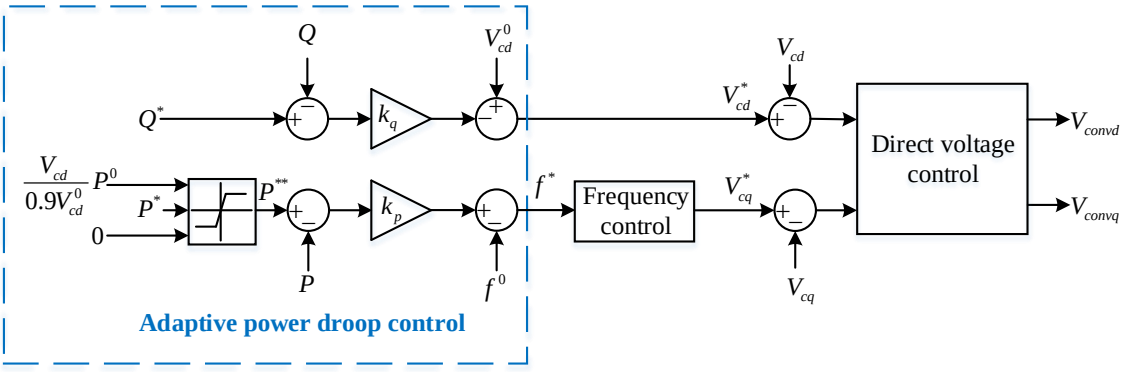

Fig. 4.6 Diagram of the adaptive power droop control

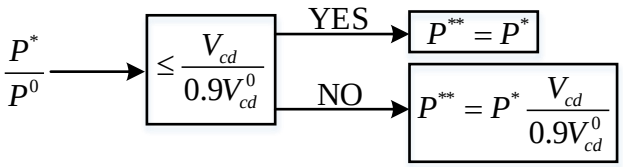

Fig. 4.7 Characteristics of active power reference

During large voltage dip, the ability of the VSC to export active power can be significantly reduced. Thus, the principle adopted in the adaptive power droop control is

to produce a dynamic active power reference P^{**} with respect to the ratio of V_{cd}/V_{cd}^0, to mitigate the control issues caused by the error of P^*-P during voltage dip. Fig. 4.7 shows the details of the active power reduction during voltage dip. The design considered here assumes that the VSC is able to deliver 1 pu active power when the AC voltage is reduced to 0.9 pu, and the active power delivery is then reduced proportionally according to the remaining AC voltage once it goes below 0.9 pu. As shown in Fig. 4.7, a dynamic saturation block is used to reduce the active power reference when $V_{cd}/\left(0.9V_{cd}^0\right) < P^*/P^0$, where V_{cd}^0 and P^0 are the rated AC voltage and active power. For reactive power, if the voltage dip is significant, a large reactive current (e.g., according to grid code requirement) will be required. Consequently, the active current/power will need to be limited further. Under such conditions, the above proposed method is not applicable, and the d-axis voltage mismatch issue will be addressed later in this chapter.

The expression of the adaptive power droop control is given by:

$$\begin{cases} V_{cd}^* = V_{cd}^0 - k_q\left(Q^*-Q\right) \\ f^* = \begin{cases} f^0 + k_p\left(P^*-P\right), & \text{when } \dfrac{V_{cd}}{0.9V_{cd}^0} \geq \dfrac{P^*}{P^0} \\ f^0 + k_p\left(P^*\dfrac{V_{cd}}{0.9V_{cd}^0} - P\right), & \text{when } \dfrac{V_{cd}}{0.9V_{cd}^0} < \dfrac{P^*}{P^0} \end{cases} \end{cases} \tag{4.5}$$

where the variables with superscript '0' denote the nominal values of the system. k_p and k_q represent the droop coefficients of the active and reactive power droop controller, respectively. P and Q are the measured active and reactive power which are given by (3.6) and (3.7) introduced in Chapter 3.

The active power droop controller operates to generate the frequency order f^* that is fed into the frequency droop controller, while the reactive power droop controller is used to produce the d-axis voltage order V_{cd}^* for the direct voltage controller.

Depending on the mode of operation, i.e., whether the VSC system is on grid connected or islanded operation, the above power and frequency control design lead to automatic frequency/ P and voltage/ Q regulations, i.e.,

- When the VSC is grid connected, the frequency reference f^* has to match the actual network frequency under steady-state, which may be different to the nominal value f^0. So the actual active power P delivered by the VSC will be slightly different to the active power reference P^*, which is determined by the actual network frequency and droop constant k_p. Similar for reactive power, the actual Q delivered by the VSC will be slightly different to the reactive power reference Q^*, which is determined by the actual network voltage and droop constant k_q.
- When the VSC is on islanded operation, the active and reactive power of the VSC are determined by the local loads, which may be different to P^* and Q^*. Consequently, the active and reactive power controllers will generate frequency and voltage errors, which means the actual network voltage and frequency will have small deviations from the nominal values of V_{cd}^0 and f^0 according to (4.5).

Thus, the combined design of the direct voltage control, the PLL and the active and reactive power droop control ensure the VSC system can be operated under either grid connected or islanded operation without the need to switch the control mode.

4.6 Universal Current control

The direct voltage controller with GFM ability ensures stable operations on grid connection and islanding networks. However, the absence of vector current control loop means that the converter lacks the capability of overcurrent protection. As overcurrent problems commonly occur in power electronic systems, such as during overload and external AC faults, it is essential to provide effective current limit control. In addition, the distribution of active and reactive current during external AC faults needs to be considered. When the system is grid connected, specific requirements in active and

reactive current provision in the grid code can be considered. However, during islanded operation, the distribution of active and reactive current is dependent on the local loads during faults. Hence, a universal dq current distribution control for both grid connected and islanded operation is also indispensable. In this section, the overcurrent protection and distribution of active and reactive current for both islanding and grid connection networks are proposed.

4.6.1 Transient fault current limit control

As discussed in the previous section, the PI regulator in the d-axis direct voltage control loop may saturate due to the mismatch between the voltage order V_{cd}^{*} and measured voltage V_{cd} during an external AC fault, which is the main cause for converter overcurrent. For the q-axis direct voltage control loop, the use of the adaptive active power droop controller can address the control saturation issue during external fault, and the system frequency can be largely controlled even during severe external faults. To solve the overcurrent issue caused by external voltage dip, a transient fault current limit controller using a current-voltage droop control is designed, which is illustrated in Fig. 4.8.

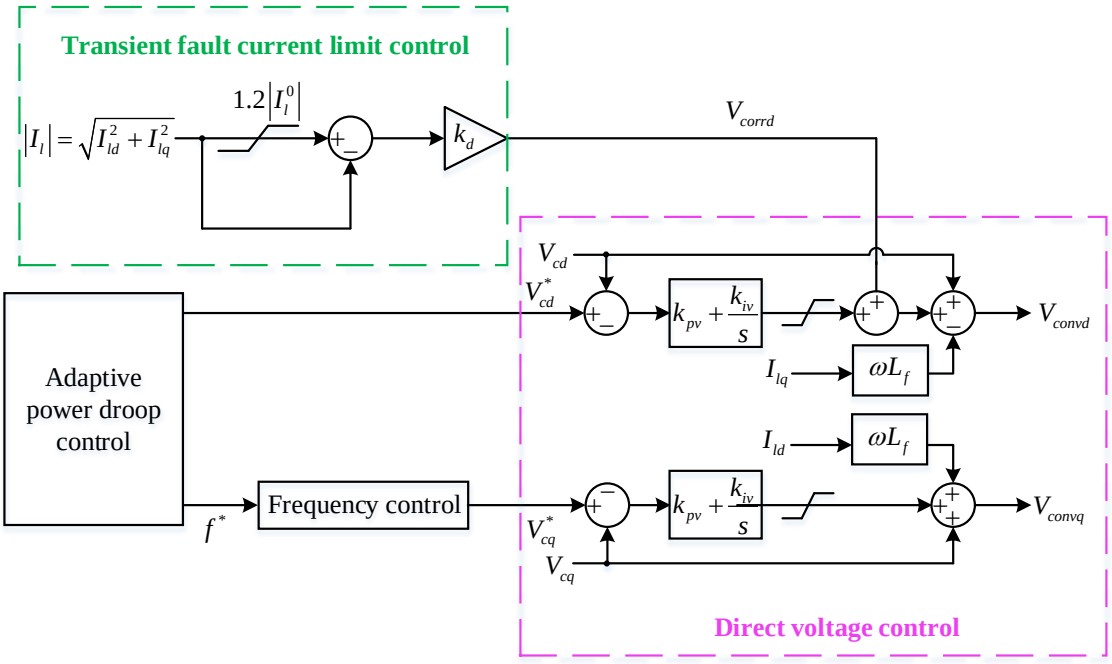

Fig. 4.8 Diagram of the transient fault current limit control

As shown in Fig. 4.8, an additional voltage control component is added to the d-axis voltage controller once overcurrent is detected. The concept is based on the consideration that, during a severe external voltage dip, the converter output voltage magnitude needs to be quickly reduced in order to limit the fault current. The mathematical model of the transient fault current limit controller can be expressed as:

$$V_{corrd} = \begin{cases} 0, & |I_l| \le 1.2|I_l^0| \\ k_d\left(1.2|I_l^0| - |I_l|\right), & |I_l| > 1.2|I_l^0| \end{cases} \tag{4.6}$$

where k_d is the proportional/droop gain, and 1.2 pu is considered as the overcurrent protection threshold, while the magnitude of the converter output current $|I_l|$ is given by:

$$|I_l| = \sqrt{I_{ld}^2 + I_{lq}^2} \tag{4.7}$$

On normal operation, the proposed controller produces no response as the actual converter current magnitude will be lower than 1.2 pu, so the current error is zero. During an external AC fault, when the actual current magnitude hits the upper limit $1.2|I_l^0|$ (I_l^0 is the nominal converter output current), a current error will be produced and a negative correction voltage V_{corrd} will appear through the droop gain k_d, which effectively reduce the output d-axis direct voltage. Once the reduced converter output voltage matches the low external voltage, the transient fault current can be limited. Once the converter output current drops below the limited level $1.2|I_l^0|$, the transient fault current limit control will then stop working.

The transient fault current limit control is designed for the control saturation at the inception of the fault to mitigate the transient fault current spike. When the fault current is settled down to a steady-state (below the pre-set level $1.2|I_l^0|$), it will stop working. This will be introduced in the following subsection.

4.6.2 Overcurrent limit control

As discussed previously, the transient fault current limit control is proposed to limit the transient overcurrent. It is desirable for the active and reactive current to follow respective orders during faults for grid connected operation, while the active and reactive currents are determined by the local loads on islanded operation, which requires to retain the AC direct voltage control loop. Thus, overcurrent issues cannot be addressed adequately with existing control schemes due to the saturation of direct voltage control loop with no specific active and current orders to follow. This can happen when the system is overloaded or during external AC faults on both islanded and grid connected operation. In order to ensure that the converter output current is limited (1.2 pu in this chapter) to protect the converter, an extra overcurrent limit control illustrated in Fig. 4.9 is designed.

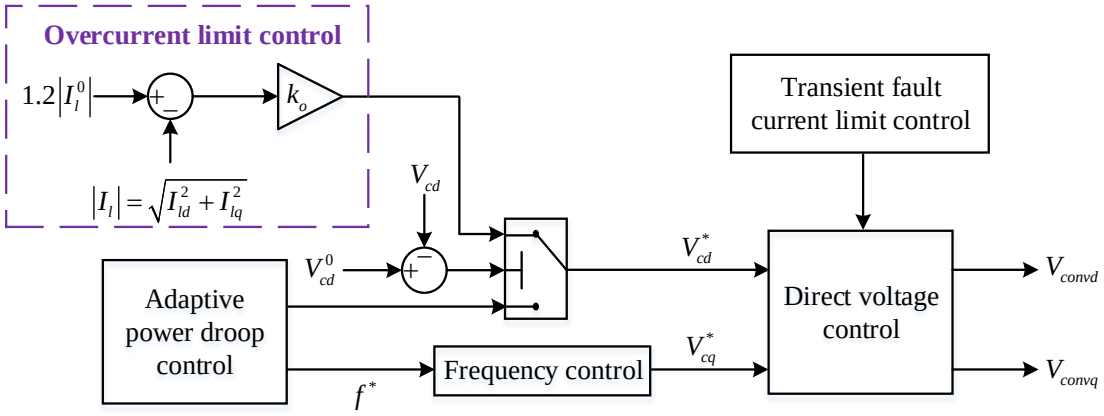

Fig. 4.9 Diagram of the overcurrent limit control

As shown in Fig. 4.9, the d-axis voltage order is produced by the overcurrent limit controller instead of the reactive power droop controller once a significant voltage dip is detected. The profile of the d-axis voltage order V_{cd}^* is given by:

$$V_{cd}^* = \begin{cases} V_{cd}^0 - k_q\left(Q^* - Q\right), & \Delta V_{cd} < 0.1V_{cd}^0 \\ k_o\left(1.2\left|I_l^0\right| - \sqrt{I_{ld}^2 + I_{lq}^2}\right), & \Delta V_{cd} \geq 0.1V_{cd}^0 \end{cases} \tag{4.8}$$

where k_o refers to the proportional gain for the control scheme. ΔV_{cd} represents the difference of voltage magnitudes between the measured and nominal filter bus voltage which can be expressed as:

$$\Delta V_{cd} = V_{cd}^{0} - V_{cd} \tag{4.9}$$

On normal operation, the difference of voltage magnitude ΔV_{cd} is less than the pre-set level $0.1V_{cd}^{0}$, then the d-axis voltage order V_{cd}^{*} fed into the direct voltage control is produced by the reactive power droop controller. When the system is overloaded on an islanded operation or suffered from an external AC fault on both islanded and grid connected operation, the difference of voltage magnitudes ΔV_{cd} will be greater than the pre-set level $0.1V_{cd}^{0}$. On this case, the d-component voltage order V_{cd}^{*} is given by the overcurrent limit controller as shown in Fig. 4.9 and (4.8). The general principle adopted on the overcurrent limit controller is to balance the measured the d-component voltage order V_{cd}^{*} with the measured the d-component voltage V_{cd} to retain the direct voltage control loop, so the distribution of active and reactive current is then determined by the local load on islanded operation. When the system is suffered from an external AC fault, the overcurrent controller can limit the overall fault current under the pre-set level 1.2 pu. This will cause the transient fault current limit control loop to stop working, which has been mentioned in the previous subsection.

4.6.3 dq current distribution control

It is essential to maintain the balance of power exchange among the converter, local load and AC grid on both islanding and grid connection networks, even during external AC fault conditions [129]. With the operations of the adaptive active power droop, overcurrent limit and transient fault current limit controllers, the overall current can be limited during an external AC fault. However, the sharing of active and reactive (dq) currents (as in grid code) needs to be addressed. As shown in (4.2) and Fig. 4.2, in the decoupling terms, I_{ld} and I_{lq} appear to the q- and d-axis of the direct voltage controller, respectively. Any change of I_{ld} and I_{lq} can result in the change of the q- and d-axis of the converter output voltage V_{conv}. This indicates that I_{ld} and I_{lq} can be controlled through the q- and d-axis of the direct voltage controller, through the so-called “cross-coupling control”. The detailed model and analysis of the so-called “cross-coupling

control" have been explored in [149], [154], [155]. Then the dq current distribution controller can be designed as illustrated in Fig. 4.10.

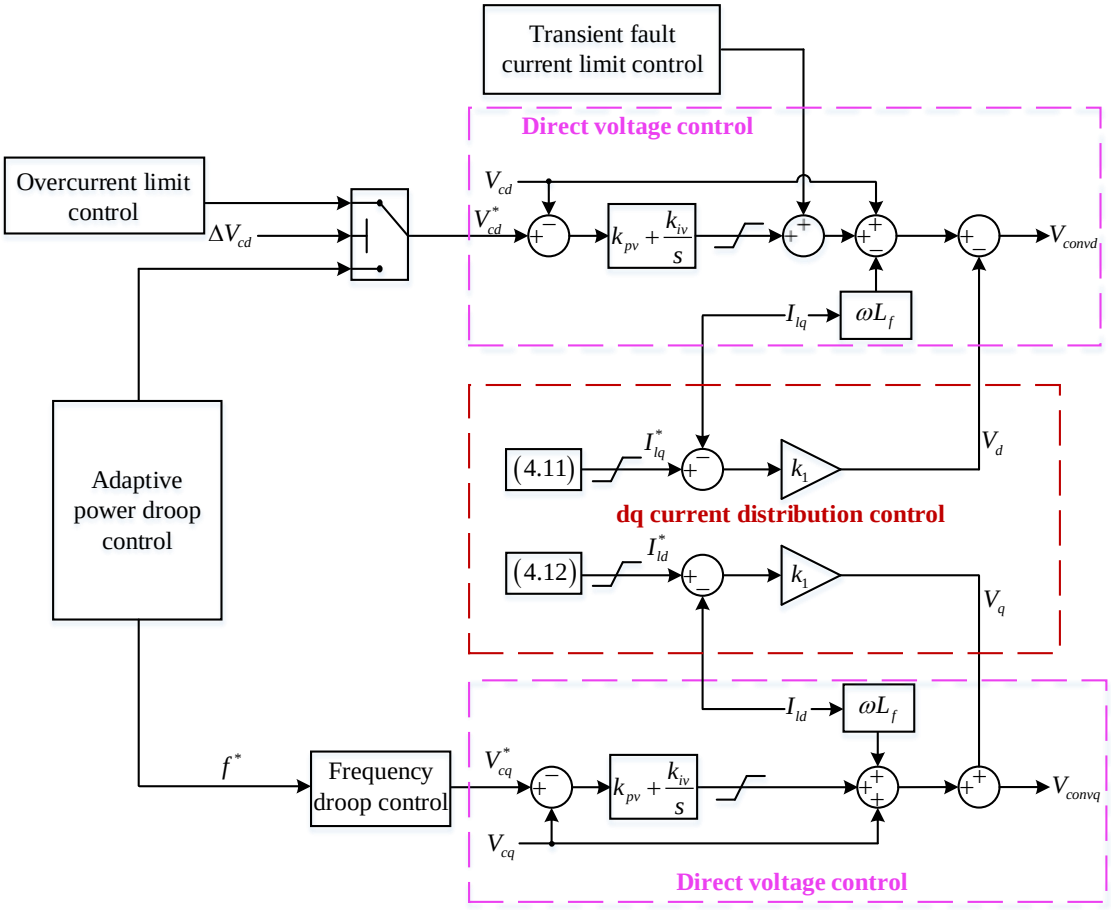

Fig. 4.10 Diagram of dq current distribution control

The mathematical expression of the dq current distribution control can be described as:

$$\begin{bmatrix} -V_d \\ V_q \end{bmatrix} = k_1 \begin{bmatrix} I_{lq}^* - I_{lq} \\ I_{ld}^* - I_{ld} \end{bmatrix} \tag{4.10}$$

where V_d and V_q represent the compensating voltage in the dq reference frame. k_1 refers to the proportional gain for the control scheme. The reactive current order I_{lq}^* can be given according to the voltage drop during fault as:

$$I_{lq}^* = k_{vi}\Delta V_{cd} \tag{4.11}$$

where k_{vi} is the proportional gain for the reactive current order. According to (4.11), a larger voltage sag ΔV_{cd} will lead to a larger reactive current order I_{lq}^{*} and vice versa. The profile of the active current order I_{ld}^{*} is determined by the reactive current and overall current, as:

$$I_{ld}^{*} = \begin{cases} \sqrt{\left|I_l\right|^2 - I_{lq}^{*2}}, & \left|I_l\right| \le 1.2\left|I_l^0\right| \\ \sqrt{1.2\left|I_l^0\right|^2 - I_{lq}^{*2}}, & \left|I_l\right| > 1.2\left|I_l^0\right| \end{cases} \tag{4.12}$$

On normal operation, the direct voltage controller takes the lead of the whole control system and the response produced by the dq current distribution controller will be compensated by the PI regulators in the direct voltage controller to ensure no conflict between the direct voltage control loop and the dq current distribution control loop. In the event of an AC fault during islanding or grid connection network, the dq current distribution controller will make the measured active and reactive current (I_{ld} and I_{lq}) to follow the current orders expressed in (4.11) and (4.12). As discussed previously, if the system is overloaded during islanded operation, the direct voltage control is retained to share the active and reactive current according to Ohm's Law, i.e., dependent on the load characteristic. In this scenario, the response produced by the dq current distribution controller are compensated by the PI regulators in the direct voltage controller.

4.7 Simulation results

To validate the feasibility and robustness of the proposed universal GFM control strategy, the system shown in Fig. 4.1 is tested by using a detailed model in MATLAB/Simulink environment. The VSC switching frequency is set at 2.5 kHz which is the typical level for IGBT in medium-high power application [24]. The DC side of the VSC is connected to a constant DC source of V_{dc}. Both grid connected and islanded operations for the universal GFM VSC are tested. The system and control parameters are stated in Table 4.1.

Table 4.1 System and control parameters

System initial parameters		
Power rating		400 kW
SCR		5
Nominal local load demand P_L		200 kW (0.5 pu)
Nominal frequency f^0 (ω_0)		50 Hz (100π rad/s)
DC voltage V_{dc}		1300 V
AC grid nominal voltage		690 V
LCL filter	Converter reactance L_f	0.2 pu
	Capacitance C	0.15 pu
	Terminal (transformer equivalent) reactance L_t	0.06 pu
Universal GFM VSC control parameters (pu)		
PLL	Proportional gain k_{ppll}	0.4
	Integral gain k_{ipll}	12.57
Adaptive power droop control	Active power reference P^*	1
	Reactive power reference Q^*	0
	Active power droop coefficient k_p	0.02
	Reactive power droop coefficient k_q	0.05
Direct voltage control	Proportional gain k_{pv}	0.9
	Integral gain k_{iv}	50
Frequency droop control	Droop coefficient k_f	1.598
Transient fault current limit control	Proportional gain k_d	2.437
Overcurrent limit control	Proportional gain k_o	9.242
dq current distribution control	Proportional gain k_1	0.697
	Proportional gain for reactive current order k_{vi}	-1.4

4.7.1 Grid connected operation

To verify the robustness of the universal GFM control strategy on grid connected operation, three cases are illustrated including grid frequency change, load step and external balanced AC faults.

A. Grid frequency change

To validate the system response during grid connected operation, the grid frequency is increased to 50.2 Hz (with a frequency rise of 0.004 pu) during 1 s - 1.5 s using the model in Fig. 4.1. The simulation results are depicted in Fig. 4.11.

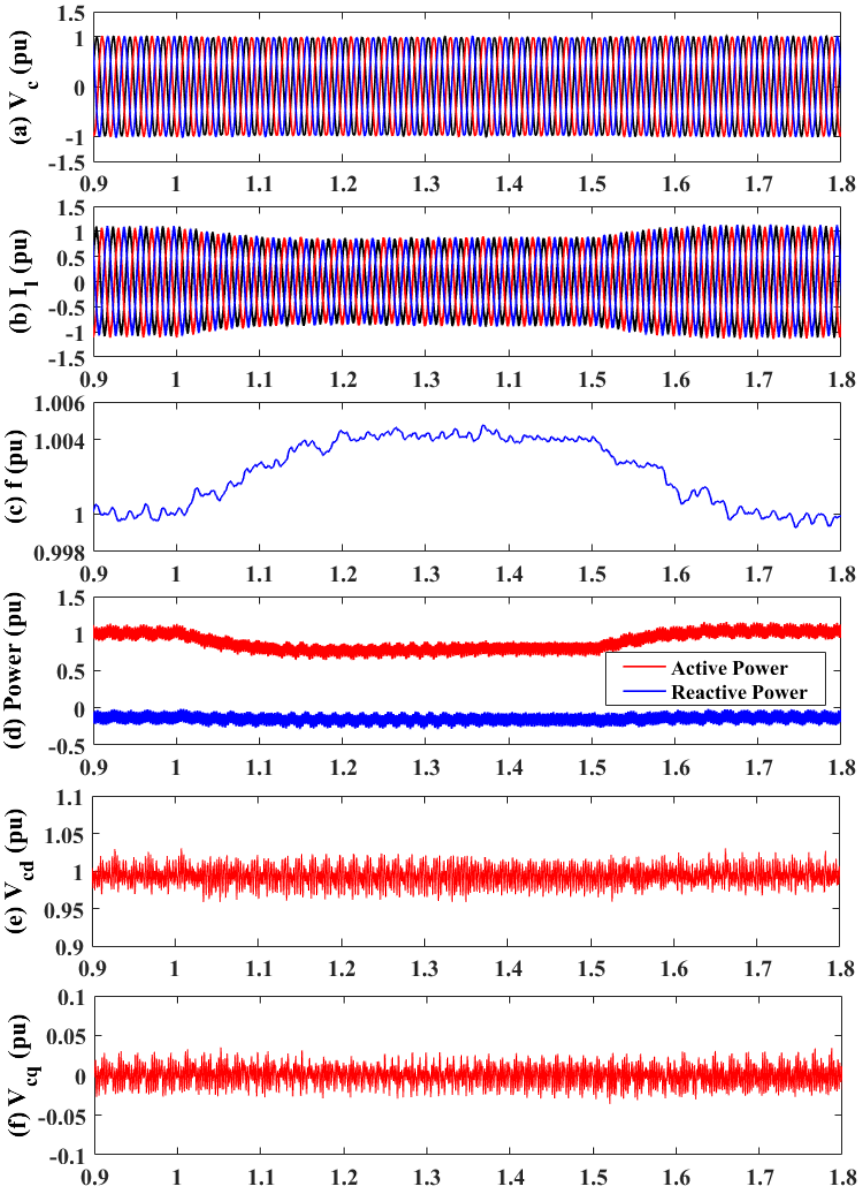

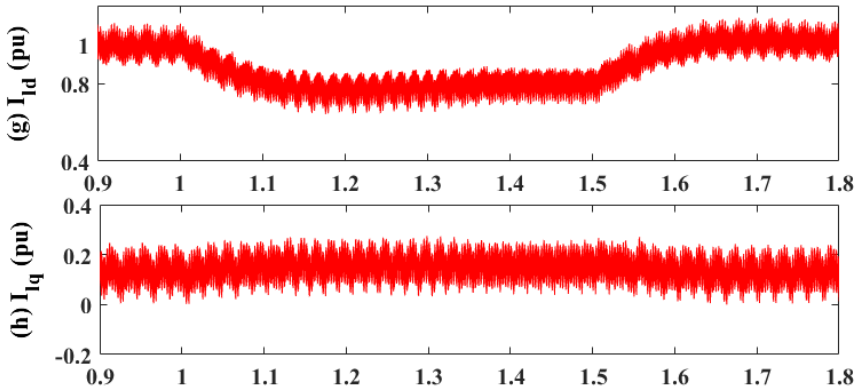

Fig. 4.11 Waveforms of grid frequency rise (a) Converter filter bus voltage (b) Converter output current (c) Frequency (d) Delivered power (e) d-axis converter filter bus voltage (f) q-axis converter filter bus voltage (g) d-axis converter output current (h) q-axis converter output current

When the network frequency increases, the angle shift between the converter output voltage and PCC voltage reduces. Consequently, the output power from the converter is reduced. Thus, according to the active power droop controller in (4.5), the frequency reference f^* for the VSC is increased. As shown in Fig. 4.11, the system frequency rises to 1.004 pu (50.2 Hz), while the active power drops to around 0.78 pu that is determined by the droop constant k_p .The AC voltage is well controlled at 1 pu, and the reactive power is largely unchanged, as depicted in Fig. 4.11 (d) and (h). Due to the reduction of active power, the converter output current drops to 0.8 pu, as can be seen in Fig. 4.11 (b). When the grid frequency recovers back to 1 pu (50 Hz), all the converter variables restore quickly to the normal levels.

B. Load step

As shown in Fig. 4.12, an additional load Z_a (0.25 pu, 100 kW) is switched in and off at 2 s and 2.5 s, respectively. The simulation results are displayed in Fig. 4.13.

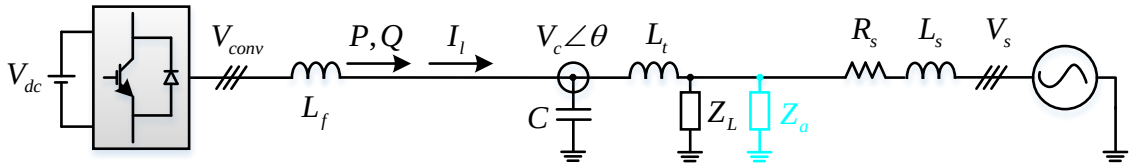

Fig. 4.12 System configuration of load steps test on grid connected operation

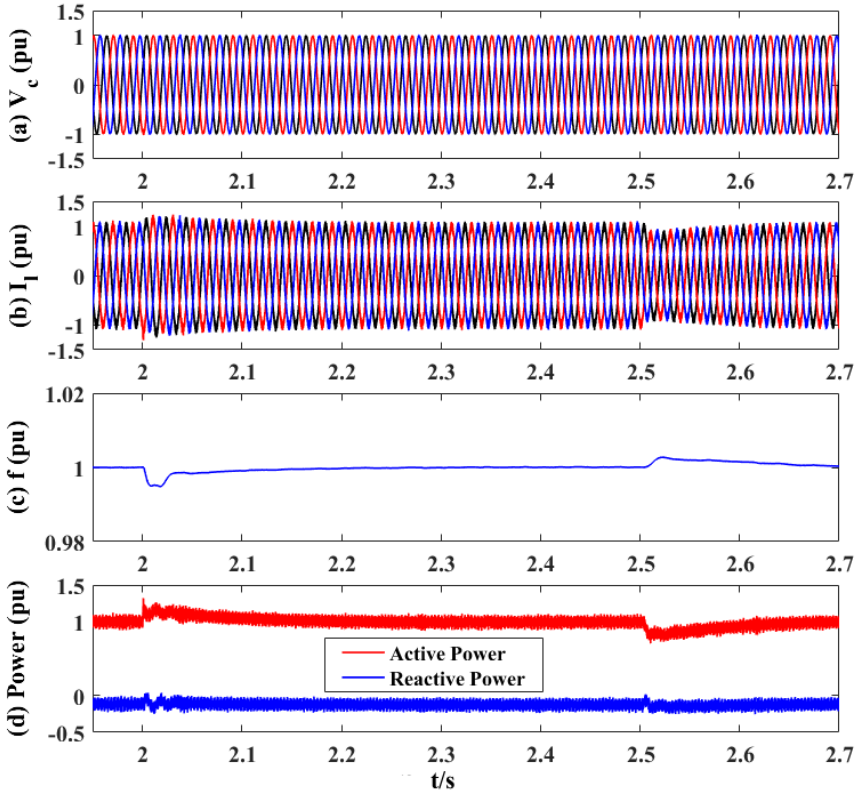

Fig. 4.13 Waveforms of load steps on grid connected operation (a) Converter filter bus voltage (b) Converter output current (c) Frequency (d) Delivered power

As shown in Fig. 4.13 (a), the AC voltage at the converter filter bus remains well-controlled before, during and after the load steps due to the operation of the direct voltage controller. The converter reactive power is slightly different to the reference value due to the small difference between the actual AC voltage and AC voltage setpoint/reference. As the network frequency is 50 Hz which is the same as the nominal frequency in the active power controller, the VSC generates zero active power error, i.e., the actual active power is the same as the reference of 1.0 pu, as can be seen in Fig. 4.13 (d). The converter output current and generated power settle down to the steady-state quickly after a tiny disturbance as displayed in Fig. 4.13 (b) and (d). According to Fig. 4.13 (c), the frequency

is also maintained at 1 pu after a small overshoot which is caused by the transient of load switching. The simulation results verify the stable operation of the universal GFM VSC control strategy under load step during grid connected operation.

C. External balanced AC fault

To test the fault ride-through operation of the proposed controller with grid connected, a three-phase-to-ground fault with a fault resistance of 0.01 Ω is induced into the system during 3.2 s - 3.5 s at the location of F shown in Fig. 4.14. As the fault resistance is extremely small, the voltage is almost reduced to 0 during the fault. The simulation results on this case are displayed in Fig. 4.15.

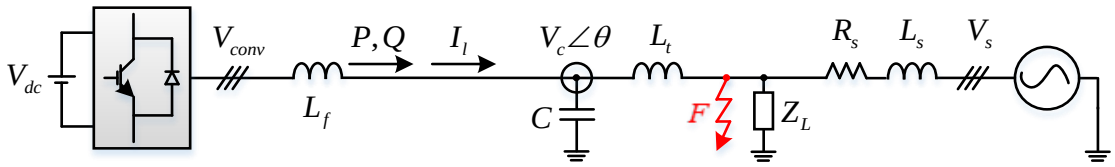

Fig. 4.14 System configuration of an AC fault test on grid connected operation

As illustrated in Fig. 4.15, the converter filter bus voltage V_c drops to about 0 pu during the fault, while the converter output fault current is largely limited at the pre-set level 1.2 pu with a transient current peak of 1.5 pu at the inception of the fault due to the operation of the transient fault current limit and overcurrent limit controllers. The frequency is remained at 1 pu resulted from the effective operation of PLL, while the active and reactive power are 0 during the fault due to the zero AC voltage. According to Fig. 4.15 (e) and (f), the d-axis voltage V_{cd} drops to 0, while PLL still effectively forces the q-component voltage V_{cq} to be 0 to avoid the excursion of the frequency and phase angle during the fault. As shown in Fig. 4.15 (g) and (h), the active current I_{ld} and reactive current I_{lq} are controlled at 0.5 pu and -1.05 pu (capacitive) respectively with respect to (4.11) and (4.12) during the fault, which is the result of the effective operation of the dq current distribution controller. After the clearance of the fault, the converter filter bus voltage, converter output current, frequency and delivered power quickly recover back to the normal levels.

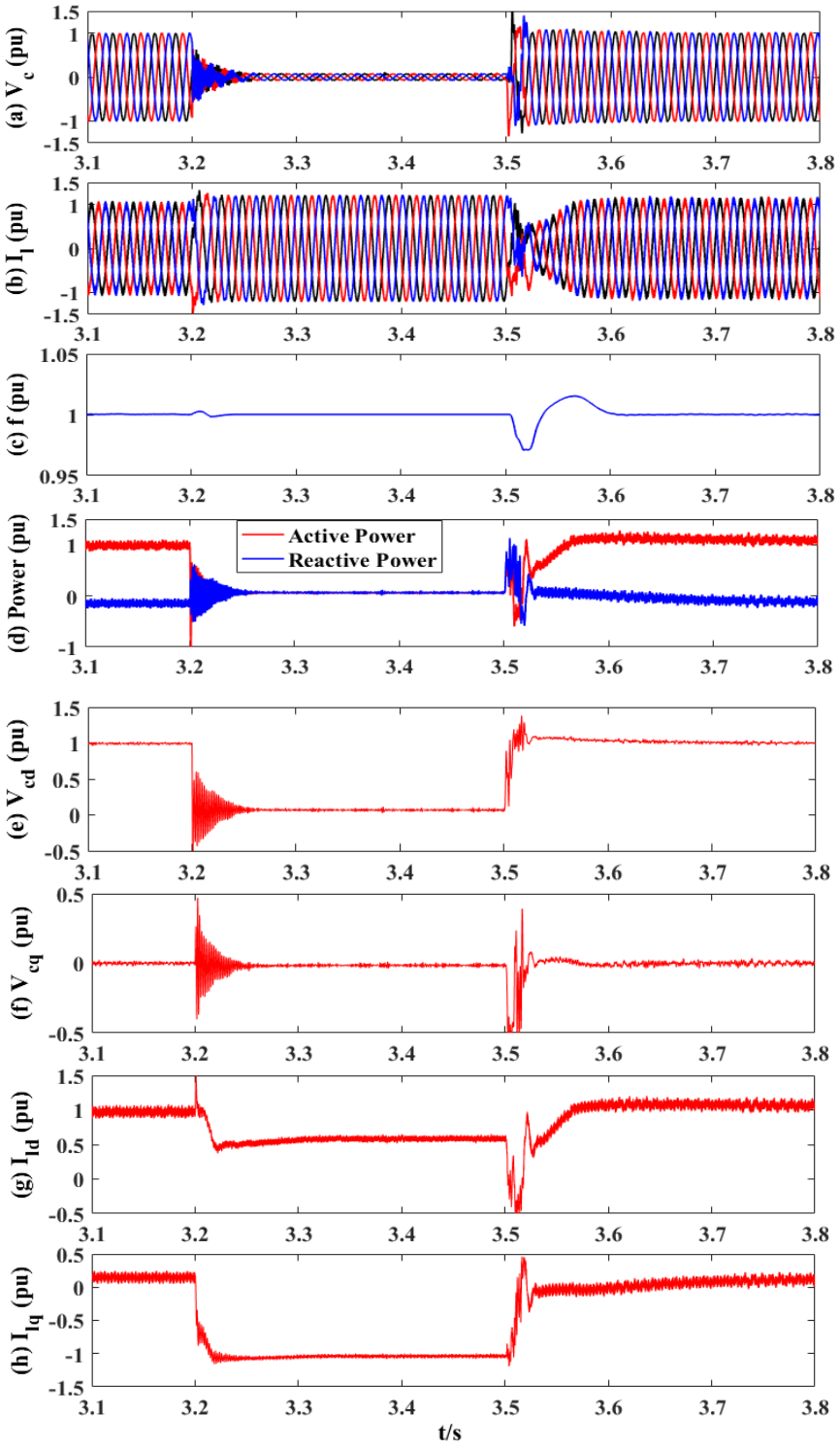

Fig. 4.15 Waveforms of an AC fault with fault voltage level at 0 pu on grid connected operation: (a) Converter filter bus voltage (b) Converter output current (c) Frequency (d) Delivered power (e) d-axis converter filter bus voltage (f) q-axis converter filter bus voltage (g) d-axis converter output current (h) q-axis converter output current

For a higher fault resistance, the retaining AC voltage during the fault will be higher. Fig. 4.16 shows the simulated results during a balanced AC fault with a fault resistance 0.1 Ω applied at the location of F during 4 s - 4.3 s. As shown in Fig. 4.16, the converter filter bus voltage V_c drops to 0.5 pu during the fault, while the fault current is limited at the pre-set level 1.2 pu with a current spike of 1.4 pu. The frequency settles back to 1 pu quickly after a small overshoot. As shown in Fig. 4.16 (g) and (h), the active current I_{ld} is controlled at 0.9 pu, while the reactive current I_{lq} is regulated at -0.8 pu according to (4.11) and (4.12). Consequently, the delivered active power drops to 0.4 pu, while the reactive power is increased to 0.4 pu (capacitive). After the clearance of the fault, the converter filter bus voltage, converter output current and frequency quickly recover, which indicates a good postfault operation.

According to the simulation results, it can be seen that the proposed current limit control is robust for different fault resistances during grid connected operation.

4.7.2 Transition from grid connected operation to islanded operation

The system shown in Fig. 4.1 is disconnected from the AC grid by opening the Switch S at 5 s to test the behaviour of transition from grid connected operation to islanded operation. The simulation results are displayed in Fig. 4.17. As shown, the converter filter bus voltage remains well-controlled without any noticeable disturbance during and after the transient. As all the generated active power is transmitted into the local load (200 kW, 0.5 pu) on islanded operation, the delivered active power and converter output current drops to 0.5 pu after islanding. Considering the characteristics of the active power droop controller discussed previously, the GFM VSC slightly increases its frequency to decrease the generated active power from reference value of 1.0 pu to 0.5 pu. As seen from Fig. 4.17 (c), the frequency increases to 1.01 pu after a short oscillation, which corresponds to 0.5 pu active power reduction with the droop constant of 0.01 pu. As shown in Fig. 4.17 (d), the VSC consumes some inductive reactive power although the local load is purely resistive. This is because that the VSC needs to compensate the difference of reactive power generated by the filter capacitor (0.15 pu) and that consumed by the terminal reactance L_f (0.06 pu).

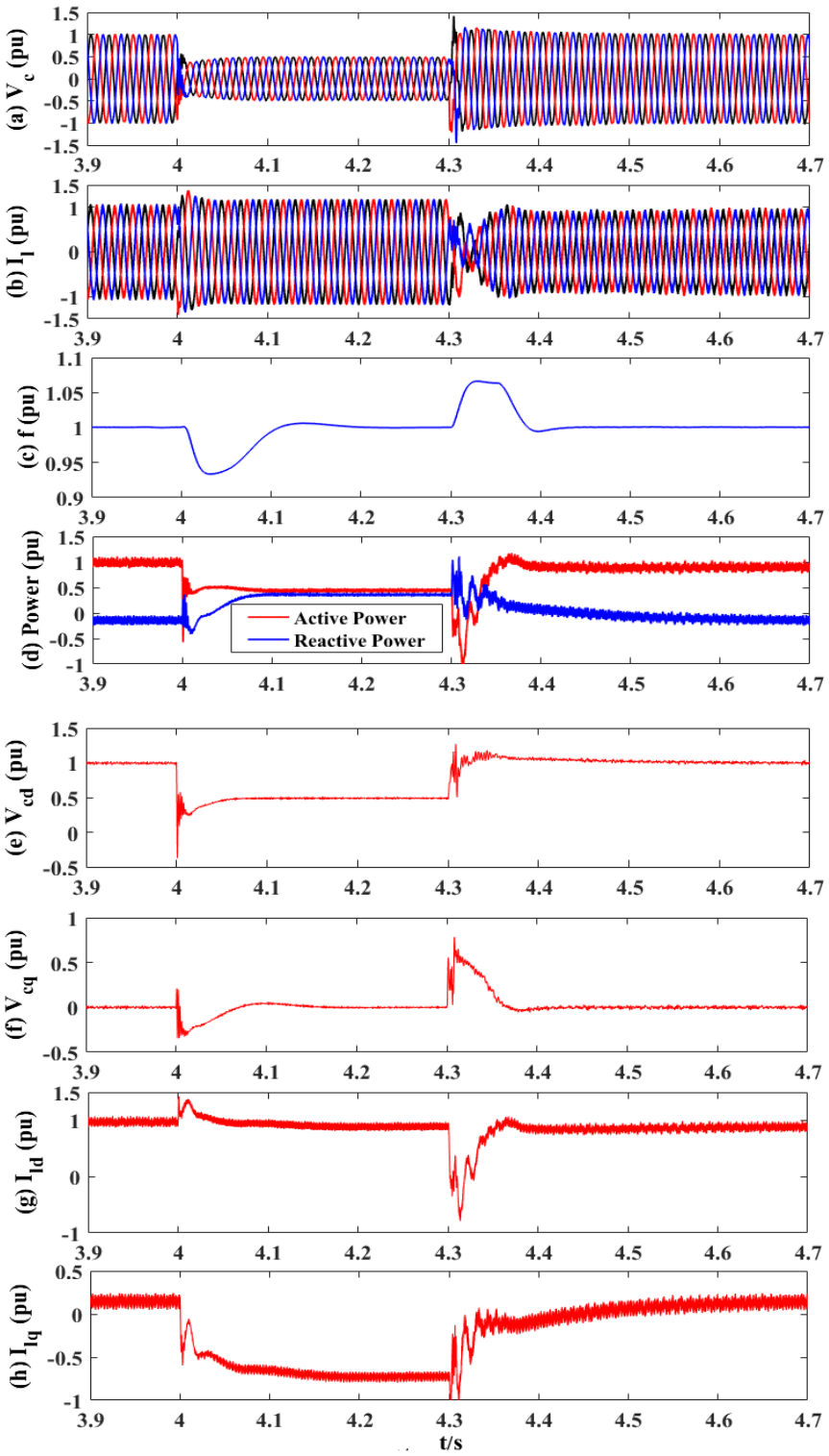

Fig. 4.16 Waveforms of an AC fault with fault voltage level at 0.5 pu on grid connected operation (a) Converter filter bus voltage (b) Converter output current (c) Frequency (d) Delivered power (e) d-axis converter filter bus voltage (f) q-axis converter filter bus voltage (g) d-axis converter output current (h) q-axis converter output current

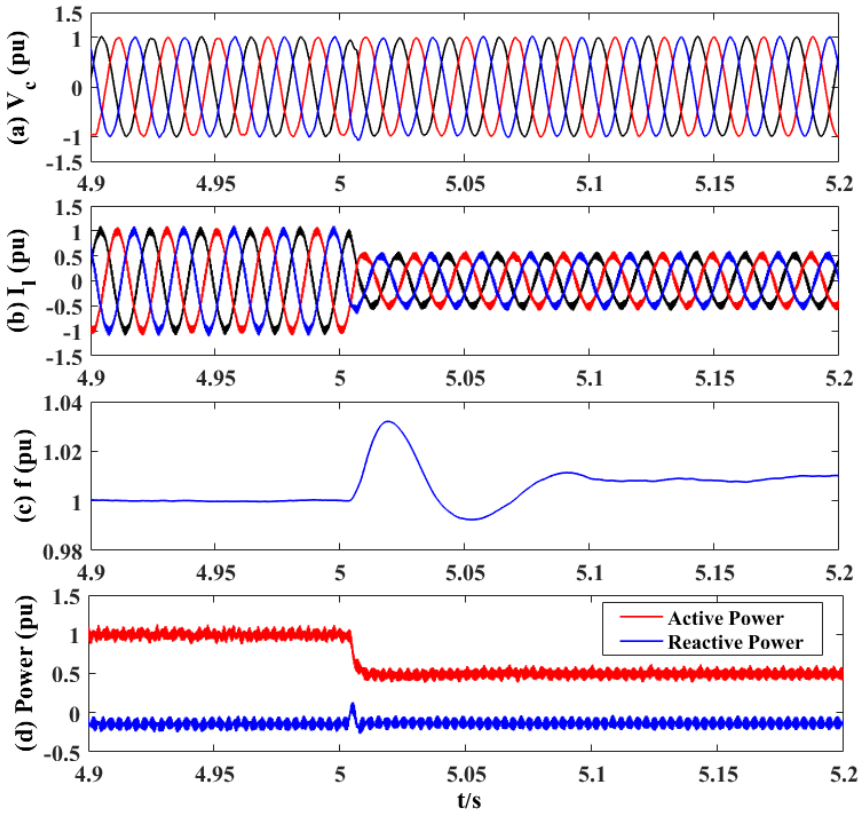

Fig. 4.17 Waveforms of transition from grid connected operation to islanded operation (a) Converter filter bus voltage (b) Converter output current (c) Frequency (d) Delivered power

The simulation results depicted in Fig. 4.17 verify that the proposed universal GFM control strategy provides a smooth transition from grid connected operation to islanded operation without the need for control mode switching.

4.7.3 Islanded operation

To further validate the feasibility of the proposed control strategy when operating as an island network, three cases are tested including load steps, overloaded condition and external balanced AC fault.

A. Load step

As shown in Fig. 4.18, the system operates in islanded mode and an additional load Z_a (0.25 pu, 100 kW) is switched in and off at 5.5 s and 5.8 s, respectively. The simulation

results are depicted in Fig. 4.19. As shown in Fig. 4.19, the AC voltage at the converter filter bus is well-controlled during and after the load step. As the total demand of the load is increased to 0.75 pu at 5.5 s, the delivered active power and converter output current quickly rise to 0.75 pu. The frequency drops slightly from 1.01 pu to about 1.005 pu due to the operation of active power droop controller as seen in Fig. 4.19 (c). Since the additional load is purely resistive, there is limited change on the reactive power and reactive current, as seen in Fig. 4.19 (d) and (h). At 5.8 s, the additional load is disconnected, the active power and converter output current quickly return to 0.5 pu while the frequency also goes back to 1.01 pu. The simulation results indicate a satisfactory response during load steps for the universal GFM VSC on islanded operation.

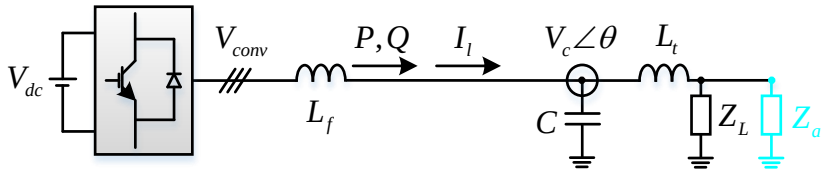

Fig. 4.18 System configuration of load steps on islanded operation

B. Overloaded condition

To validate the feasibility of the dq current distribution on islanded operation during overloaded condition, an additional load Z_a (400 kW / 1 pu and 100 kVar / 0.25 pu) is switched in and out at 6.1 s and 6.4 s, respectively. The simulation results are depicted in Fig. 4.20.

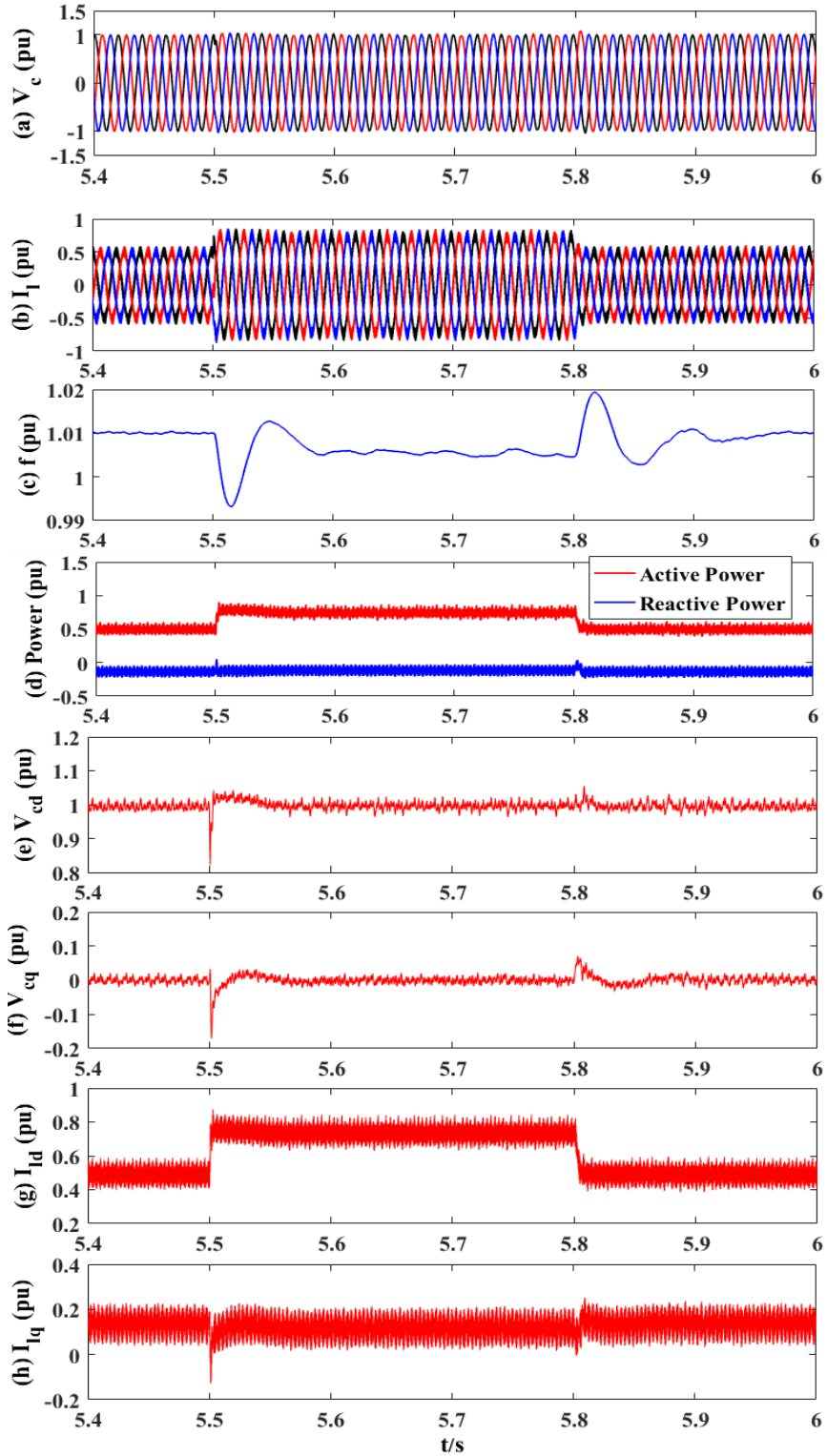

Fig. 4.19 Waveforms of load step on islanded operation (a) Converter filter bus voltage (b) Converter output current (c) Frequency (d) Delivered power (e) d-axis converter filter bus voltage (f) q-axis converter filter bus voltage (g) d-axis converter output current (h) q-axis converter output current

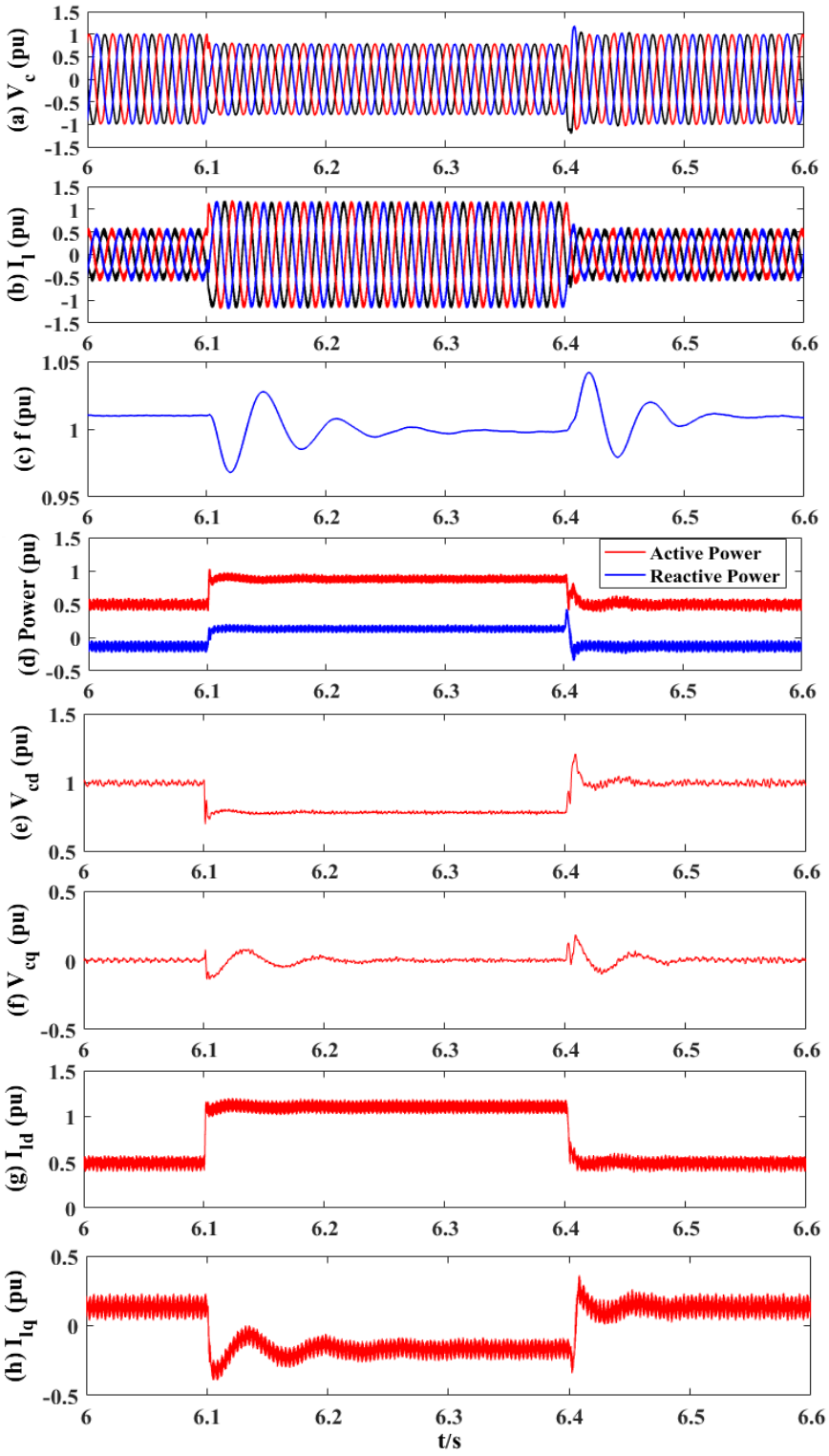

Fig. 4.20 Waveforms of overload on islanded operation (a) Converter filter bus voltage (b) Converter output current (c) Frequency (d) Delivered power (e) d-axis converter filter bus voltage (f) q-axis converter filter bus voltage (g) d-axis converter output current (h) q-axis converter output current

As the initial load is 200 kW / 0.5 pu, the switching in of the additional load at 6 s causes the VSC to be overloaded. During the overloaded condition, the overcurrent limit controller operates to limit the converter output current, and then to drop the voltage reference V_{cd}^{*} for the direct voltage controller. As displayed in Fig. 4.20 (a), (b) and (e), the converter filter bus voltage drops to 0.8 pu, while the converter output current is limited at around 1.2 pu. Since the converter filter bus voltage drops to 0.8 pu, the active and reactive current go to around 1.18 pu and 0.2 pu according to Ohm's Law, as shown in Fig. 4.20 (g) and (h). Hence, the generated active and reactive power settle down at around 0.9 pu and 0.16 pu according to the power flow equation (3.6) and (3.7), as illustrated in Fig. 4.20 (d). The frequency is around 1 pu according to the active power droop controller, while the q-axis voltage V_{cq} is 0 pu due to the operation of PLL, as depicted in Fig. 4.20 (c) and (e). When the additional load is switched off, the system returns to normal operation quickly.

The simulation results displayed in Fig. 4.20 validate that the proposed overcurrent limit control can effectively limit the overall current and provide the sharing of active and reactive currents according to the local loads when the converter is overloaded during islanded operation.

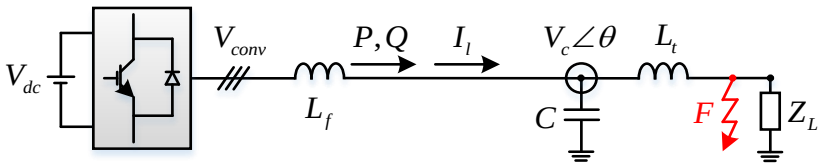

Fig 4.21 System configuration of an external AC fault on island network

C. External balanced AC fault

A balanced AC fault with a fault resistance of 0.01 Ω is simulated during 7 s- 7.3 s at the location of F shown in Fig 4.21, and the simulation results are shown in Fig. 4.22. As illustrated in Fig. 4.22, the AC voltage at the converter filter bus drops to almost 0 during the fault. The overcurrent is largely limited at 1.2 pu through the transient fault current limit controller and the overcurrent limit controller. Since the AC voltage drops to around 0 and the system is under zero voltage network, there are not active and reactive

power exported from the converter. Meanwhile, PLL locks the frequency at 1.01 pu. According to Fig. 4.22 (g) and (h), the active current is controlled at 0.4 pu, while the reactive current goes to 1.1 pu during the fault. This is because the dq distribution controller provides active and reactive current reference according to the voltage dip given in (4.11) and (4.12). As the fault is very severe and voltage dip is extremely large, the reactive current reference is limited at 1.1 pu by the saturation block, while the active current reference is set at 0.4 pu considering the fault current level (1.2 pu). And then the current references are followed by their respective measured current with respect to (4.10). When the fault is cleared, the converter restores quickly to the normal operation.

The simulation results depicted in Fig. 4.22 verifies that the proposed current limit controller provides good overcurrent protection and effective distribution of active and reactive current during an external AC fault when islanding.

4.8 Summary

In this chapter, a universal GFM VSC control strategy is proposed for grid connected and islanded operation with effective overcurrent limit control. The general control schemes include adaptive power droop, frequency droop, PLL, direct voltage and current limit controller. On grid connected operation, the VSC works as a controlled AC voltage source synchronised to the grid by PLL for the power exchange with the local load and AC grid. When the network becomes islanding, the VSC establishes the voltage and frequency for the network by the GFM direct voltage controller and frequency droop controller to provide a stable islanded operation.

To verify the operation of the proposed control strategy on grid connection, system responses during grid frequency change, load step and external AC fault are tested. The simulation results validate that the converter can operate adequately during grid frequency change and load step, and the proposed current limit controller can effectively limit the fault current and distribute the active and reactive currents according to the set current references.

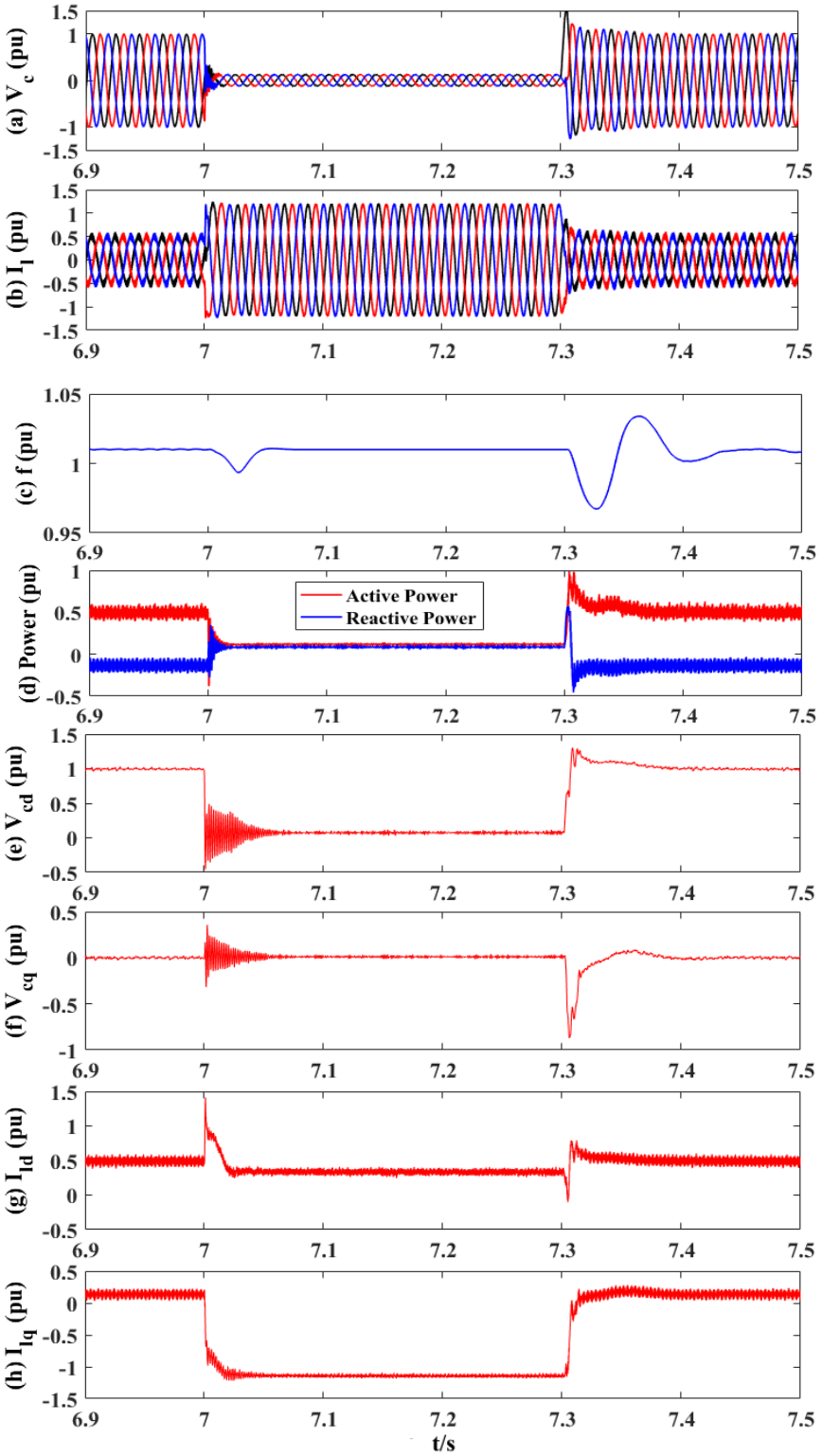

Fig. 4.22 Waveforms of an external AC fault on islanded network: (a) Converter filter bus voltage (b) Converter output current (c) Frequency (d) Delivered power (e) d-axis converter filter bus voltage (f) q-axis converter filter bus voltage (g) d-axis converter output current (h) q-axis converter output current

To verify the operation of the proposed control strategy on islanded operation, simulation during transition from the grid connected operation to islanded operation is carried out, and the results indicate smooth operation without control mode switching. Load step, overloaded operation and external AC fault are tested when the system is in islanded mode. The simulation results demonstrate that the converter can tightly control the AC voltage and frequency, and generate power with respect to the demand of the local loads during steady-state and load steps. The overall current limit controller can effectively limit the overcurrent and control the active and reactive current during overload or external fault conditions.

Although the proposed control strategy is able to deal with the transient events on both grid connection and islanding network, there are still some issues to be addressed. The current control loop only considers symmetrical AC faults, which makes the system lack the capability of dealing with asymmetrical faults. Another issue come out of the dq current distribution control loop. As mentioned previously, the produced response of the dq current distribution control loop due to the mismatch of the generated reactive current order and measured reactive current can be compensated by the PI regulators in the direct voltage controller. This can only be achieved when the grid is strong enough. In other words, when the connected grid becomes weak, the corresponding response can lead the system to be unstable due to the constraint of current control loop on a weak network, which will be validated in Chapter 5.

Chapter 5 Control of grid-forming VSC during symmetrical and asymmetrical AC faults

As discussed in Chapter 4, the universal GFM VSC control combines the advantages of conventional GFL and GFM VSCs for stable grid connected and islanded operation. During fault, the transient fault current limit controller operates to limit the transient fault current, while the overcurrent limit controller performs for the overall fault current limiting. The dq current distribution controller will set current orders according to the voltage dip and overall current level to ensure adequate the active and reactive current sharing. Nevertheless, since the mentioned current controllers only control the positive-sequence current terms, the operations during asymmetrical AC faults need to be further investigated.

Based on the control system introduced in Chapter 4, this chapter develops an enhanced AC fault current limit control scheme including the enhanced dq current distribution control and negative-sequence component current control, to limit and control the current during fault conditions. To enable the separated control of positive- and negative-sequence components, the control schemes are built in double synchronous reference frames. The proposed control strategy has the capability to deal with symmetrical and asymmetrical faults and can restore normal operation quickly. To verify the feasibility of the proposed control strategy, time-domain simulations are carried out in MATLAB/Simulink environment.

5.1 Overall system control

As shown in Fig. 5.1, the overall control system is divided into two parts, including the general GFM control, and enhanced AC fault current limit control that consists of the voltage balancing control, enhanced dq current distribution control and negative-sequence current control. The general GFM control is based on the control strategies introduced in Chapter 4 with partial controlling variables being filtered by notch filters to extract the positive-sequence components. To address challenges related to AC faults on a weak network (i.e., the external AC voltage is not stiff), the voltage balancing control

and enhanced dq current distribution control are developed. It is worth mentioning that they are different from the AC fault current control discussed in Chapter 4, and the details will be discussed in the following sections. In addition, a negative-sequence current control strategy is employed in this chapter to deal with asymmetrical faults.

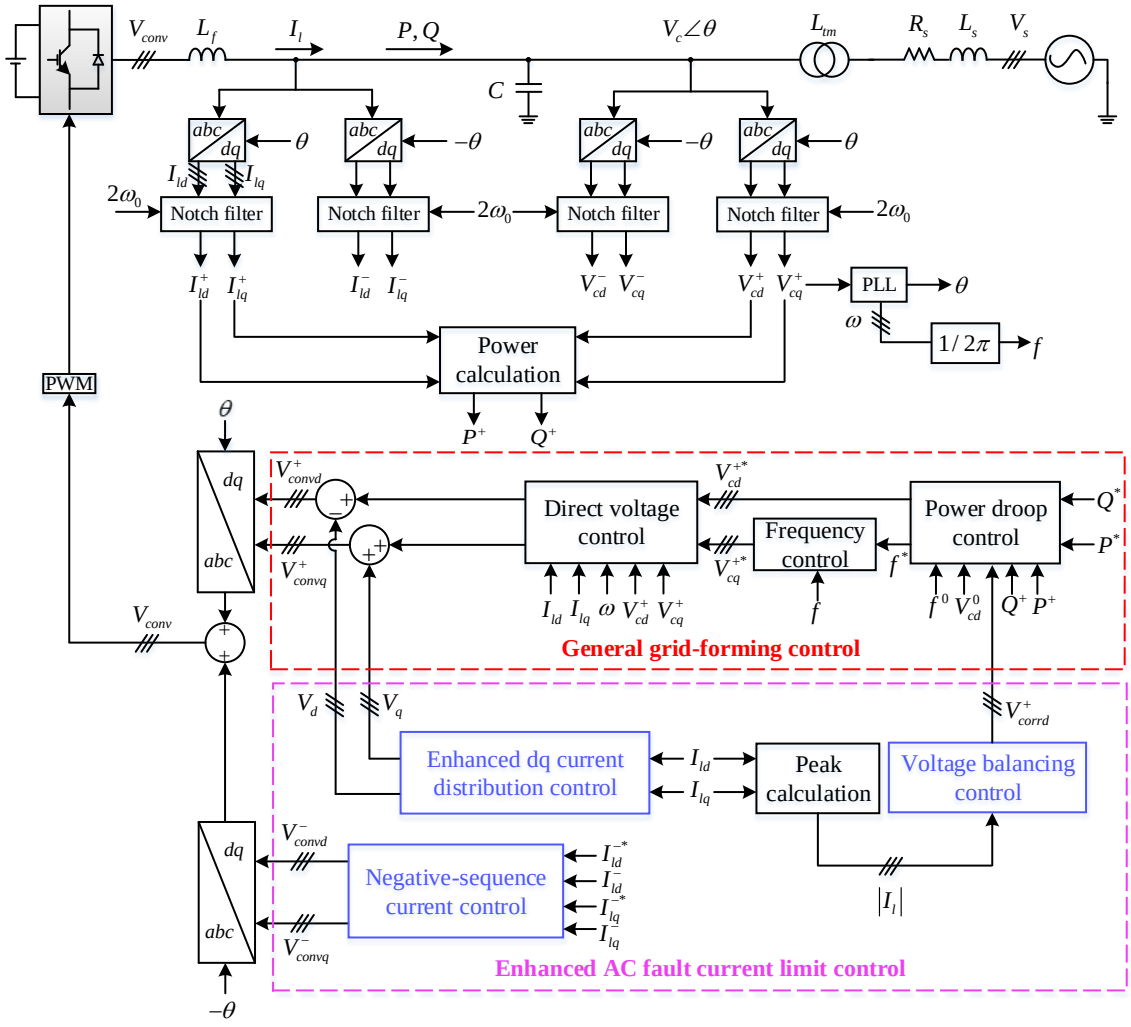

Fig. 5.1 overall control system of the GFM VSC on grid connection

5.2 General GFM control

The general GFM control module is based on the control schemes discussed in Chapter 4, including direct voltage control, frequency droop control, PLL and adaptive power droop control. Different from the control schemes in Chapter 4, there are two dq frames (positive- and negative-sequence dq reference frames) used in this chapter. Some control

parameters are implemented in both positive- and negative-sequence dq reference frames, which will be introduced later in this section.

5.2.1 Double synchronous reference frames

To facilitate precise control of the GFM VSC for positive- and negative-sequence component variables, double synchronous reference frames are adopted in this chapter. Under unbalanced conditions, a three-phase variable without zero-sequence component can be decomposed as:

$$F_{abc}(t) = F_{abc}^{+}(t) + F_{abc}^{-}(t) \tag{5.1}$$

where $F_{abc}(t)$ refers to the three-phase voltage or current, while F_{abc}^{+} and F_{abc}^{-} represent the corresponding positive- and negative-sequence voltage or current components, respectively.

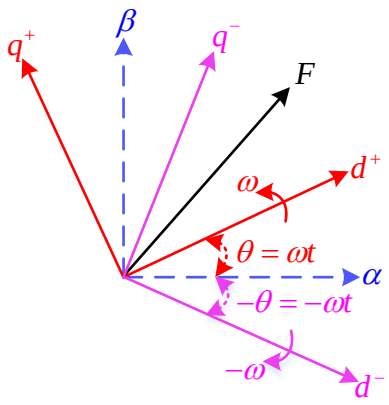

Fig. 5.2 Vector F in the positive dq$_+$ and negative dq$_-$ reference frames

It is convenient to model the converter by using a positive reference frame rotating at the speed of ω and a negative reference frame rotating at the speed of $-\omega$ during grid unbalanced conditions [149], [156], [157], which is displayed in Fig. 5.2. Thus, the relationship between the representations of F in the dq$_+$ and dq$_-$ reference frames can be described as [149], [156], [157]:

$$\begin{aligned} F_{dq+} &= F_{dq-} \cdot e^{-j2\theta} \\ F_{dq-} &= F_{dq+} \cdot e^{j2\theta} \end{aligned} \tag{5.2}$$

It is worth mentioning that the negative-sequence components will appear as double-frequency components in the positive-sequence frame, and vice versa. Hence, notch filters are commonly used to remove the double-frequency components to separate the positive- and negative-sequence components from the measured variables of the VSC, and the transfer function of a typical notch filter can be expressed as:

$$G_{nf}(s) = \frac{s^2 + 4\omega_0^2}{s^2 + 4\xi_{nf} s + 4\omega_0^2} \tag{5.3}$$

where s and ξ_{nf} are the Laplace operator and the damping ratio, respectively. ω_0 is the nominal angular frequency of the network. After the separation of the positive- and negative-sequence components, it is much more straightforward to control the positive- and negative-sequence voltage and current independently.

5.2.2 Direct voltage control in the positive-sequence reference frame

Different from the direct voltage control loop in Chapter 4, the positive-sequence converter filter bus dq-axes voltages are controlled through PI regulators, while the negative-sequence dq-axes voltages are only determined by the negative-sequence current controller when the network becomes unbalanced. Hence, the direct voltage control dynamics in the positive-sequence dq reference frame can be expressed as:

$$\begin{cases} V_{convd}^{+} = k_{pv}\left(V_{cd}^{+*} - V_{cd}^{+}\right) + k_{iv}\int\left(V_{cd}^{+*} - V_{cd}^{+}\right)dt - \omega I_{lq} L_f + V_{cd} \\ V_{convq}^{+} = k_{pv}\left(V_{cq}^{+*} - V_{cq}^{+}\right) + k_{iv}\int\left(V_{cq}^{+*} - V_{cq}^{+}\right)dt + \omega I_{ld} L_f + V_{cq} \end{cases} \tag{5.4}$$

where the variables with superscript "+" and "*" denote the positive-sequence components and control orders for the direct voltage controller, respectively. Notch filters can introduce magnitude error and phase shift to the original inputs, which can have adverse impact on system performance. Thus, as seen in (5.4), the decoupling and feedforward terms are not processed by the notch filters (i.e., the compensation terms contain both positive and negative sequence components represented in the positive dq+ frame), which is to ensure accurate feedforward compensation. The control diagram of the direct voltage controller is illustrated in Fig. 5.3.

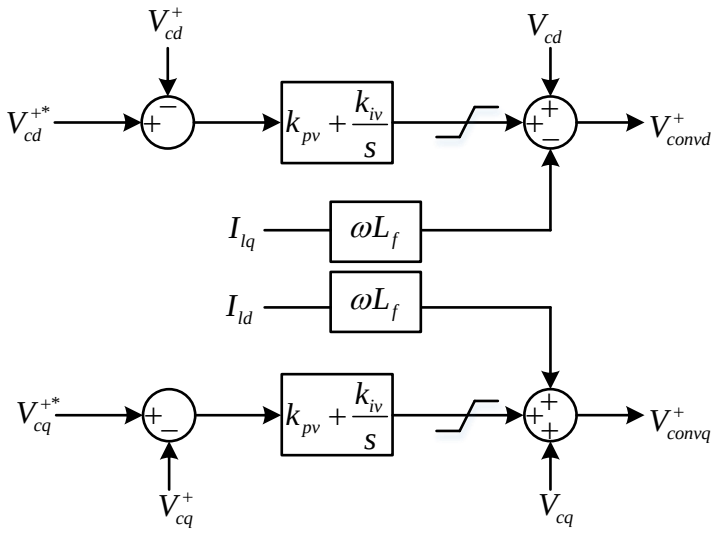

Fig. 5.3 Control diagram of the direct voltage controller

5.2.3 Adaptive power droop control in the positive-sequence reference frame

As the voltage orders V_{cdq}^{+*} fed into the direct voltage controller in this chapter are in the positive-sequence components, the active P^{+} and reactive power Q^{+} used in this chapter are also measured in the positive-sequence components to avoid the adverse impact of the second-harmonic components on the direct voltage controller during unbalanced network conditions, which can be expressed as:

$$\begin{cases} P^{+}=1.5\left(V_{cd}^{+}I_{ld}^{+}+V_{cq}^{+}I_{lq}^{+}\right) \\ Q^{+}=1.5\left(V_{cq}^{+}I_{ld}^{+}-V_{cd}^{+}I_{lq}^{+}\right) \end{cases} \tag{5.5}$$

Based on the principle of the adaptive power droop controller discussed in Chapter 4, the expression of the adaptive power droop controller in the positive-sequence components can be obtained as:

$$\begin{cases} V_{cd}^{+*}=V_{cd}^{0}-k_q\left(Q^{*}-Q^{+}\right) \\ f^{*}=\begin{cases} f^{0}+k_p(P^{*}-P^{+}), & \text{when } \dfrac{V_{cd}^{+}}{0.9V_{cd}^{0}}\geq\dfrac{P^{*}}{P^{0}} \\ f^{0}+k_p(P^{*}\dfrac{V_{cd}^{+}}{0.9V_{cd}^{0}}-P^{+}), & \text{when } \dfrac{V_{cd}^{+}}{0.9V_{cd}^{0}}<\dfrac{P^{*}}{P^{0}} \end{cases} \end{cases} \tag{5.6}$$

The control diagram of the described adaptive power droop control can be displayed in Fig. 5.4. In Chapter 4, the adaptive power droop control is mainly used for frequency and active power regulation. In this chapter, the reactive power droop control loop plays the main role in reactive power compensation for the GFM VSC to provide AC voltage support on a weak network. When the connected AC grid becomes weak and delivered active power is maintained at a high level (e.g. 1 pu), the converter will increase its reactive power to support the converter output voltage for bulk active power generation.

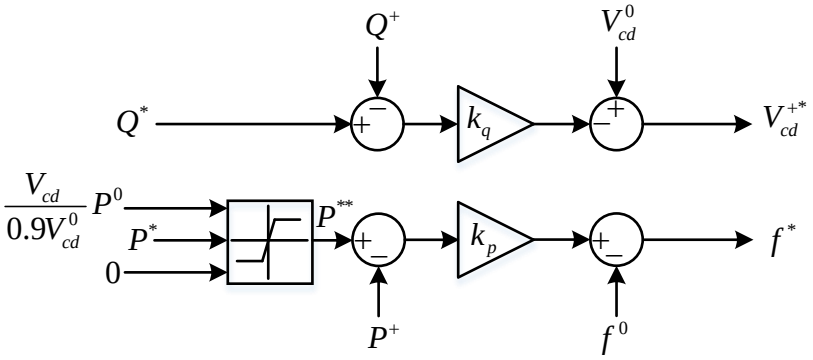

Fig. 5.4 Diagram of the adaptive power droop control

5.2.4 PLL in the positive-sequence reference frame

Since there are two dq reference frames used in this chapter, a notch filter is used in PLL discussed in Chapter 4 as shown in Fig. 5.5 to extract the positive-sequence converter filter bus voltage V_{cq}^+, so as to estimate the phase angle θ and frequency f of the network. According to Fig. 5.5, the frequency estimated by PLL can be expressed as:

$$f = f^0 + k_{ppll}V_{cq}^+ + k_{ipll}\int V_{cq}^+ dt \tag{5.7}$$

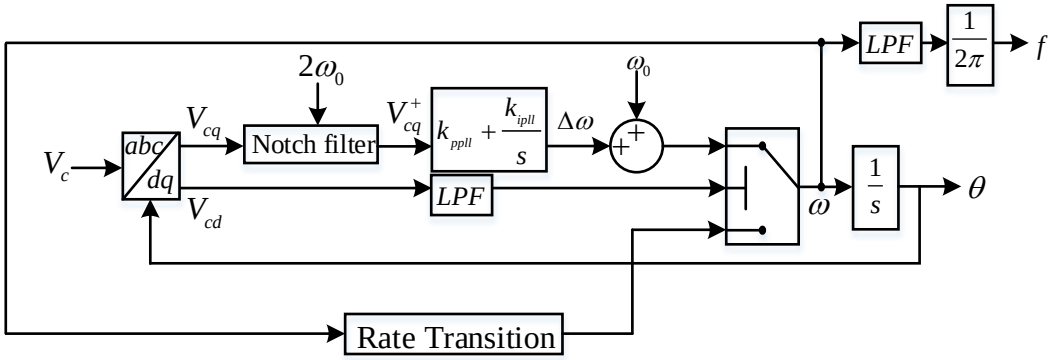

Fig. 5.5 Diagram of PLL

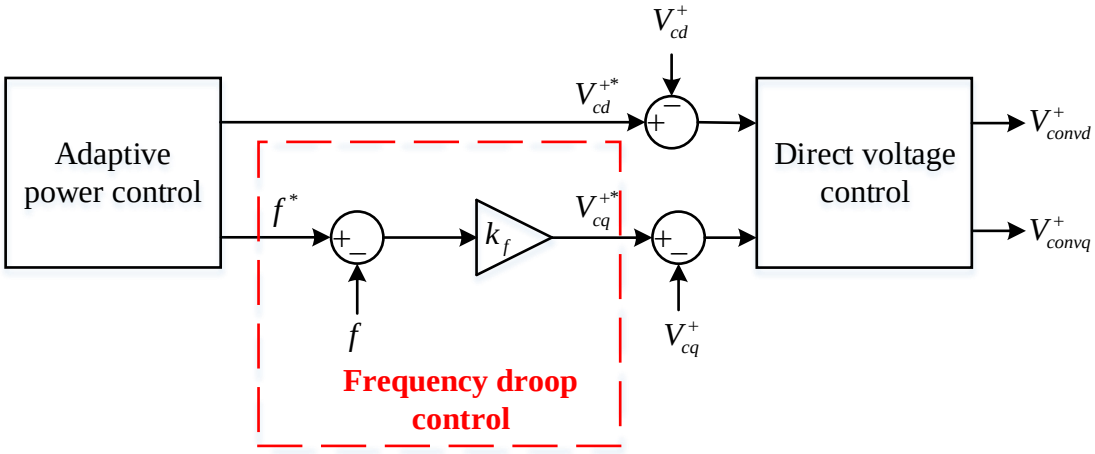

Fig. 5.6 Diagram of the frequency droop control

5.2.5 Frequency droop control in the positive-sequence reference frame

The frequency droop control discussed in Chapter 4 is developed to establish the system frequency while islanding. However, the system frequency will be imposed by the grid when the converter is grid connected. In this chapter, the frequency droop controller depicted in Fig. 5.6 is used to build the link between the active power droop control loop and q-axis direct voltage control loop as it can express the relationship between the frequency and q-axis voltage, while the d-axis voltage order V_{cd}^{+*} is produced by the reactive power droop control loop directly. Considering the characteristics of the frequency droop control discussed in Chapter 4, the q-axis positive-sequence voltage order V_{cq}^{+*} can be given by:

$$V_{cq}^{+*} = k_f \left(f^* - f \right) \tag{5.8}$$

5.3 Enhanced AC fault current limit control

As discussed in Chapter 3 and Chapter 4, the absence of vector current control loop during normal operation means that the converter needs to have additional controller to ensure the capability of fault ride-through. Therefore, it is essential to develop an effective AC fault current limit control for the GFM VSC. To ensure a stable operation on weak networks, the current control loop should only work during fault conditions. A voltage balancing controller is developed for overall fault current limiting, and meantime, to retain the direct voltage controller. In addition, an enhanced dq current distribution is employed to share the active and reactive current accordingly. To control the negative-sequence fault currents, a negative-sequence current controller is also designed.

5.3.1 Voltage balancing control

In Chapter 4, the overcurrent limit controller is switched in instead of the reactive power droop controller to limit the overall fault current once the voltage dip is greater than 0.1 pu. However, the overall voltage dip can be smaller than 0.1 pu during asymmetrical faults, during which the overcurrent limit controller will not be switched in. This is not desirable for the converter as potential overcurrent may still occur. To address this issue, the voltage balancing control is developed without control loop switching in this chapter. The control method used in the voltage balancing control loop is similar to the transient fault current limit controller discussed in Chapter 4.

As the overall fault current limiting has to consider both symmetrical and asymmetrical AC faults, the current variables in this subsection are all derived from the abc-dq transformation directly without notch filters. As shown in Fig. 5.7, the upper limit of the saturation block is set to $1.2|I_0|$, where $|I_0|$ refers to the current rating of the converter, while considering 20% overloading capability. On normal operation, the voltage balancing controller produces no response as the current is less than $1.2|I_0|$. When an external AC fault occurs, the feedback signal will be saturated and fixed at the level of

$1.2|I_0|$, which will produce a correction voltage V_{corrd} through a proportional gain (droop) k_b to reduce the voltage order for fault current limiting. The mathematical expression of the voltage balancing controller can be expressed as:

$$V_{corrd} = \begin{cases} 0, & |I_l| < 1.2|I_l^0| \\ k_b\left(1.2|I_l^0| - |I_l|\right), & |I_l| \geq 1.2|I_l^0| \end{cases} \tag{5.9}$$

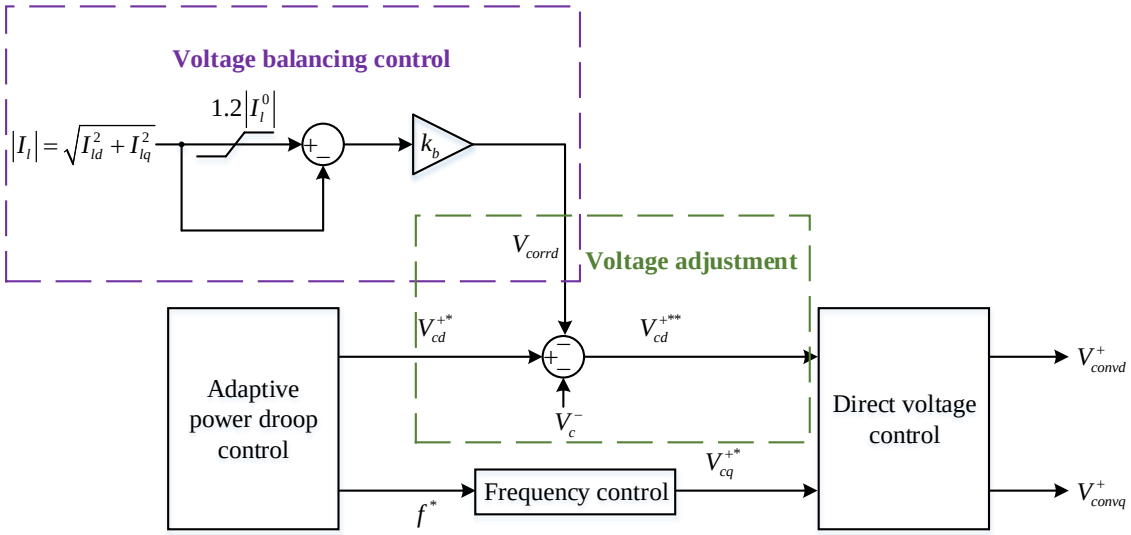

Fig. 5.7 Diagram of voltage balancing control

During asymmetrical AC faults, both positive- and negative-sequence voltages exist, which could potentially result in overvoltage on the healthy phases [158]. As the converter output voltage fed into PWM is the sum of the positive- and negative-sequence components produced by the direct voltage and negative-sequence current controllers (to be introduced later in this chapter), the generated voltage control output could exceed the converter voltage capability during asymmetrical AC faults while trying to control the positive-sequence voltage at the converter filter bus at the nominal value [105]. This can lead to over-modulation of the PWM block that degrades the controllability of the control system [158]. To avoid the aforementioned overvoltage and over-modulation issues, the d-axis voltage order at the converter filter bus is adjusted considering both positive- and negative-sequence components as shown in Fig. 5.7, which can be expressed as:

$$V_{cd}^{+**} = V_{cd}^{+*} - V_{corrd} - V_{c}^{-} \tag{5.10}$$

where V_c^- refers to the converter filter bus voltage in the negative-sequence component, and V_{cd}^{+**} represents the adjusted d-axis voltage order. By applying (5.10), the d-axis voltage order is reduced considering the presence of negative-sequence voltage, to avoid potential overvoltage issue during asymmetrical faults.

5.3.2 Enhanced dq current distribution control

As no negative-sequence components exist during symmetrical AC fault, the current variables in this subsection are also all derived from the abc-dq transformation without notch filters.

On grid connected operation, the VSC is required to distribute the active and reactive current as required in grid code during an external AC fault. As explained in Chapter 4, the so-called "cross-coupling" control can be used to regulate the active and reactive current on the direct voltage control loop. On normal operation, the discussed dq current distribution controller in Chapter 4 still produces unnecessary responses for the converter due to the mismatch between the current orders and measured current as the reactive current order I_{lq}^{*} is always dependent on the voltage error ΔV_{cd} according to (4.11). This will not be a problem if the network is strong due to the compensation of the direct voltage controller. However, system stability may be affected when the grid becomes weak, as the external voltage is likely to see high variation which can lead the dq current distribution controller to adversely affect the operation of the direct voltage controller, which will be validated by simulation results in the later section. In addition, the interference existing in voltage and current between the d- and q-axis can lead to an unsatisfactory dynamic performance on a weak network [154]. To cope with this interference, an enhanced dq current distribution control is proposed.

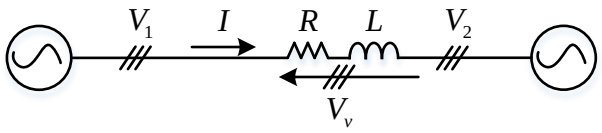

Fig. 5.8 Circuit of a voltage source passing a RL impedance

For the simple circuit shown in Fig. 5.8, the voltage drop between the voltage source and the terminal can be expressed as [80]:

$$\begin{bmatrix} V_{vd} \\ V_{vq} \end{bmatrix} = \begin{bmatrix} V_{1d} \\ V_{1q} \end{bmatrix} - \begin{bmatrix} V_{2d} \\ V_{2q} \end{bmatrix} = \begin{bmatrix} R & -\omega L \\ \omega L & R \end{bmatrix} \begin{bmatrix} I_d \\ I_q \end{bmatrix} \tag{5.11}$$

where V_{1dq} , I_{dq} , V_{2dq} and V_{vdq} represent the source voltage, output current, terminal voltage and voltage drop across the RL in the dq reference frame, respectively.

By linearising (5.11), the expression of the voltage drop deviation can be obtained as:

$$\begin{bmatrix} \Delta V_{vd} \\ \Delta V_{vq} \end{bmatrix} = \begin{bmatrix} R & -\omega L \\ \omega L & R \end{bmatrix} \begin{bmatrix} \Delta I_d \\ \Delta I_q \end{bmatrix} \tag{5.12}$$

where ΔV_{vdq} and ΔI_{dq} refer to the deviation of voltage drop and current flow in the dq reference frame, respectively. According to (5.12), the transient voltage drop can be controlled by regulating the current flowing through a virtual RL impedance. Thus, the control dynamics of the enhanced dq current distribution controller in the dq reference frame for the VSC shown in Fig. 5.1 can be expressed as:

$$\begin{cases} -V_d = k_1 \left(I_{ld}^* - I_{ld} \right) - k_2 \left(I_{lq}^* - I_{lq} \right) \\ V_q = k_1 \left(I_{ld}^* - I_{ld} \right) + k_2 \left(I_{lq}^* - I_{lq} \right) \end{cases} \tag{5.13}$$

where V_d and V_q represent the compensating voltage in the dq reference frame, which will be fed to V_{convd}^+ and V_{convq}^+, respectively. k_1 and k_2 refer to the proportional gains of the enhanced dq current distribution controller, which are equivalent to the virtual impedance ωL and R illustrated in (5.12). The control diagram of the enhanced dq current distribution controller is displayed in Fig. 5.9. The current orders I_{ld}^* and I_{lq}^* in (5.13) are given by:

$$
I_{lq}^{*}=\begin{cases} I_{lq}, & \left(V_{cd}^{0}-V_{cd}^{+}\right)<0.1\text{pu} \\ k_{vi}\left(V_{cd}^{0}-V_{cd}^{+}-V_{c}^{-}\right), & \left(V_{cd}^{0}-V_{cd}^{+}\right)\geq 0.1\text{pu} \end{cases}
$$

$$
I_{ld}^{*}=\begin{cases} \sqrt{\left|I_{l}\right|^{2}-I_{lq}^{*2}}, & \left|I_{l}\right|<1.2\text{pu} \\ \sqrt{\left(1.2\left|I_{l}\right|-\sqrt{I_{ld}^{-2}+I_{lq}^{-2}}\right)^{2}-I_{lq}^{*2}}, & \left|I_{l}\right|\geq 1.2\text{pu} \end{cases} \tag{5.14}
$$

where k_{vi} is the proportional gain for the reactive current order.

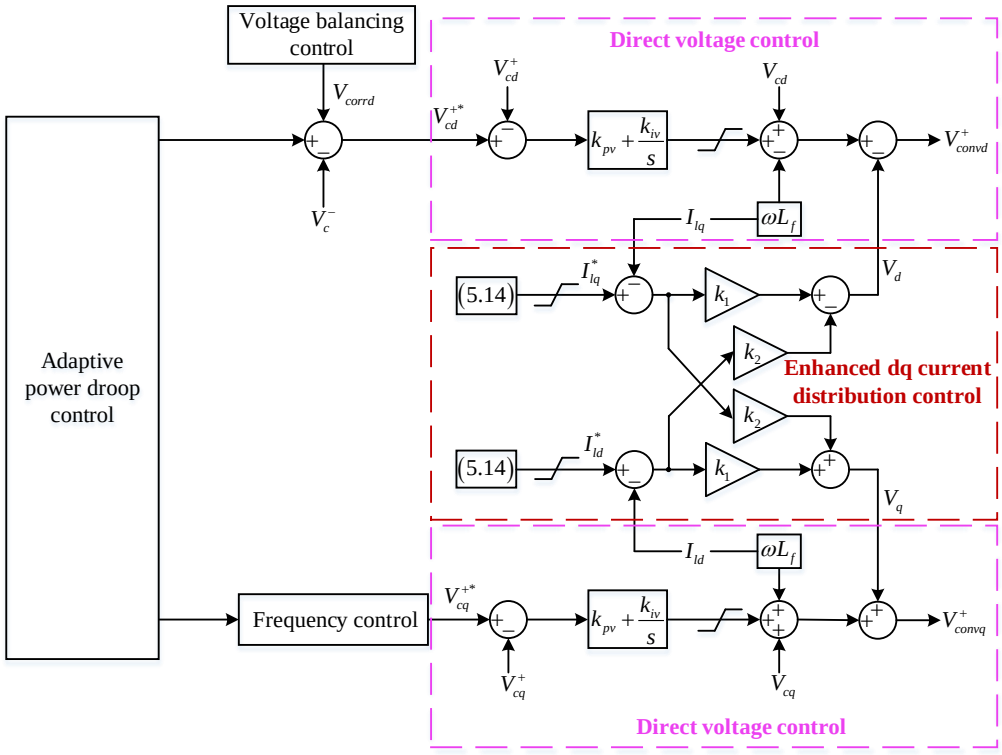

Fig. 5.9 Diagram of the enhanced dq current distribution control

On normal operation, the difference between the nominal voltage magnitude V_{cd}^{0} of the network and the measured positive-sequence d-axis voltage V_{cd}^{+} is negligible (much smaller than 0.1 pu), which makes the current orders I_{ld}^{*} and I_{lq}^{*} equivalent to the measured current I_{ld} and I_{lq}, respectively. This means that the enhanced dq current distribution controller produces no response and has no impact on the system dynamics. The fault current limiting will be accommodated by the voltage balancing controller if there is a fault with a small voltage dip (less than 0.1 pu). In the event of a severe external

AC fault with a significant voltage dip (larger than 0.1 pu), the converter output current will be greater than 1.2 pu, which will lead to new current orders I_{ld}^{*} and I_{lq}^{*} produced according to (5.14), while the actual current I_{ld} and I_{lq} will track the relevant orders through the enhanced dq current distribution controller. As I_{ld} and I_{lq} are not processed by the notch filter, negative-sequence components will exist in I_{ld} and I_{lq} during asymmetrical faults. This means that the enhanced dq current distribution controller will also have impact on the negative-sequence components.

Different from the dq current distribution controller described in Chapter 4, the enhanced dq current distribution controller completely stops working on normal operation to avoid unstable issues, and automatically changes the current orders to trigger the operation during faults. Compared to the method of switching to a separated current control loop, the enhanced dq current distribution controller produces additional voltage components in the d- and q-axis to retain the AC voltage controller, rather than a simple control mode switching which may cause system instability, especially during the mode switching transients. Furthermore, it eliminates the interference existing in current between the d- and q-axis to ensure a stable operation during faults.

5.3.3 Negative-sequence current control

When the system suffers from an asymmetrical AC fault, the measured currents I_{ld} and I_{lq} will contain negative-sequence current components which appear as second-order (double-frequency) harmonics on the positive-sequence reference frame. As the existing dq current distribution controller does not specifically target the negative-sequence current, the negative-sequence fault current cannot be precisely controlled. To ensure the adequate control of the negative-sequence current, a separate negative-sequence current controller is designed as displayed in Fig. 5.10.

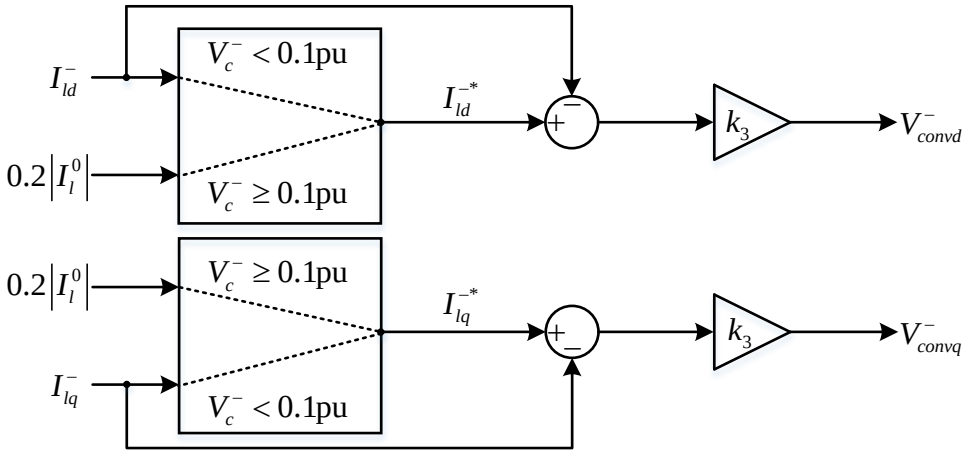

Fig. 5.10 Diagram of the negative-sequence current control

As depicted in Fig. 5.10, the overall control strategy of the negative-sequence current controller employs a proportional gain to ensure the negative-sequence dq-axes current (I_d^- and I_q^-) to track the pre-set values in the event of an asymmetrical AC fault. Hence, the principle of the negative-sequence current control can be expressed as:

$$\begin{cases} V_{convd}^{-} = k_3\left(I_{ld}^{-*} - I_{ld}^{-}\right) + \omega L_f I_{lq}^{-} + V_{cd}^{-} \\ V_{convq}^{-} = k_3\left(I_{lq}^{-*} - I_{lq}^{-}\right) - \omega L_f I_{ld}^{-} + V_{cq}^{-} \end{cases} \tag{5.15}$$

where V_{cdq}^{-}, I_{ldq}^{-*} and I_{ldq}^{-} represent the negative-sequence measured converter filter bus voltage, reference and measured converter output currents, respectively. k_3 is the proportional gain for the negative-sequence current controller. V_{convd}^{-} and V_{convq}^{-} refer to the measured negative sequence converter output voltage, which will be combined with V_{convd}^{+} and V_{convq}^{+} to form the reference voltage for the PWM modulator as displayed in Fig. 5.1. It should be noted that adding separated negative-sequence decoupling terms $\omega L_f I_{ldq}^{-}$ and feedforward terms V_{cdq}^{-} can potentially affect the stability of the converter due to the adverse effects brought by the notch filters [159], [160]. As V_{convdq}^{+} and V_{convdq}^{-} are added to form the overall output voltage, the decoupling terms $\omega L_f I_{ldq}^{-}$ and feedforward terms V_{cdq}^{-} can be included in the existing direct voltage control loop. As displayed in Fig. 5.3,

the decoupling $\omega L_f I_{ldq}$ and feedforward terms V_{cdq} on the direct voltage control covers both positive- and negative-sequence components. Thus, there is no need to add separated negative-sequence compensation here, and the negative-sequence current controller can be simply expressed as:

$$\begin{cases} V_{convd}^{-} = k_3\left(I_{ld}^{-*} - I_{ld}^{-}\right) \\ V_{convq}^{-} = k_3\left(I_{lq}^{-*} - I_{lq}^{-}\right) \end{cases} \tag{5.16}$$

As aforementioned, the enhanced dq current distribution controller impacts on the negative-sequence current, and thus, the proportional gain k_3 used in the negative-sequence current controller needs to be larger than the proportional gains k_1 and k_2 used in the enhanced dq current distribution controller, to ensure the negative-sequence dq-axes current to follow the pre-set current orders effectively.

As negative-sequence current may be needed for fault detection, the profile of the negative-sequence current orders I_{ld}^{-*} and I_{lq}^{-*} can be given by:

$$\begin{aligned} I_{ld}^{-*} &= \begin{cases} I_{ld}^{-}, & V_c^{-} < 0.1\text{pu} \\ 0.2\left|I_l^0\right|, & V_c^{-} \geq 0.1\text{pu} \end{cases} \\ I_{lq}^{-*} &= \begin{cases} I_{lq}^{-}, & V_c^{-} < 0.1\text{pu} \\ 0.2\left|I_l^0\right|, & V_c^{-} \geq 0.1\text{pu} \end{cases} \end{aligned} \tag{5.17}$$

During normal network conditions, negative-sequence voltage will be very small, i.e., V_c^{-} is less than 0.1 pu. Thus, the negative-sequence current orders I_{ld}^{-*} and I_{lq}^{-*} are equivalent to the measured negative-sequence current I_d^{-} and I_q^{-}. This means that the negative-sequence current controller will be deactivated and have no impact on the system dynamics. However, during an asymmetrical AC fault, V_c^{-} will be greater than 0.1 pu, which will cause the negative-sequence current orders I_{ld}^{-*} and I_{lq}^{-*} to be transferred to $0.2\left|I_l^0\right|$ in this example. The current orders can be set at any desired level according to the different requirements of fault detection, and the need of the connected

power network. Then the negative-sequence current controller will regulate the negative sequence current to track the new current order of $0.2\left|I_l^0\right|$.

5.4 Simulation results

To verify the feasibility of the proposed control strategy, the overall system shown in Fig. 5.1 is implemented for time-domain simulations in MATLAB/Simulink. The GFM VSC is connected to a weak network with an SCR of 2 (based on 100 MW), and is subjected to temporary symmetrical and asymmetrical AC faults F as shown in Fig. 5.11. A timed fault logic component is used to automatically apply the faults with a fault resistance of 0.4 Ω. The DC side of the GFM VSC is connected to a constant DC source with a DC voltage of V_{dc}. A detailed switching model in MATLAB/Simulink is used. The system and control parameters are depicted in Table 5.1.

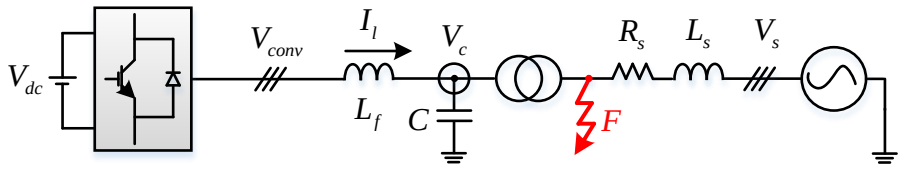

Fig. 5.11 System configuration of the GFM VSC with an external AC fault

5.4.1 Symmetrical AC fault (three-phase-to-ground fault)

To validate the ability of symmetrical fault ride-through of the proposed controller, a three-phase-to-ground fault is applied at the location of F at 1.5 s and is cleared at 1.8 s. Prior to the fault, the converter exports 100 MW (1 pu) active power to the AC system while the reactive power is around 0 MVar. The simulation results are illustrated in Fig. 5.12.

Table 5.1 System and control parameters

System parameters		
Nominal AC voltage (L-L RMS)	110 kV	
Nominal frequency ω_0 (f^0)	100π rad/s (50 Hz)	
Based Power	100 MW	
AC network SCR	2	
Converter DC voltage V_{dc}	100 kV	
Converter power rating	100 MW	
Converter reactance L_f	0.2 pu	
Filter capacitance C	0.15 pu	
Transformer (Y/Y), inductance L_{tm}	55/110 kV, 0.05 pu	
Control parameters of the GFM VSC (pu)		
PLL	Proportional gain k_{ppll}	2.032
	Integral gain k_{ipll}	314.159
Power droop control	Active Power reference P^*	1
	Reactive power reference Q^*	0
	Active power droop coefficient k_p	0.02
	Reactive power droop coefficient k_q	0.01
Frequency droop control	Droop coefficient k_f	0.902
Direct voltage control	Proportional gain k_{pv}	0.9
	Integral gain k_{iv}	40
Voltage balancing control	Proportional gain k_b	8.265
Enhanced dq current distribution control	Reactive current order gain k_{vi}	-1.4
	Proportional gain k_1	0.3
	Proportional gain k_2	0.3
Negative-sequence current control	Proportional gain k_3	0.8

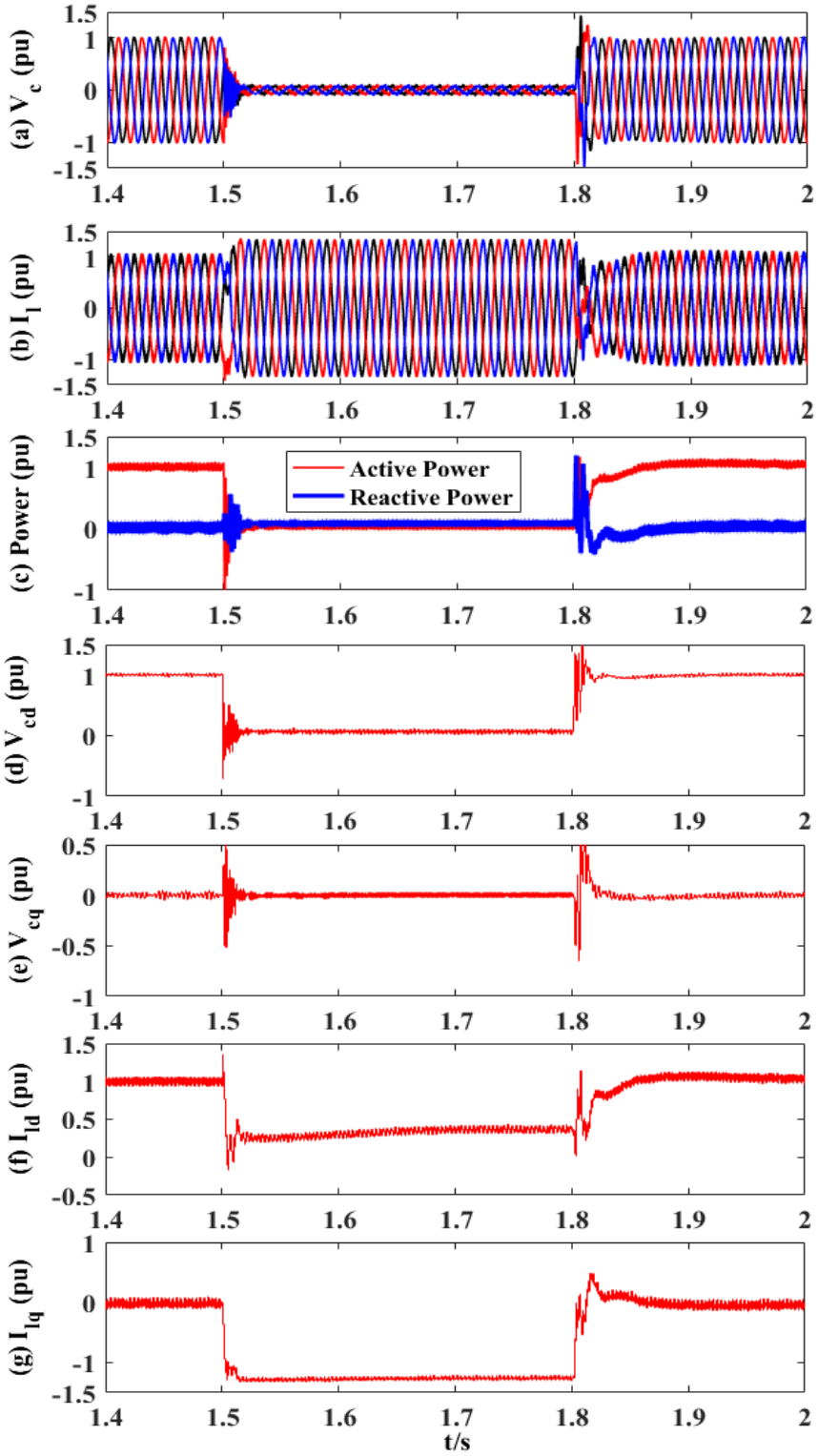

Fig. 5.12 Waveforms of three-phase-to-ground fault: (a) Converter filter bus voltage (b) Converter output current (c) Delivered power (d) d-axis converter filter bus voltage (e) q-axis converter filter bus voltage (f) d-axis converter output current (g) q-axis converter output current

As shown in Fig. 5.12 (a) and (b), the converter filter bus voltage collapses to almost zero during the fault, while the fault current is largely limited to 1.3 pu through the voltage balancing controller. The overall fault current level is a bit higher than the pre-set level 1.2 pu, which is caused by only using a proportional gain/droop in the voltage balancing controller. As the fault is very severe and the converter filter bus voltage collapses during the fault, there is no power exported from the system. Hence, both active and reactive power drop to 0, which can be seen in Fig. 5.12 (c). After the fault initiation, the active power droop controller sets the active power order according to the voltage level as given in (5.6). The positive-sequence d-axis voltage V_{cd}^{+} drops to around 0 during to the fault, which causes the active power order to be 0. Thus, the positive-sequence q-axis voltage V_{cq}^{+} can remain at 0 due to the effective operation of the active power droop controller and the PLL. According to (5.13) and (5.14), the enhanced dq current controller makes the reactive current I_{lq} quickly go to around -1.25 pu whereas the active current I_{ld} is finally limited at 0.25 pu to avoid the overcurrent damage of the converter, as depicted in Fig. 5.12 (f) and (g). After the clearance of the fault, the converter filter bus voltage, output current and delivered active power recover go back quickly to 1 pu after a short period.

Fig. 5.13 presents the waveforms during a three-phase-to-ground fault using the dq current distribution controller introduced in Chapter 4. It can be seen that both the converter filter bus voltage and output current are distorted (unstable) on normal operation, as shown in Fig. 5.13 (a) and (b), which is caused by control conflict between the dq current distribution controller and the direct voltage controller. The undesirable operation of the dq current distribution controller adversely interferes with the performance of the direct voltage controller. This can be avoided by the proposed enhanced dq current distribution controller that equalises the current orders and measured currents, as shown in Fig. 5.12. As shown in Fig. 5.13 (c)-(g), the voltage and current experience severe oscillations during the fault, which are damped with the proposed enhanced dq current distribution controller to mitigate the interference existing in voltage and current between the d- and q-axis.

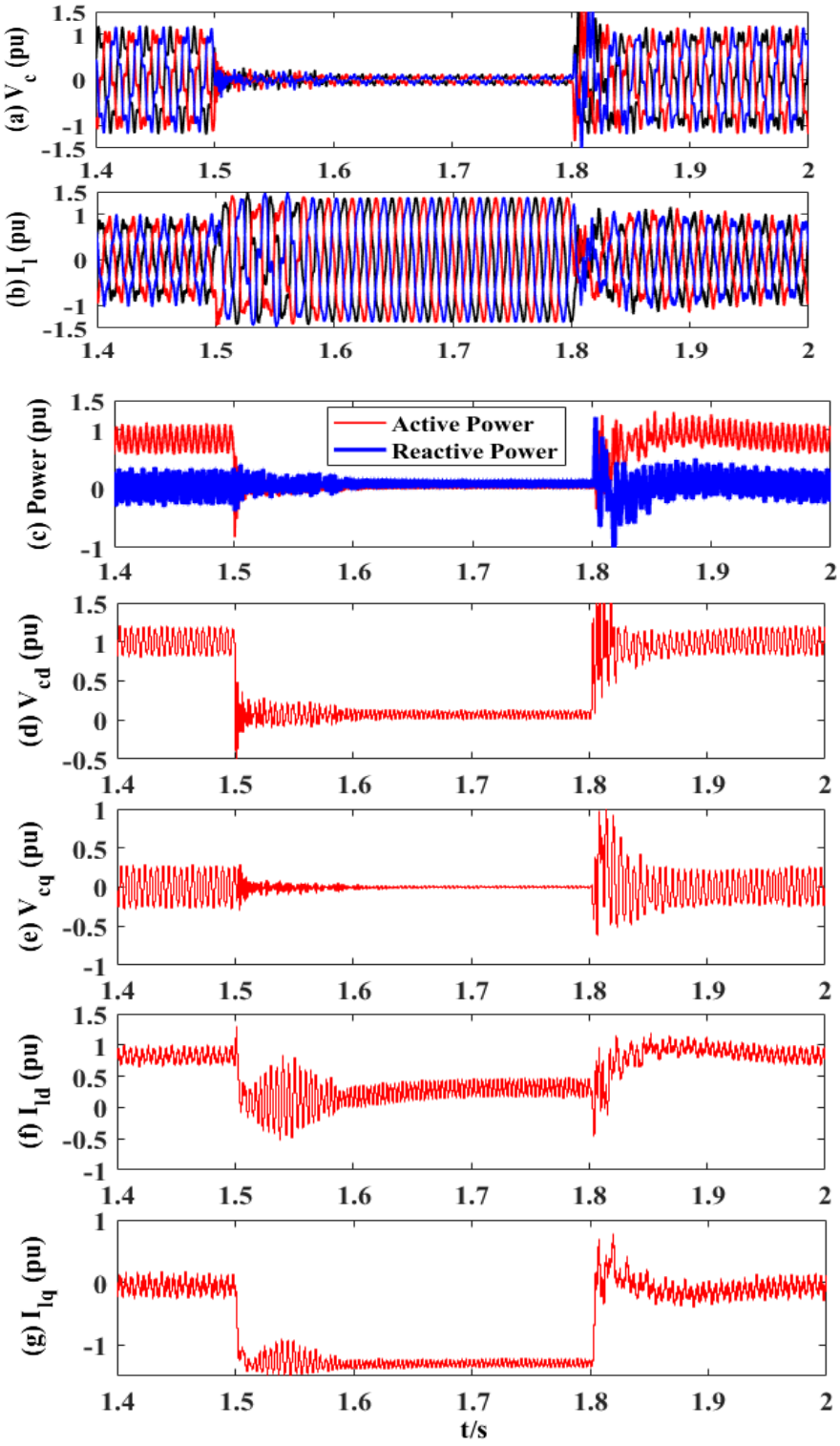

Fig. 5.13 Waveforms of three-phase to ground fault with the dq current distribution controller in Chapter 4 (a) Converter filter bus voltage (b) Converter output current (c) Delivered power (d) d-axis converter filter bus voltage (e) q-axis converter filter bus voltage (f) d-axis converter output current (g) q-axis converter output current

By comparing the simulation results depicted in Fig. 5.12 and Fig. 5.13, it verifies that the enhanced dq current distribution and voltage balancing controller can adequately limit the fault current and distribute the active and reactive current accordingly.

5.4.2 Asymmetrical AC faults

To test the ability of asymmetrical fault ride-through of the proposed controller, three categories of asymmetrical faults are tested and illustrated including single-phase-to-ground fault, phase-phase-to-ground fault and phase-to-phase fault.

A. Single-phase-to-ground fault

Fig. 5.14 shows the simulation waveforms during a single-phase-to-ground fault at the location of F . In this scenario, phase A is short-circuited to ground from 2 s to 2.3 s. As shown in Fig. 5.14 (a), phase A of the converter filter bus voltage drops significantly due to the fault. In addition, the d-axis voltage order in the positive-sequence dq frame is reduced by the voltage balancing control and voltage adjustment as given in (5.10), which leads V_{cd}^{+} drops to 0.7 pu as depicted in Fig. 5.14 (c). Due to the voltage adjustment, there is no significant overvoltage on the healthy phase of the converter filter bus voltage. As shown in Fig. 5.14 (b), the fault current is largely limited at 1.2 pu with a transient current spike at 1.4 pu. During the fault, V_{cq}^{+} remains at 0 pu by PLL to maintain the frequency at the grid level, as shown in Fig. 5.14 (d). As illustrated in Fig. 5.14 (e) and (f), the dq-axes currents in the positive-sequence components (I_{ld}^{+} and I_{lq}^{+}) are shared at 0.9 pu and -0.2 pu respectively, which is resulted from the effective operation of the enhanced dq current distribution controller as given in (5.14). As shown in Fig. 5.14 (e) and (f), the negative-sequence current controller regulates the negative-sequence currents (I_{ld}^{-} and I_{lq}^{-}) at the pre-set level of 0.2 pu, to actively provide negative-sequence fault currents to the network (e.g., for fault detection). As the negative-sequence voltage is controlled through the negative-sequence current controller, the dq-axes voltages in the negative-sequence components (V_{cd}^{-} and V_{cq}^{-}) go to -0.3 pu and -0.05 pu, respectively.

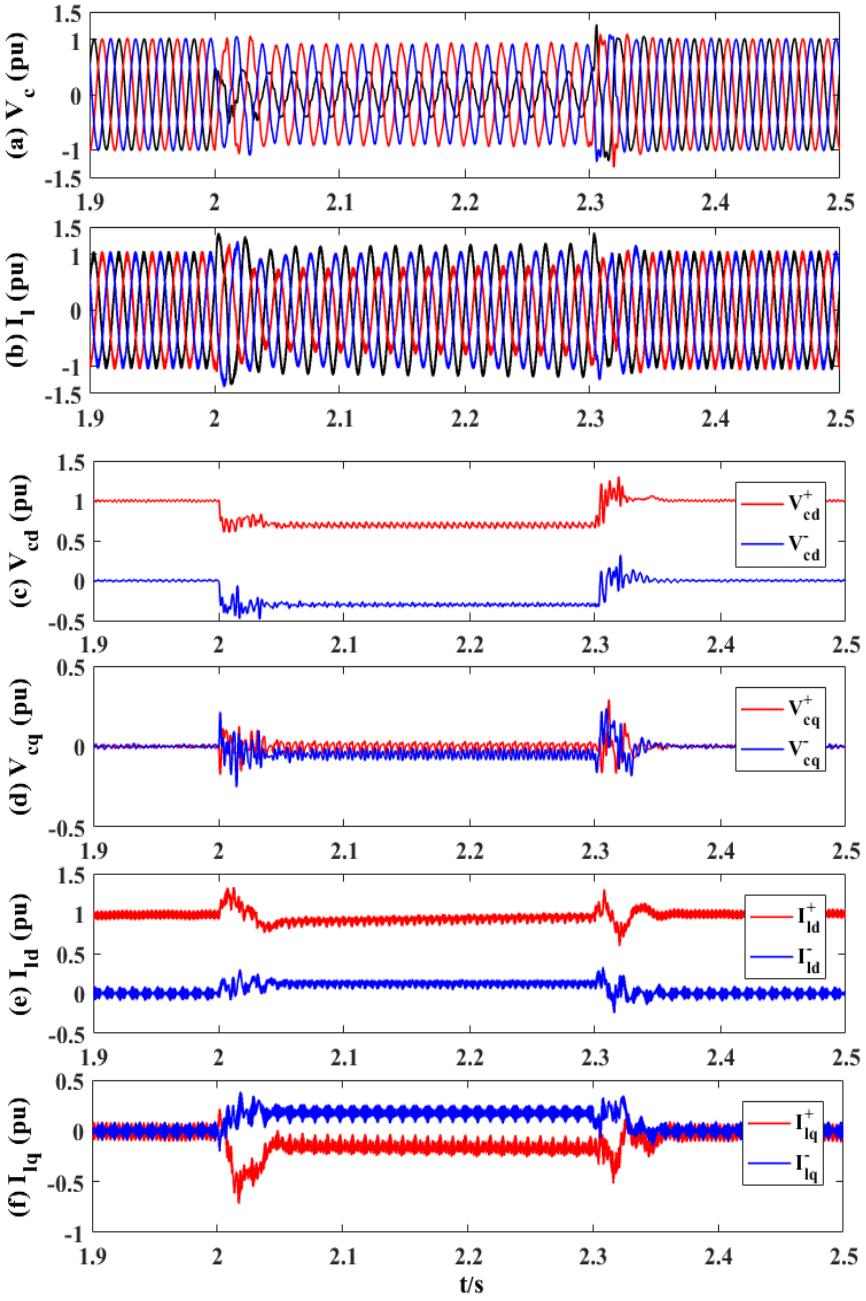

Fig. 5.14 Waveforms of single-phase-to-ground fault (a) Converter filter bus voltage (b) Converter output current (c) d-axis converter filter bus voltage (d) q-axis converter filter bus voltage (e) d-axis converter output current (f) q-axis converter output current

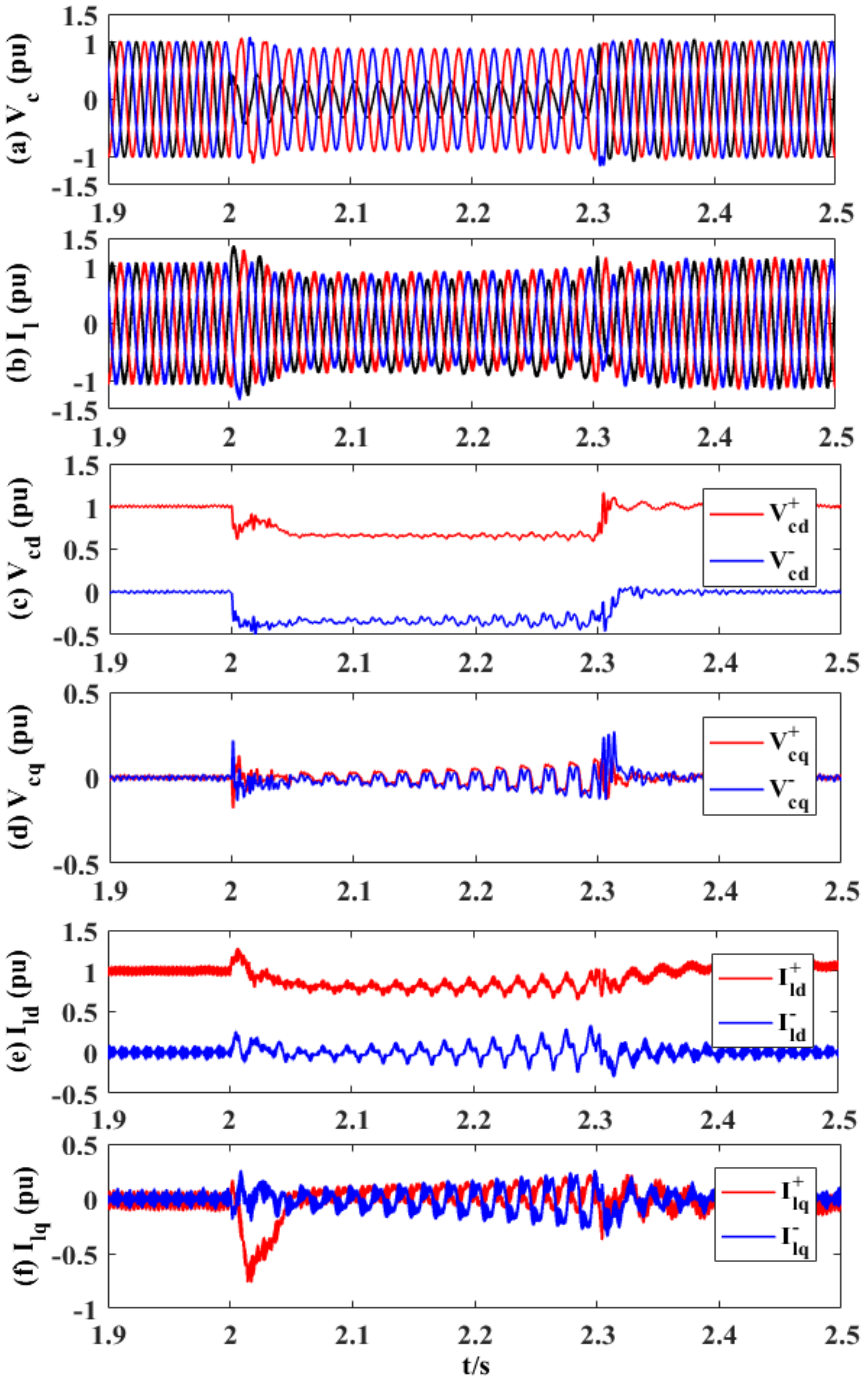

Fig. 5.15 Waveforms of single-phase-to-ground fault without the negative-sequence current controller (a) Converter filter bus voltage (b) Converter output current (c) d-axis converter filter bus voltage (d) q-axis converter filter bus voltage (e) d-axis converter output current (f) q-axis converter output current

To validate the importance and necessity of the employment of the negative-sequence current controller during asymmetrical faults, the converter is tested without the negative-sequence current controller in the event of a single-phase-to-ground fault. The simulation results are displayed in Fig. 5.15. As seen, without the negative-sequence current controller, the negative-sequence currents cannot be controlled, which also causes the divergences of the positive-sequence currents, and the positive- and negative-sequence voltages. The converter tends to become unstable, which indicates the significance of controlling the negative-sequence currents when the system is subject to an asymmetrical AC fault.

B. Phase-phase-to-ground fault

Fig. 5.16 displays the simulation waveforms during phase-phase-to-ground fault at the location of F . In this case, phases A and B of the network are short-circuited to ground at 2.5 s with a fault duration of 0.3 s. As depicted from Fig. 5.16 (a), the healthy phase (phase C) drops to about 0.85 pu whereas phase A and B reduce significantly after the fault initiation. As shown in Fig. 5.16 (c) and (d), the adjusted d-axis order and PLL drive V_{cd}^{+} and V_{cq}^{+} to be 0.5 pu and 0 pu respectively by the direct voltage controller during the fault, while the V_{cd}^{-} and V_{cq}^{-} go to -0.2 pu and 0.35 pu respectively. The peak fault current of the faulted phases is limited at 1.3 pu by the voltage balancing controller, as displayed in Fig. 5.16 (b). Fig. 5.16 (e) and (f) illustrate the simulation waveforms of the positive- and negative-sequence currents. The negative-sequence dq-axes currents are also controlled at the reference level 0.2 pu according to the negative-sequence current controller as given in (5.17). Additionally, the enhanced dq current distribution controller effectively distributes the positive-sequence dq-axes currents at 0.7 pu and -0.9 pu by following the current orders given in (5.14).

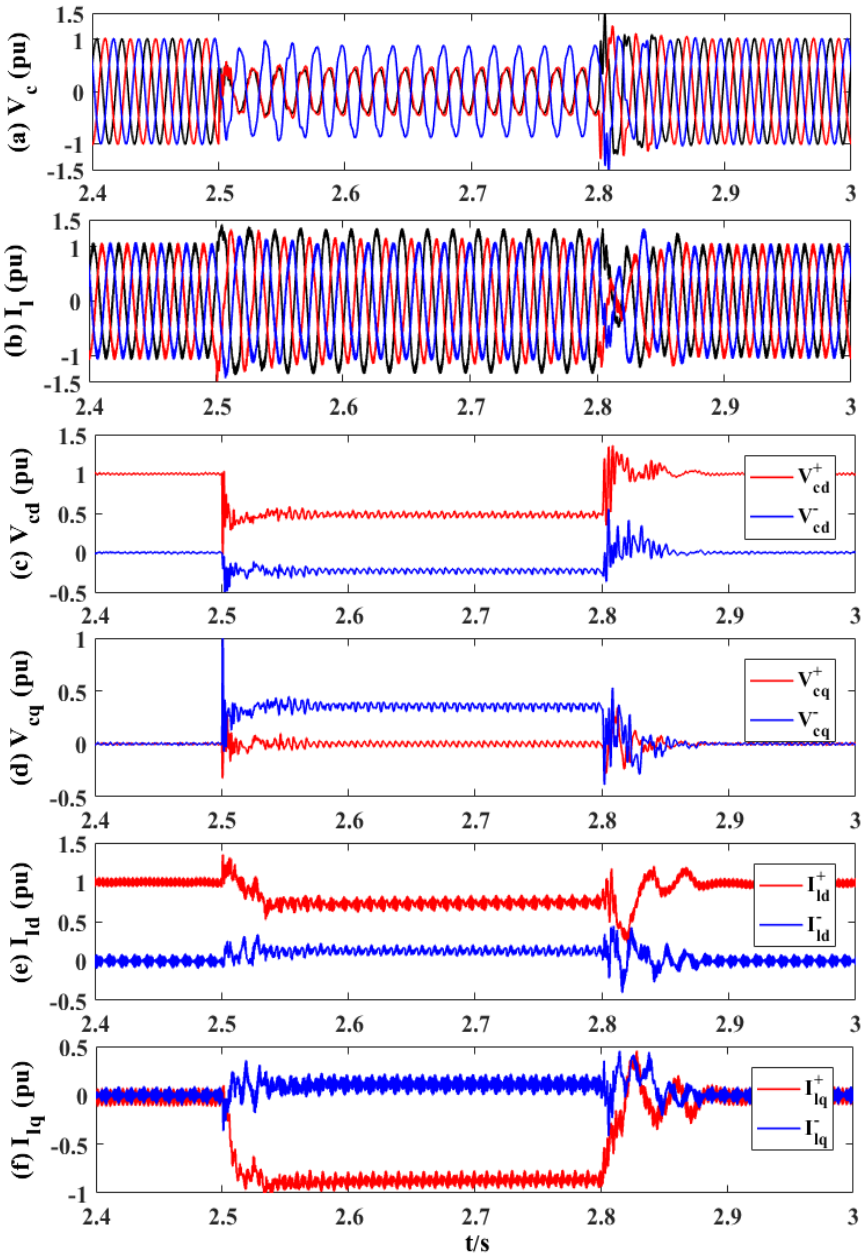

Fig. 5.16 Waveforms of phase-phase to ground fault (a) Converter filter bus voltage (b) Converter output current (c) d-component converter filter bus voltage (d) q-component converter filter bus voltage (e) d-component converter output current (f) q-component converter output current

C. Phase-to-phase fault

In this scenario, phases A and B of the network are short-circuited to each other at the location of F from 3 s to 3.3 s. Fig. 5.17 shows the simulation waveforms during the phase-to-phase fault.

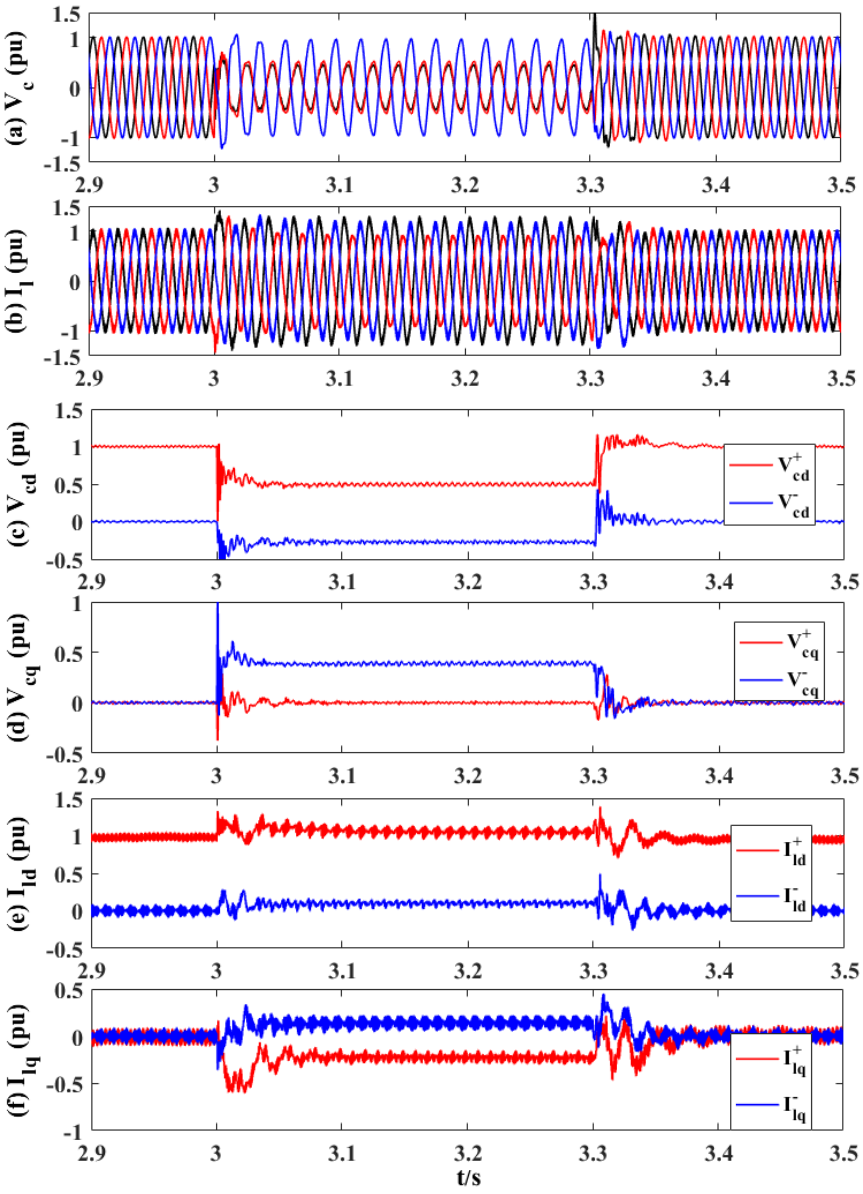

Fig. 5.17 Waveforms of phase to phase fault (a) Converter filter bus voltage (b) Converter output current (c) d-axis converter filter bus voltage (d) q-axis converter filter bus voltage (e) d-axis converter output current (f) q-axis converter output current

As can be seen from Fig. 5.17 (a), the healthy phase (phase C) stays at 1 pu whereas the unhealthy phases (phase A and B) have significant voltage dip due to the fault. The adjusted voltage order as given in (5.10) is followed by the direct voltage controller to control V_{cd}^{+} at 0.5 pu, while PLL effectively forces V_{cq}^{+} at 0 pu, as illustrated in Fig. 5.17 (c) and (d). According to Fig. 5.17 (b), (e) and (f), the overall fault current is largely limited at 1.3 pu by using the voltage balancing controller, while the positive-sequence dq-axes currents (I_{ld}^{+} and I_{lq}^{+}) are distributed at 1.05 pu and -0.25 pu respectively by the enhanced dq current distribution controller. According to (5.14), the reactive current order I_{lq}^{*} depends on the voltage drop corresponding to the nominal positive- and negative-sequence voltages. With the positive- and negative-sequence voltages going to 0.5 pu and 0.45 pu respectively, the reactive current order I_{lq}^{*} becomes small, hence a low positive-sequence reactive current I_{lq}^{+} to prevent over-voltage on the healthy phase. In addition, the negative-sequence dq-axes currents are effectively controlled at 0.2 pu by the negative-sequence current controller. Through regulating the negative-sequence dq-axes currents, the negative-sequence dq-axes voltages go to -0.25 pu and 0.4 pu respectively, as shown in Fig. 5.17 (c) and (d).

The simulation results for all the three categories of asymmetrical AC faults validate that the proposed negative-sequence current controller can effectively control the negative-sequence dq-axes currents during asymmetrical faults, while the overall fault current limiting and sharing of positive-sequence dq-axes currents can be adequately accomplished by the proposed voltage balancing controller with adjusted d-axis voltage order and enhanced dq current distribution controller.

5.5 Summary

In this chapter, the GFM control strategy proposed in Chapter 4 is improved to ensure stable operation when connected to a weak grid and effective AC fault current limit control during both symmetrical and asymmetrical AC faults. Additional voltage balancing, enhanced dq current distribution and negative-sequence current control are proposed. The control system uses double synchronous reference frames to realise the

separated control of positive- and negative-sequence components during asymmetrical faults. To cater for various AC faults, the voltage balancing control loop is adopted instead of the overcurrent limit controller to retain the AC voltage controller for overall fault current limiting. To avoid overvoltage and over-modulations during asymmetrical faults, an adjusted voltage order is used to reduce the d-axis voltage reference. As the dq current distribution controller used in Chapter 4 can affect GFM operation during normal condition when the network becomes weak, it is replaced by the proposed enhanced dq current distribution control loop to ensure the sharing of the active and reactive current during symmetrical AC faults. To precisely control the fault current during asymmetrical faults, a negative-sequence current control strategy is proposed. The viability of the proposed control strategy has been confirmed using the time-domain simulations in MATLAB/Simulink environment.

Chapter 6 Stability analysis of grid-forming and grid-following VSCs integrated to weak networks

In this chapter, the small signal model of the GFM VSC based on the control strategy introduced in Chapter 5 is developed. By applying the impedance-based method introduced in Chapter 2, the admittance of the GFM VSC in the system dq reference frame is derived, and then transformed into the admittance in the positive- and negative-sequence (pn) reference frame by applying the method in [114], [161], [162] to simplify the stability analysis. Based on the converter admittances in the pn reference frame, the stabilities of the GFM VSC and GFL VSC on weak networks are compared according to the Nyquist stability criterion and time-domain simulations. The effectiveness and accuracy of the grid-supporting function for the GFM VSC and GFL VSC are verified by frequency-domain analysis and time-domain simulations in MATLAB/Simulink environment.

6.1 Admittance of the proposed GFM VSC

As presented in Chapter 5, the control system of the GFM includes the adaptive power control, direct voltage control, PLL based frequency droop control and AC fault current limit control. On normal operation, the enhanced AC fault current limit controller produces no response and has no impact on the entire control system. In addition, as the active power order will not hit the upper limit of the dynamic saturation block shown in Fig. 5.4 during a small voltage perturbation, the outer loop can be simplified into a conventional power droop control loop. Thus, the overall system control scheme can be simplified into Fig. 6.1 for the purpose of small signal stability analysis. The voltage variation of the VSC at the DC side is also neglected. In order to conduct the stability analysis and control design in the frequency-domain, nonlinear systems have to be linearised firstly [114], [163], [164]. Based on the linearised system, the small signal model and admittance of the VSC including the controller and impedance of the filter and transformer can be derived. It should be noted that the general GFM schemes in Chapter 4 and Chapter 5 are generally similar except notch filters used in Chapter 5 to extract the

positive- and negative-sequence components. As mentioned in Chapter 5, notch filters can adversely impact the system response, hence the system stability. In this context, the small signal stability of the model for Chapter 5 is only investigated in this chapter.

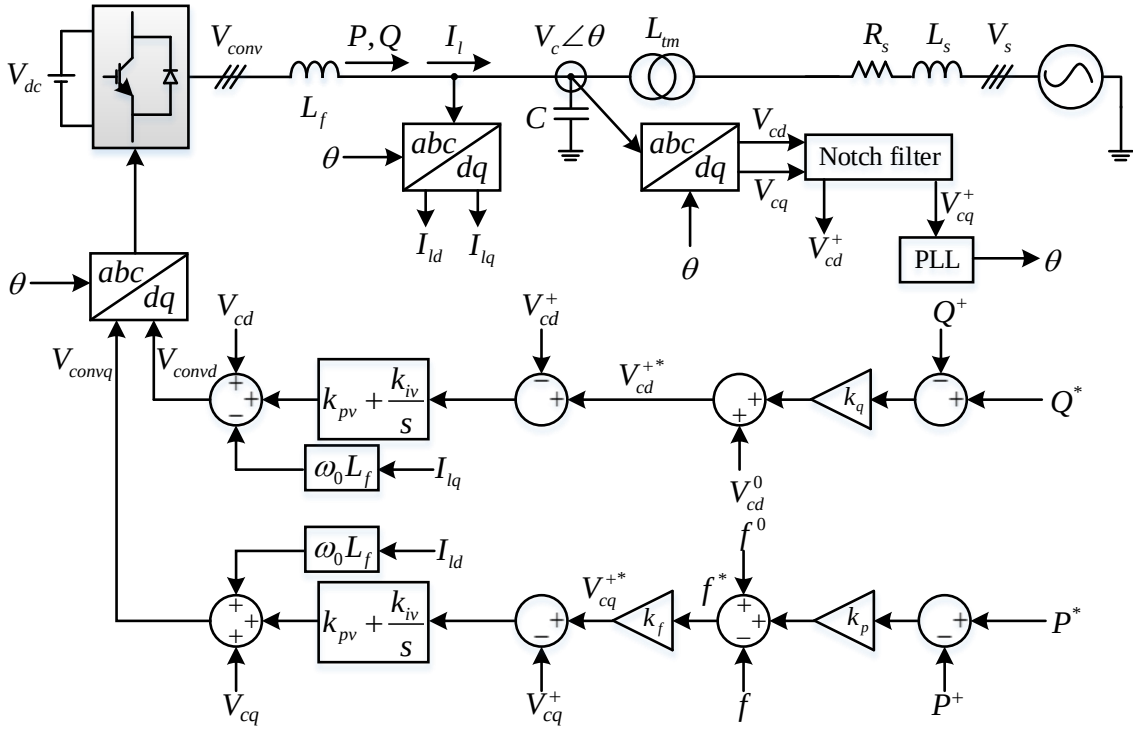

Fig. 6.1 The control configuration of GFM VSC

6.1.1 Admittance in the dq reference frame

As mentioned in Chapter 4 and Chapter 5, PLL is adopted for the proposed GFM VSC to synchronise with the AC grid. Due to the use of PLL, there are two reference frames existing in the system as shown in Fig. 6.2. One is the system dq reference frame (with the superscript "s" displayed in Fig. 6.2), and the other is the controller dq reference frame (without the superscript "s" depicted in Fig. 6.2) [114], [124], [165]. The controller dq reference frame is defined by PLL, which is used for the estimation of the grid parameters to find the position of the system dq reference frame. In this chapter, the variables with the superscript "s" are in the system dq reference frame, while V_{cdq}, I_{ldq} and V_{convdq} are the converter filter bus voltage, converter output current and voltage in the controller dq reference frame.

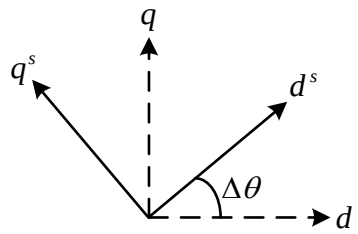

Fig. 6.2 System and controller dq reference frame

In steady-state, the controller dq reference frame is aligned with the system dq reference frame. When a small signal perturbation occurs on the grid voltage, the position of system dq reference frame is changed, which causes the controller dq reference frame to be mis-aligned with the system dq reference frame due to the PLL dynamics [124], [166]. Hence, an angular position error $\Delta\theta$ between the two reference frames appears, as shown in Fig. 6.2. The small signal model of PLL can be depicted in Fig. 6.3.

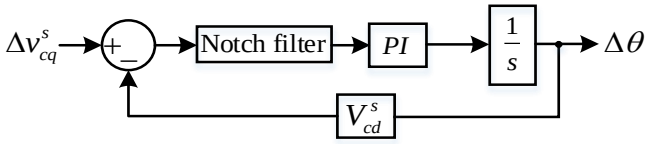

Fig. 6.3 Small signal model of PLL

According to Fig. 6.3, the transfer function of PLL based on small signal model can be expressed as:

$$\Delta\theta = \Delta(\omega t) = \Delta(2\pi ft) = G_{pll}(s)\Delta v_{cq}^s \tag{6.1}$$

where $G_{pll}(s)$ represents the closed loop transfer function of PLL, given by:

$$G_{pll}(s) = \frac{G_{nf}(s)\left(k_{ppll}s + k_{ipll}\right)}{V_{cd}^s s^2 + G_{nf}(s)\left(V_{cd}^s k_{ppll}s + V_{cd}^s k_{ipll}\right)} \tag{6.2}$$

where k_{ppll} and k_{ipll} are the proportional and integral gains of the PLL. $G_{nf}(s)$ represents the transfer function of the notch filter, which was introduced in Chapter 5.

The dynamics of the GFM VSC for the circuit shown in Fig. 6.1 in the system dq reference frame can be expressed as:

$$\begin{bmatrix} V_{convd}^{s} \\ V_{convq}^{s} \end{bmatrix} - \begin{bmatrix} V_{cd}^{s} \\ V_{cq}^{s} \end{bmatrix} = L_f \frac{d}{dt} \begin{bmatrix} I_{ld}^{s} \\ I_{lq}^{s} \end{bmatrix} + \omega_0 L_f \begin{bmatrix} -I_{lq}^{s} \\ I_{ld}^{s} \end{bmatrix} \tag{6.3}$$

where V_{convdq}^{s}, V_{cdq}^{s} and I_{ldq}^{s} represent the converter output voltage, converter filter bus voltage and converter output current in the system dq reference frame.

Based on (6.3), the linearised small signal model of the system depicted in Fig. 6.1 can be derived as:

$$\begin{bmatrix} \Delta v_{convd}^{s} \\ \Delta v_{convq}^{s} \end{bmatrix} - \begin{bmatrix} \Delta v_{cd}^{s} \\ \Delta v_{cq}^{s} \end{bmatrix} = \begin{bmatrix} L_f s & -\omega_0 L_f \\ \omega_0 L_f & L_f s \end{bmatrix} \begin{bmatrix} \Delta i_{ld}^{s} \\ \Delta i_{lq}^{s} \end{bmatrix} \tag{6.4}$$

where Δv_{convdq}^{s}, Δv_{cdq}^{s} and Δi_{ldq}^{s} are the disturbance (small signal) variables of the converter output voltage, converter filter bus voltage, converter output current in the dq reference of the system, respectively.

In steady-state, the converter filter bus voltages V_{cd} and V_{cq} in the controller dq reference frame determined by the PLL equal to the corresponding V_{cd}^{s} and V_{cq}^{s} in the system dq reference frame, which can be given by [124], [161], [167], [168]:

$$\begin{bmatrix} V_{cd} \\ V_{cq} \end{bmatrix} = \begin{bmatrix} \cos(0) & \sin(0) \\ -\sin(0) & \cos(0) \end{bmatrix} \begin{bmatrix} V_{cd}^{s} \\ V_{cq}^{s} \end{bmatrix} \tag{6.5}$$

However, the small voltage perturbations Δv_{cd}^{s} and Δv_{cq}^{s} existed at the converter filter bus will cause PLL to extract an angle deviation $\Delta\theta$ as previously introduced. This will affect the frame transformation for voltage and current. The relationship of the converter filter bus voltages of the two reference frames can be written as:

$$\begin{bmatrix} V_{cd} + \Delta v_{cd} \\ V_{cq} + \Delta v_{cq} \end{bmatrix} = \begin{bmatrix} \cos(0 + \Delta\theta) & \sin(0 + \Delta\theta) \\ -\sin(0 + \Delta\theta) & \cos(0 + \Delta\theta) \end{bmatrix} \begin{bmatrix} V_{cd}^{s} + \Delta v_{cd}^{s} \\ V_{cq}^{s} + \Delta v_{cq}^{s} \end{bmatrix} \tag{6.6}$$

As introduced in Chapter 3, $\sin\Delta\theta \approx \Delta\theta$ and $\cos\Delta\theta \approx 1$ when the angle deviation $\Delta\theta$ is small. By subtracting the steady-state components in (6.5), (6.6) can be rewritten as:

$$\begin{bmatrix}\Delta v_{cd}\\ \Delta v_{cq}\end{bmatrix}=\begin{bmatrix}\Delta v_{cd}^{s}+\Delta\theta V_{cq}^{s}+\Delta\theta\Delta v_{cq}^{s}\\ \Delta v_{cq}^{s}-\Delta\theta V_{cd}^{s}-\Delta\theta\Delta v_{cd}^{s}\end{bmatrix} \tag{6.7}$$

By eliminating the second order terms $\Delta\theta\Delta v_{cq}^{s}$ and $\Delta\theta\Delta v_{cd}^{s}$, (6.7) can be simplified as:

$$\begin{bmatrix}\Delta v_{cd}\\ \Delta v_{cq}\end{bmatrix}=\begin{bmatrix}\Delta v_{cd}^{s}+\Delta\theta V_{cq}^{s}\\ \Delta v_{cq}^{s}-\Delta\theta V_{cd}^{s}\end{bmatrix} \tag{6.8}$$

Regarding (6.1), the voltage perturbations in the controller dq reference frame can be rearranged as:

$$\begin{bmatrix}\Delta v_{cd}\\ \Delta v_{cq}\end{bmatrix}=\begin{bmatrix}1 & V_{cq}^{s}G_{pll}(s)\\ 0 & 1-V_{cd}^{s}G_{pll}(s)\end{bmatrix}\begin{bmatrix}\Delta v_{cd}^{s}\\ \Delta v_{cq}^{s}\end{bmatrix} \tag{6.9}$$

In a similar way, the current perturbations in the controller dq reference frame can be obtained as:

$$\begin{bmatrix}\Delta i_{ld}\\ \Delta i_{lq}\end{bmatrix}=\begin{bmatrix}\Delta i_{ld}^{s}+\Delta\theta I_{lq}^{s}\\ \Delta i_{lq}^{s}+\Delta\theta I_{ld}^{s}\end{bmatrix}=\begin{bmatrix}0 & I_{lq}^{s}G_{pll}(s)\\ 0 & -I_{ld}^{s}G_{pll}(s)\end{bmatrix}\begin{bmatrix}\Delta v_{cd}^{s}\\ \Delta v_{cq}^{s}\end{bmatrix}+\begin{bmatrix}\Delta i_{ld}^{s}\\ \Delta i_{lq}^{s}\end{bmatrix} \tag{6.10}$$

In the same way, the small signal of the converter output voltage references produced by the direct voltage controller in the system dq reference frame can be derived as:

$$\begin{bmatrix}\Delta v_{convd}^{s}\\ \Delta v_{convq}^{s}\end{bmatrix}=\begin{bmatrix}\Delta v_{convd}-\Delta\theta V_{convq}^{s}\\ \Delta v_{convq}+\Delta\theta V_{convd}^{s}\end{bmatrix}=\begin{bmatrix}0 & -V_{convq}^{s}G_{pll}(s)\\ 0 & V_{convd}^{s}G_{pll}(s)\end{bmatrix}\begin{bmatrix}\Delta v_{cd}^{s}\\ \Delta v_{cq}^{s}\end{bmatrix}+\begin{bmatrix}\Delta v_{convd}\\ \Delta v_{convq}\end{bmatrix} \tag{6.11}$$

Defining matrices: $\Delta\boldsymbol{v_c}=\begin{bmatrix}\Delta v_{cd}\\ \Delta v_{cq}\end{bmatrix}$, $\Delta\boldsymbol{v_c^s}=\begin{bmatrix}\Delta v_{cd}^{s}\\ \Delta v_{cq}^{s}\end{bmatrix}$, $\Delta\boldsymbol{i_l}=\begin{bmatrix}\Delta i_{ld}\\ \Delta i_{lq}\end{bmatrix}$, $\Delta\boldsymbol{i_l^s}=\begin{bmatrix}\Delta i_{ld}^{s}\\ \Delta i_{lq}^{s}\end{bmatrix}$,

$\Delta\boldsymbol{v_{conv}}=\begin{bmatrix}\Delta v_{convd}\\ \Delta v_{convq}\end{bmatrix}$, $\Delta\boldsymbol{v_{conv}^s}=\begin{bmatrix}\Delta v_{convd}^{s}\\ \Delta v_{convq}^{s}\end{bmatrix}$, $\mathbf{A}=\begin{bmatrix}1 & V_{cq}^{s}G_{pll}(s)\\ 0 & 1-V_{cd}^{s}G_{pll}(s)\end{bmatrix}$, $\mathbf{B}=\begin{bmatrix}0 & I_{lq}^{s}G_{pll}(s)\\ 0 & -I_{ld}^{s}G_{pll}(s)\end{bmatrix}$,

$\mathbf{E}=\begin{bmatrix}0 & -V^{s}_{convq}G_{pll}(s)\\ 0 & V^{s}_{convd}G_{pll}(s)\end{bmatrix}$ and $\mathbf{Z}=\begin{bmatrix}L_f s & -\omega_0 L_f\\ \omega_0 L_f & L_f s\end{bmatrix}$, (6.4), (6.9), (6.10) and (6.11) can be rewritten as:

$$\Delta \boldsymbol{v}^{s}_{conv}-\Delta \boldsymbol{v}^{s}_{c}=\mathbf{Z}\Delta \boldsymbol{i}^{s}_{l} \tag{6.12}$$

$$\Delta \boldsymbol{v}_{c}=\mathbf{A}\Delta \boldsymbol{v}^{s}_{c} \tag{6.13}$$

$$\Delta \boldsymbol{i}_{l}=\mathbf{B}\Delta \boldsymbol{v}^{s}_{c}+\Delta \boldsymbol{i}^{s}_{l} \tag{6.14}$$

$$\Delta \boldsymbol{v}_{conv}=-\mathbf{E}\Delta \boldsymbol{v}^{s}_{c}+\Delta \boldsymbol{v}^{s}_{conv} \tag{6.15}$$

Considering that the GFM VSC is controlled by the direct voltage control loop, the matrices of the PI regulators and decoupling terms in the controller can be defined as:

$$\mathbf{V}=\begin{bmatrix}\left(k_{pv}+k_{iv}\right)/s & 0\\ 0 & \left(k_{pv}+k_{iv}\right)/s\end{bmatrix} \tag{6.16}$$

$$\mathbf{D}=\begin{bmatrix}0 & -\omega_0 L_f\\ \omega_0 L_f & 0\end{bmatrix} \tag{6.17}$$

The relationship between V^{+}_{cdq} and V_{cdq} can be expressed as:

$$\begin{bmatrix}V^{+}_{cd}\\ V^{+}_{cq}\end{bmatrix}=\mathbf{N}\begin{bmatrix}V_{cd}\\ V_{cq}\end{bmatrix} \text{ by defining } \mathbf{N}=\begin{bmatrix}G_{nf}(s) & 0\\ 0 & G_{nf}(s)\end{bmatrix} \tag{6.18}$$

Thus, by linearising (6.18), the small perturbation of the positive-sequence component voltage in the controller dq reference frame can be obtained as:

$$\begin{bmatrix}\Delta v^{+}_{cd}\\ \Delta v^{+}_{cq}\end{bmatrix}=\mathbf{N}\begin{bmatrix}\Delta v_{cd}\\ \Delta v_{cq}\end{bmatrix}=\mathbf{N}\Delta \boldsymbol{v}_{c} \tag{6.19}$$

where Δv^{+}_{cd} and Δv^{+}_{cq} represent the positive-sequence component voltage deviations in the controller dq reference frame at the converter filter bus.

The time delay T_d caused by the adoption of digital control method and PWM is introduced, which can be defined as [114], [118], [120], [165]:

$$\mathbf{F}=\begin{bmatrix}1/\left(1+0.5T_d s\right) & 0\\ 0 & 1/\left(1+0.5T_d s\right)\end{bmatrix} \tag{6.20}$$

where T_d is set at one (for PWM delay) and half (for control loop sampling rate) of the PWM duty circle T_{sw} (i.e. 0.4 ms), hence 0.6 ms in this chapter. It is worth mentioning that the change caused by the digital control method and PWM takes effect right away but occurs over the full time T_d, so $0.5T_d$ is taken here as the average delay.

Hence, by assuming constant voltage orders V_{cd}^{+*} and V_{cq}^{+*}, the small perturbation of the converter output voltage in the dq reference frame of the controller can be obtained as:

$$\Delta \boldsymbol{v}_{\boldsymbol{conv}}=\mathbf{F}\left(-\mathbf{VN}\Delta \boldsymbol{v}_{\boldsymbol{c}}+\mathbf{D}\Delta \boldsymbol{i}_{\boldsymbol{l}}+\Delta \boldsymbol{v}_{\boldsymbol{c}}\right) \tag{6.21}$$

Considering (6.12)-(6.21), the small signal admittance of the GFM VSC with constant voltage orders V_{cd}^{+*} and V_{cq}^{+*} in the system dq reference frame can be derived as:

$$\mathbf{Y}_{\boldsymbol{vsc}}=-\frac{\Delta \boldsymbol{i}_{\boldsymbol{l}}^{\boldsymbol{s}}}{\Delta \boldsymbol{v}_{\boldsymbol{c}}^{\boldsymbol{s}}}=\frac{-\mathbf{FVAN}+\mathbf{FDB}+\mathbf{FA}+\mathbf{E}-\mathbf{I}}{-\mathbf{Z}+\mathbf{FD}} \tag{6.22}$$

where $\mathbf{I}$ is the identity matrix that can be defined as $\begin{bmatrix}1 & 0\\ 0 & 1\end{bmatrix}$. $\mathbf{Y}_{\boldsymbol{vsc}}$ can be represented by four elements ($Y_{vscdd}(s)$, $Y_{vscdq}(s)$, $Y_{vscqd}(s)$ and $Y_{vscqq}(s)$) in a matrix as:

$$\mathbf{Y}_{\boldsymbol{vsc}}=\begin{bmatrix}Y_{vscdd}(s) & Y_{vscdq}(s)\\ Y_{vscqd}(s) & Y_{vscqq}(s)\end{bmatrix} \tag{6.23}$$

As the voltage orders V_{cd}^{+*} and V_{cq}^{+*} shown in Fig. 6.1 are determined by the outer controllers including the frequency droop and power droop controller, the corresponding outer controllers can impact on the voltage orders, and hence the entire control system.

The frequency droop controller as shown in Fig. 6.1 can be linearised as:

$$\Delta v_{cq}^{+*} = k_f \left(\Delta f^* - \Delta f \right) \tag{6.24}$$

In the same way, (6.1) can be linearised as:

$$\Delta f = \frac{s \bullet G_{pll}(s)}{2\pi} \tag{6.25}$$

When the positive-sequence q-axis voltage order V_{cq}^{+*} is given by the frequency droop controller with a constant frequency reference f^*, and the positive-sequence d-axis voltage order V_{cd}^{+*} is fixed, which gives $\Delta f^* = 0$ and $\Delta v_{cd}^{+} = 0$, the small signal perturbations of the voltage orders can be derived as:

$$\begin{bmatrix} \Delta v_{cd}^{+*} \\ \Delta v_{cq}^{+*} \end{bmatrix} = \begin{bmatrix} 1 & 0 \\ 0 & k_f \end{bmatrix} \begin{bmatrix} 0 & 0 \\ 0 & s \bullet G_{pll}(s)/2\pi \end{bmatrix} \begin{bmatrix} \Delta v_{cd}^{s} \\ \Delta v_{cq}^{s} \end{bmatrix} \tag{6.26}$$

As discussed in Chapter 5, the instantaneous power in the positive-sequence component generated from the GFM VSC can be expressed in the controller dq reference frame as:

$$P^+ = 1.5\left(V_{cd}^+ I_{ld}^+ + V_{cq}^+ I_{lq}^+ \right) \tag{6.27}$$

$$Q^+ = 1.5\left(V_{cq}^+ I_{ld}^+ - V_{cd}^+ I_{lq}^+ \right) \tag{6.28}$$

By linearising (6.27) and (6.28), the expression of the active and reactive power deviations (ΔP^+ and ΔQ^+) can be derived as:

$$\begin{bmatrix} -\Delta Q^+ \\ -\Delta P^+ \end{bmatrix} = \begin{bmatrix} 1.5I_{lq}^{+s} & -1.5I_{ld}^{+s} \\ -1.5I_{ld}^{+s} & -1.5I_{lq}^{+s} \end{bmatrix} \begin{bmatrix} \Delta v_{cd}^+ \\ \Delta v_{cq}^+ \end{bmatrix} + \begin{bmatrix} -1.5V_{cq}^{+s} & 1.5V_{cd}^+ \\ -1.5V_{cd}^+ & -1.5V_{cq}^{+s} \end{bmatrix} \begin{bmatrix} \Delta i_{ld}^+ \\ \Delta i_{lq}^+ \end{bmatrix} \tag{6.29}$$

where Δi_{ld}^+ and Δi_{lq}^+ represent the converter output current deviations in the positive-sequence component in the controller dq reference frame. V_{cdq}^{+s} and I_{ldq}^{+s} refer to the steady-state converter filter bus voltage and output current in the positive-sequence component in the system dq reference frame.

The power droop controller shown in Fig. 6.1 can be linearised as:

$$\Delta v_{cd}^{+*} = -k_q\left(-\Delta Q^{+}\right) \tag{6.30}$$

$$\Delta f^{*} = k_p\left(-\Delta P^{+}\right) \tag{6.31}$$

According to (6.25)-(6.31), when the voltage orders are controlled by the power droop and frequency droop controllers, the deviations of the voltage orders Δv_{cd}^{+*} and Δv_{cq}^{+*} can be expressed as:

$$\begin{bmatrix}\Delta v_{cd}^{+*}\\ \Delta v_{cq}^{+*}\end{bmatrix} = \begin{bmatrix}1 & 0\\ 0 & k_f\end{bmatrix}\begin{bmatrix}-k_q & 0\\ 0 & k_p\end{bmatrix}\begin{bmatrix}-\Delta Q^{+}\\ -\Delta P^{+}\end{bmatrix} - \begin{bmatrix}1 & 0\\ 0 & k_f\end{bmatrix}\begin{bmatrix}0 & 0\\ 0 & s\bullet G_{pll}(s)/2\pi\end{bmatrix}\begin{bmatrix}\Delta v_{cd}^{s}\\ \Delta v_{cq}^{s}\end{bmatrix} \tag{6.32}$$

The relationship between Δi_{ldq}^{+} and Δi_{ldq} is similar to (6.18), which can be expressed as:

$$\begin{bmatrix}\Delta i_{ld}^{+}\\ \Delta i_{lq}^{+}\end{bmatrix} = \mathbf{N}\begin{bmatrix}\Delta i_{ld}\\ \Delta i_{lq}\end{bmatrix} = \mathbf{N}\Delta \boldsymbol{i}_{\boldsymbol{l}} \tag{6.33}$$

Defining $\mathbf{K} = \begin{bmatrix}-k_q & 0\\ 0 & k_p\end{bmatrix}$, $\mathbf{V} = \begin{bmatrix}-1.5V_{cq}^{+s} & 1.5V_{cd}^{+}\\ -1.5V_{cd}^{+} & -1.5V_{cq}^{+s}\end{bmatrix}$, $\mathbf{C} = \begin{bmatrix}1.5I_{lq}^{+s} & -1.5I_{ld}^{+s}\\ -1.5I_{ld}^{+s} & -1.5I_{lq}^{+s}\end{bmatrix}$, $\mathbf{P} = \begin{bmatrix}0 & 0\\ 0 & s\bullet G_{pll}(s)/2\pi\end{bmatrix}$ and $\mathbf{G} = \begin{bmatrix}1 & 0\\ 0 & k_f\end{bmatrix}$, the total small signal admittance of the GFM VSC with PLL and the outer controllers can be derived as:

$$\mathbf{Y}_{\boldsymbol{vsc}} = \frac{\mathbf{FVGKVBN} + \mathbf{FVGKCAN} - \mathbf{FVKP} - \mathbf{FVAN} + \mathbf{FDB} + \mathbf{FA} + \mathbf{E} - \mathbf{I}}{-\mathbf{Z} + \mathbf{FD} + \mathbf{FVGKVN}} \tag{6.34}$$

where the calculated admittance $\mathbf{Y}_{\boldsymbol{vsc}}$ of the GFM VSC represents the part within the boxed formed by the red dotted lines, as illustrated in Fig. 6.4.

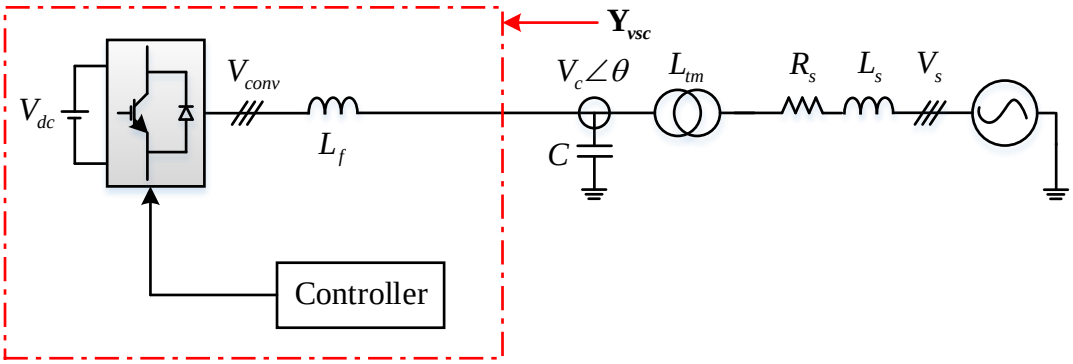

Fig. 6.4 Schematics of the admittance calculated by the small signal model

6.1.2 Admittance in the pn reference frame

As investigated in [169], [170], the dq impedance method is better suited for modelling. Nevertheless, it is complicated for stability analysis as there is frequency transformation in the dq impedance method [114], [118], [124], [165], [171]. Thus, the admittance in the dq reference frame is transformed into the pn reference frame to build a more straightforward model in a common frame [172], which is also easier to combine with the grid impedance [171]. According to [114], [162], [171], [173], the small signal admittance of the GFM VSC depicted in (6.34) can be transformed in the pn reference frame as:

$$Y_{vscpp}(s)=\frac{1}{2}\left(Y_{vscdd}(s-j\omega_0)+Y_{vscqq}(s-j\omega_0)+Y_{vscqd}(s-j\omega_0)-Y_{vscdq}(s-j\omega_0)\right) \quad (6.35)$$

$$Y_{vscpp}(s)=\frac{1}{2}\left(Y_{vscdd}(s+j\omega_0)-Y_{vscqq}(s+j\omega_0)+Y_{vscqd}(s+j\omega_0)+Y_{vscdq}(s+j\omega_0)\right) \quad (6.36)$$

$$Y_{vscpp}(s)=\frac{1}{2}\left(Y_{vscdd}(s-j\omega_0)-Y_{vscqq}(s-j\omega_0)-Y_{vscqd}(s-j\omega_0)-Y_{vscdq}(s-j\omega_0)\right) \quad (6.37)$$

$$Y_{vscpp}(s)=\frac{1}{2}\left(Y_{vscdd}(s+j\omega_0)+Y_{vscqq}(s+j\omega_0)-Y_{vscqd}(s+j\omega_0)+Y_{vscdq}(s+j\omega_0)\right) \quad (6.38)$$

$$\mathbf{Y}_{vscPN}=\begin{bmatrix} Y_{vscpp}(s) & Y_{vscpn}(s) \\ Y_{vscnp}(s-2j\omega_0) & Y_{vscnn}(s-2j\omega_0) \end{bmatrix} \quad (6.39)$$

where $\mathbf{Y}_{vscPN}$ is the small signal admittance of the GFM VSC in the pn reference frame. $Y_{vscpp}(s)$, $Y_{vscpn}(s)$, $Y_{vscnp}(s-2j\omega_0)$ and $Y_{vscnn}(s-2j\omega_0)$ are the four elements of the matrix shown in (6.39).

6.1.3 Validation of analytical admittance for the GFM VSC

To verify the accuracy of the small signal admittance of the GFM VSC calculated by the method discussed previously, a time-domain model using the control system shown in Fig. 6.1 is established in MATLAB/Simulink. The system and control parameters are depicted in Table 6.1. By adopting the admittance measuring method in time-domain introduced in [114], the admittance in time-domain simulation can be extracted. The GFM VSC is set to export 1 pu active power into the AC grid with an SCR of 2. As the impedance of both the capacitor and transformer can also impact on the total admittance of the system, the final admittance in the pn reference frame $\mathbf{Y}_{vscPNT}$ calculated for the small signal model covers the impedance of the capacitor and transformer, which is the part within the boxed formed by the blue dotted line, as depicted in Fig. 6.5.

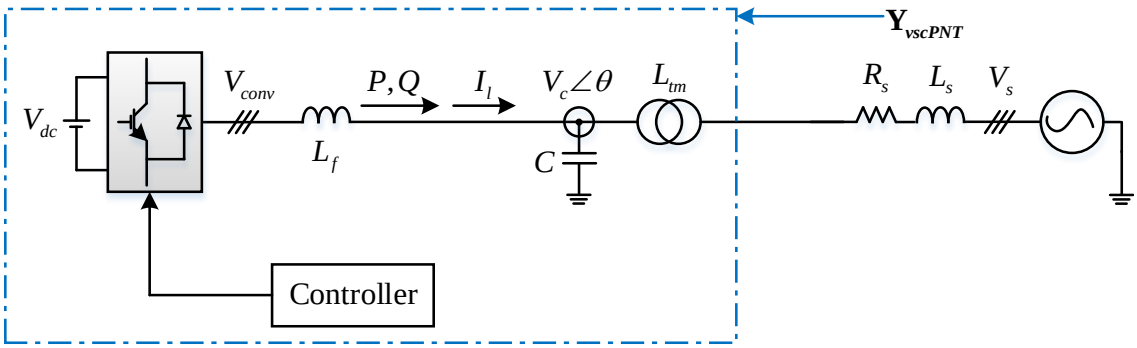

Fig. 6.5 Schematics of the final admittance calculated by the small signal model

Table 6.1 System and control parameters

System parameters		
DC voltage V_{dc}		100 kV
Power rating		500 MW
SCR		2
Nominal frequency ω_0 (f^0)		100 π rad/s (50 Hz)
Converter reactance L_f		0.2 pu
Filter capacitance C		0.15 pu
Transformer (Y/Y), inductance L_{tm}		55/110 kV, 0.05 pu
Control parameters of the GFM VSC (pu)		
PLL	Proportional gain k_{ppll}	1
	Integral gain k_{ipll}	78.54
Power droop control	Active power order P^*	1
	reactive power order Q^*	0
	Active power droop coefficient k_p	0.02
	Reactive power droop coefficient k_q	0.02
Frequency droop control	Droop coefficient k_f	1.65
Direct voltage control	Proportional gain k_{pv}	1.08
	Integral gain k_{iv}	9.6

Fig. 6.6 compares the admittances calculated using the analytical method and those measured from the time-domain simulation model, where the pink line denotes the analytical admittance and the red asterisks represent the measured admittance from the time-domain model. As displayed in Fig. 6.6, the admittances of the two models match each other very well. This indicates that the admittance calculated by the small signal analytical model are accurate and effective.

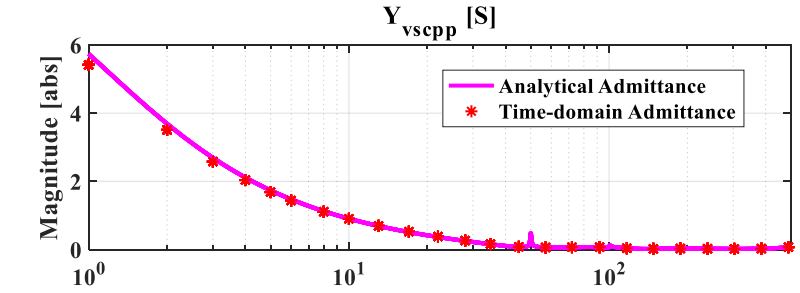
Y_{vscpp} [S]
Magnitude [abs]
Analytical Admittance
Time-domain Admittance

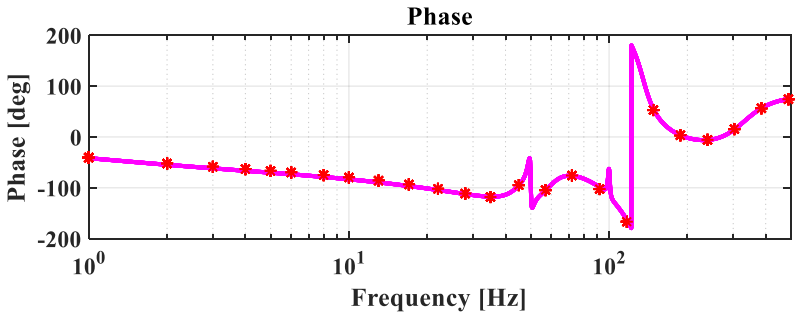
Phase
Phase [deg]
Frequency [Hz]

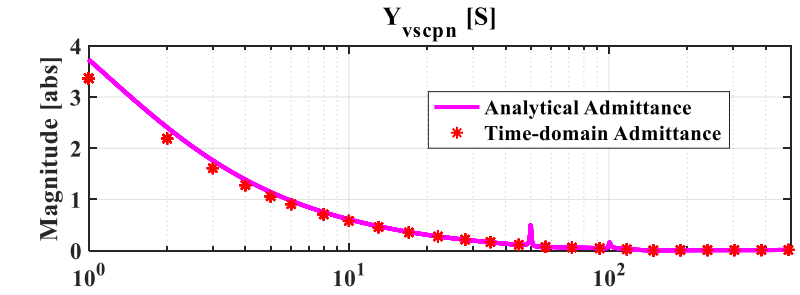
Y_{vscpn} [S]
Magnitude [abs]
Analytical Admittance
Time-domain Admittance

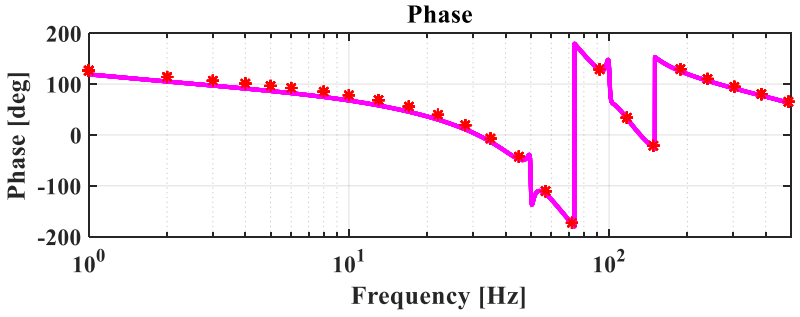
Phase
Phase [deg]
Frequency [Hz]

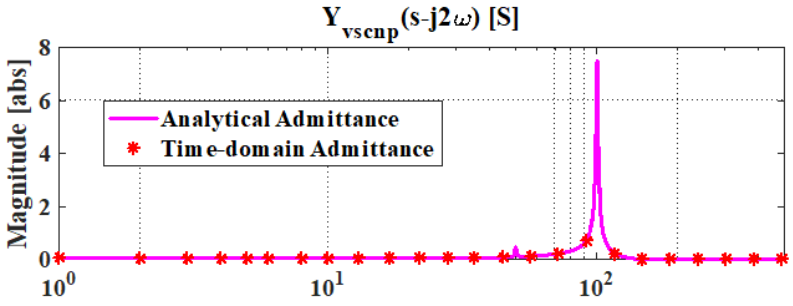
$Y_{vscnp}(s-j2\omega)$ [S]
Magnitude [abs]
Analytical Admittance
Time-domain Admittance

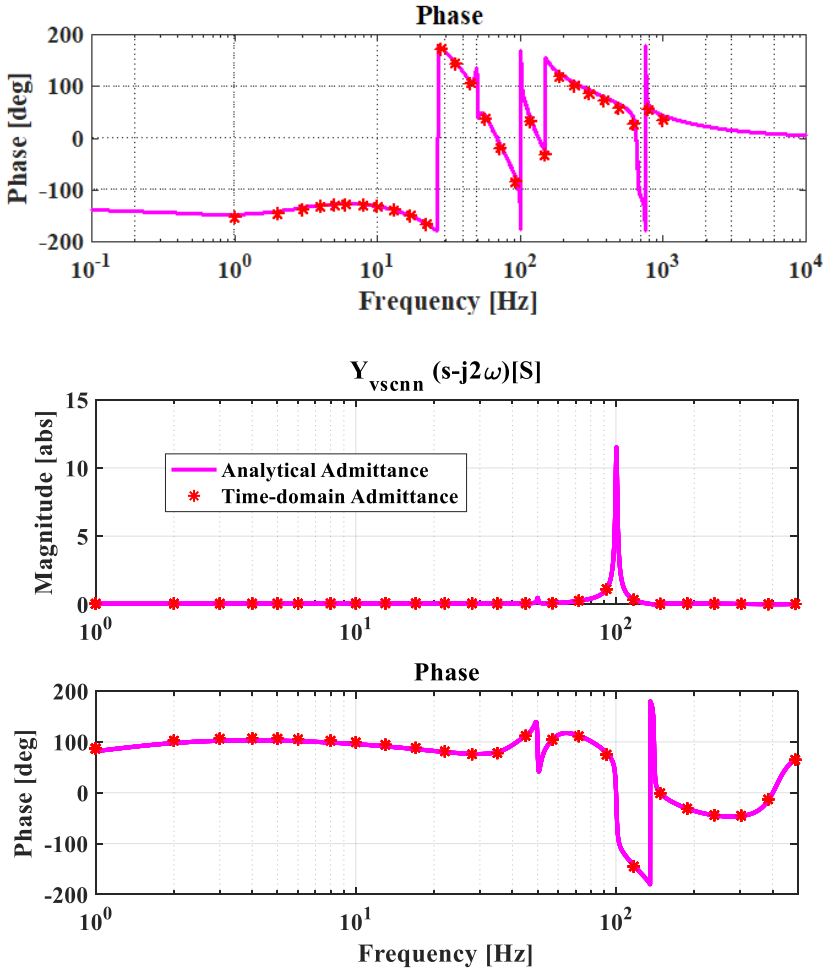

Fig. 6.6 Converter admittances of analytical model and time-domain model for the GFM VSC with *P* and *Q* control

The GFM VSC depicted in Fig. 6.1 has an outer control loops with P and Q control. Further studies using an outer control loop with P and AC voltage control (i.e., removal of the Q controller) are carried out as shown in Fig. 6.7. Using the same system and control parameters as in Fig. 6.1 and Table 6.1, the comparison of the small signal admittance $\mathbf{Y}_{vscPNTM}$ and the time-domain model admittance for the GFM with P and AC voltage control loop is illustrated in Fig. 6.8. As seen, the admittances match well, which validates the accuracy of the small signal model.

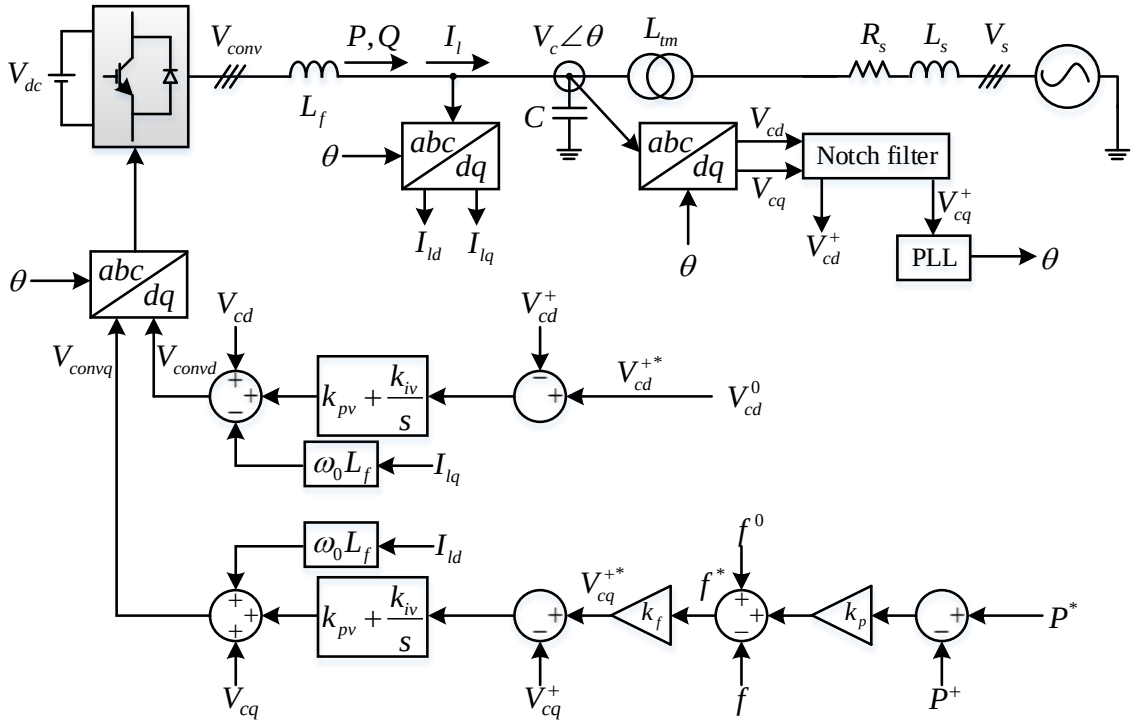

Fig. 6.7 The control configuration of the GFM VSC with *P* and voltage magnitude control

Comparing the admittances shown in Fig. 6.6 and Fig. 6.8, it can be seen that the removal of the outer Q control loop does not have much impact on the admittances of the system. It is also clear that in the low frequency range, e.g., below 100 Hz, the system admittances (especially the Y_{pp}) largely resemble the physical inductance of the converter system (with the admittance angle close to -90 degrees) as the GFM behaves as an internal voltage source behind an inductance.

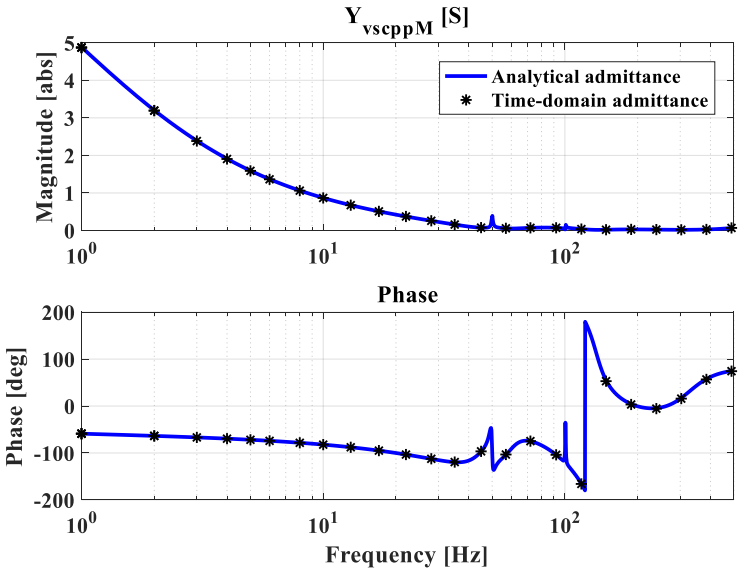
Y_{vsppM} [S]
Analytical admittance
Time-domain admittance
Magnitude [abs]
Phase
Phase [deg]
Frequency [Hz]

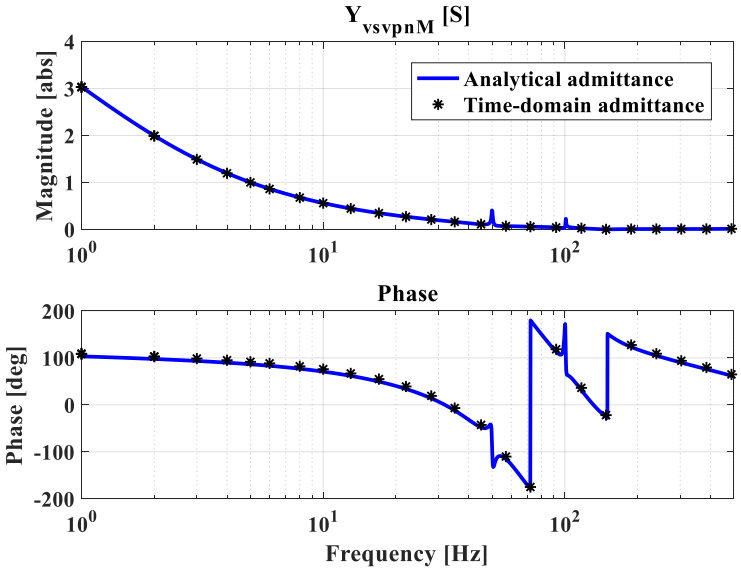
Y_{vsvpnM} [S]
Analytical admittance
Time-domain admittance
Magnitude [abs]
Phase
Phase [deg]
Frequency [Hz]

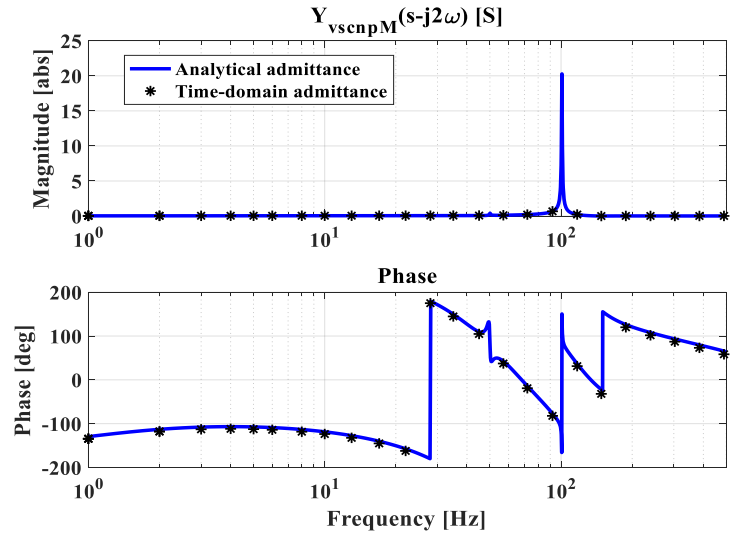
$Y_{vscnpM}(s-j2\omega)$ [S]
Analytical admittance
Time-domain admittance
Magnitude [abs]
Phase
Phase [deg]
Frequency [Hz]

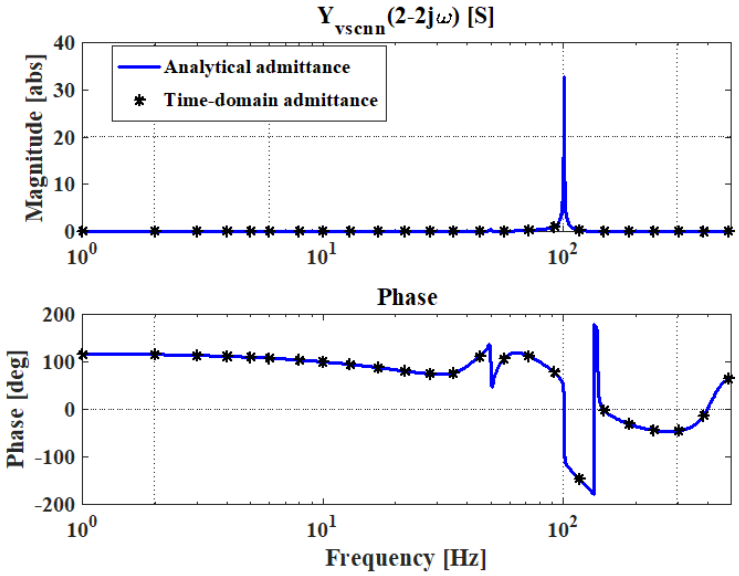

Fig. 6.8 Converter admittances of analytical model and time-domain model for the GFM VSC with *P* and AC voltage control

6.2 Admittance of the GFL VSC

As presented in Chapter 3, the general control system of the GFL VSC includes the AC voltage control and vector current control. By using the small signal model of the GFL built in [114], [161], [167], the analytical admittance $\mathbf{Y}_{vscPNT1}$ in the pn reference frame of the GFL VSC covering the impedance of the filter capacitor and transformer as shown in the pink boxed part of Fig. 6.9 can be obtained. To verify the accuracy of the analytical admittance $\mathbf{Y}_{vscPNT1}$, a time-domain model of the system using model of Fig. 6.9 is also built in MATLAB/Simulink, so the admittance can be measured. Same as the GFM cases, the GFL VSC transmits 1 pu active power to the AC grid with an SCR of 2. The DC voltage, power rating, LC filter, grid strength and transformer of the GFL VSC remain the same as those of the GFM VSC, while the system and control parameters are displayed in Table 6.2.

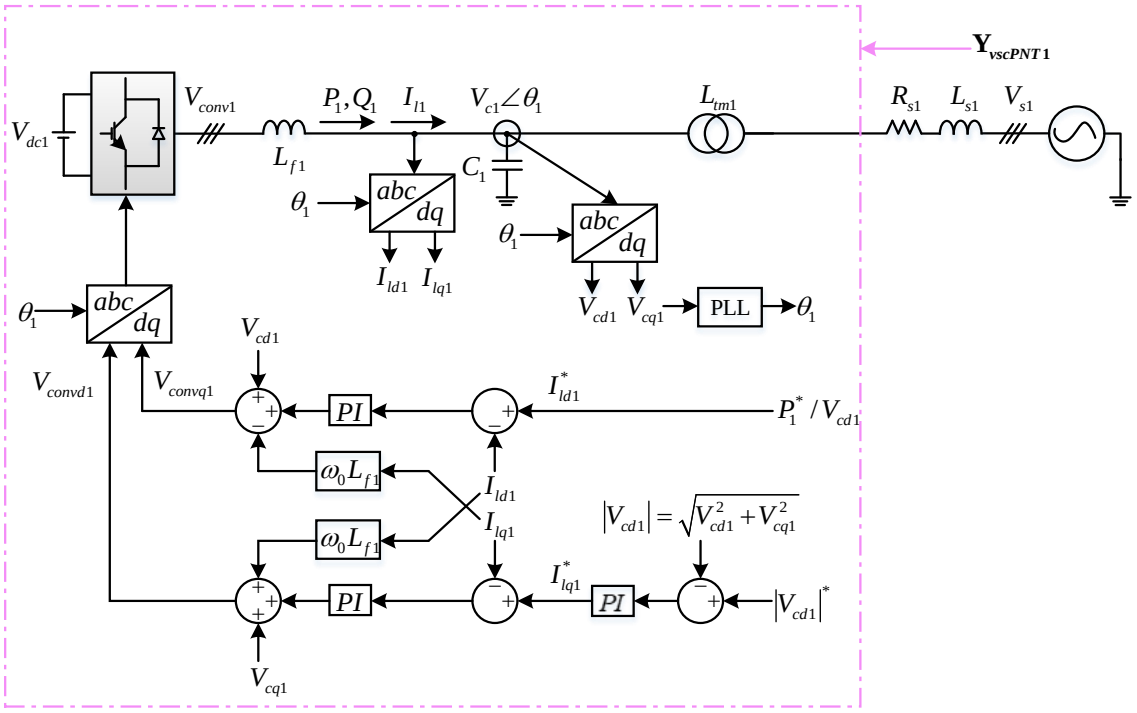

Fig. 6.9 System configuration of the GFL VSC

Fig. 6.10 compares the calculated and measured admittances of the GFL VSC, where the black lines refer to the calculated analytical admittances and the blue asterisks denote the measured admittances from the time-domain model. As shown, the admittances of the two models matches well, which indicates the accuracy of the analytical admittance. Comparing the results in Fig. 6.10 with those of Fig. 6.6 and Fig. 6.8, it can be seen that Y_{pp} has much lower admittance (high impedance) in the low frequency range than those of grid forming converter, i.e., GFL largely behaves as a current source with high internal impedance.

Table 6.2 System initial and control parameters

System parameters		
DC voltage V_{dc1}		100 kV
Power rating		500 MW
SCR		2
Nominal frequency ω_0 (f^0)		100 π rad/s (50 Hz)
Converter reactance L_{f1}		0.2 pu
Filter capacitance C_1		0.15 pu
Transformer (Y/Y), inductance L_{tm1}		55/110 kV, 0.05 pu
Control parameters of the GFL VSC (pu)		
PLL	Proportional gain k_{ppll1}	1
	Integral gain k_{ipll1}	78.54
Vector current control	Proportional gain k_{pi1}	0.54
	Integral gain k_{ii1}	114.51
AC voltage control	Proportional gain k_{pc1}	1.2
	Integral gain k_{iac1}	12.1

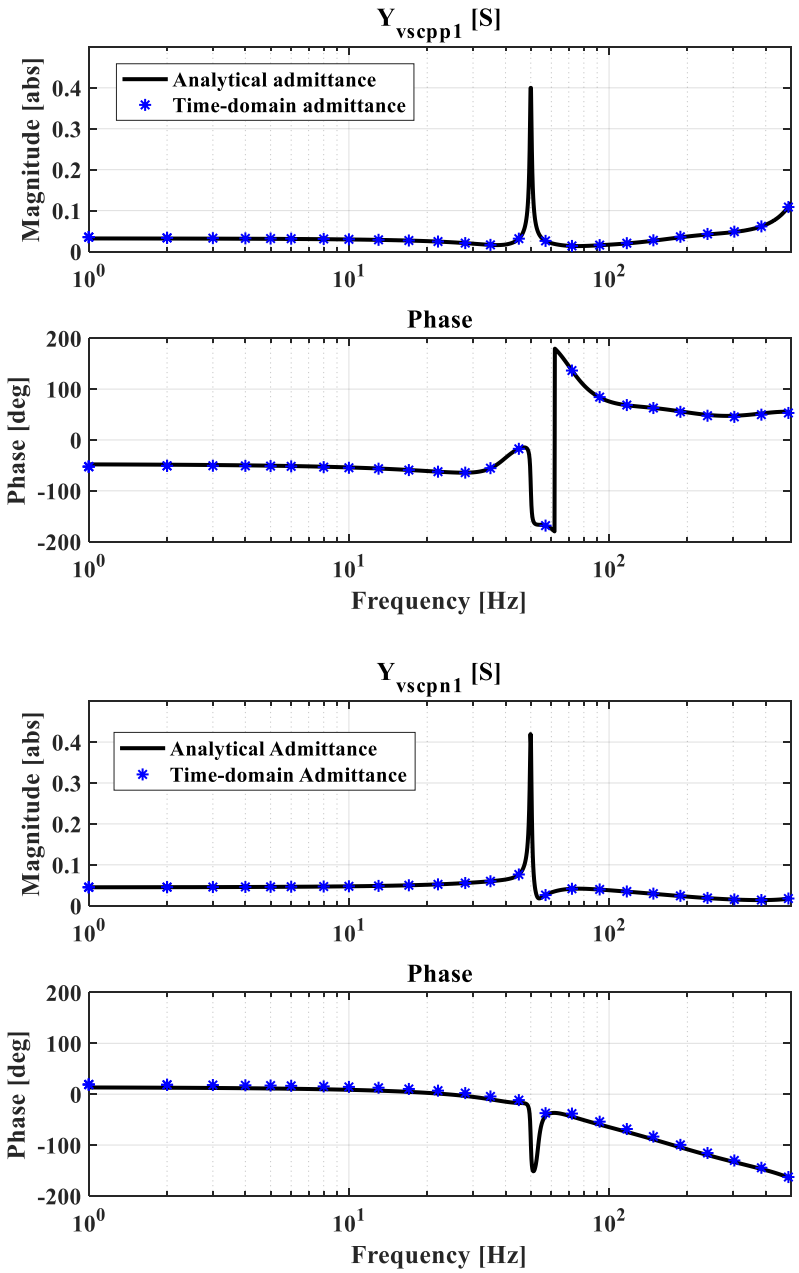
Y vscpp1 [S]
Analytical admittance
Time-domain admittance
Magnitude [abs]
0.4
0.3
0.2
0.1
0
10^0
10^1
10^2
Phase
200
100
0
-100
-200
Phase [deg]
Frequency [Hz]
Y vscpn1 [S]
Analytical Admittance
Time-domain Admittance
Magnitude [abs]
Phase
Phase [deg]
Frequency [Hz]

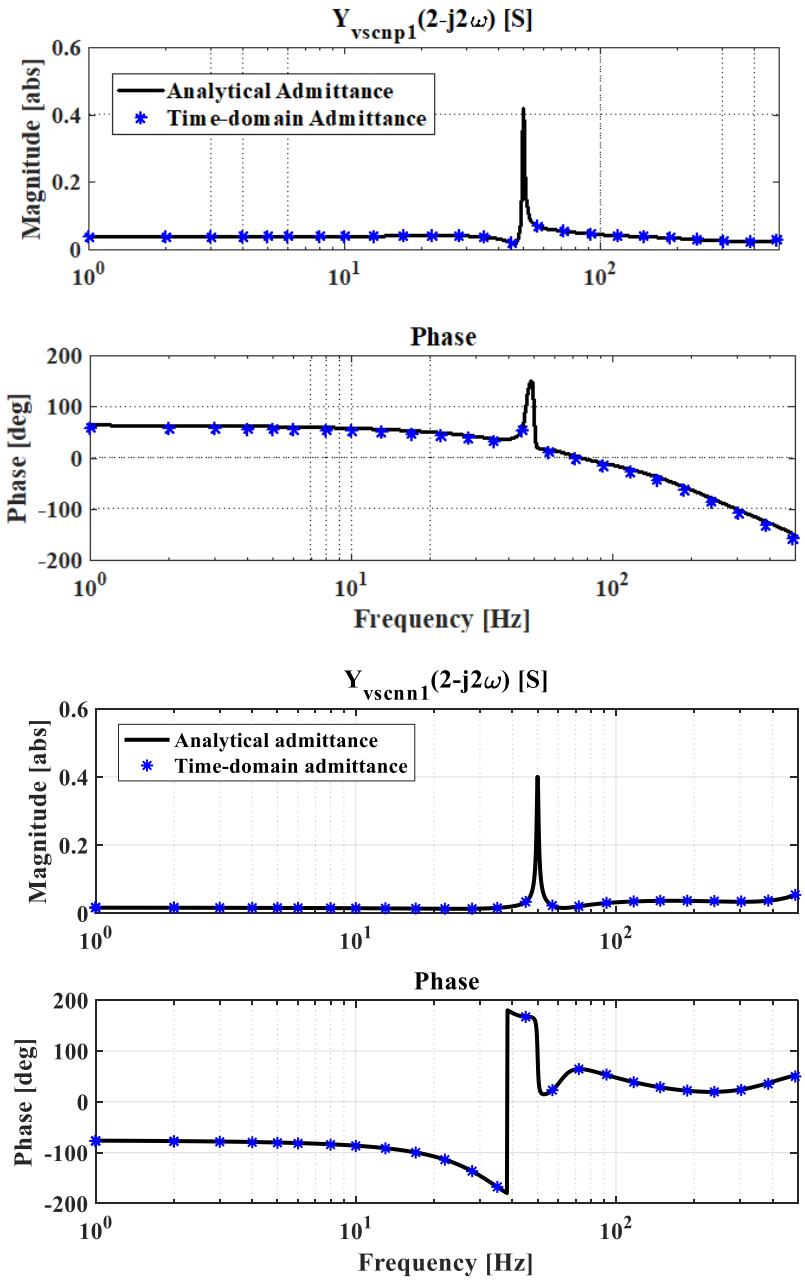

Fig. 6.10 Converter admittances of analytical model and time-domain model for the GFL VSC

6.3 Stability assessment of single grid connected VSC

According to the methods used in [114], [120], [161], the small signal equivalent circuit of the grid connected VSC can be depicted in Fig. 6.11. The VSC is represented by a Norton equivalent circuit in the form of a current source I_c in parallel with an equivalent admittance Y_{vsc} that includes the controller, LC filter and transformer, while the AC grid is modelled by its Thevenin equivalent circuit consisting of an ideal voltage source V_s in series with a grid impedance Z_s. Based on the equivalent circuit shown in Fig. 6.11 and the direction of current flow, the converter output current can be derived as:

$$I_o(s) = \frac{I_c(s)/Y_{vsc}(s) - V_s(s)}{Z_s(s) + 1/Y_{vsc}(s)} = \left[I_c(s) - Y_{vsc}(s)V_s(s)\right] \bullet \frac{1}{Y_{vsc}(s)Z_s(s) + 1} \tag{6.40}$$

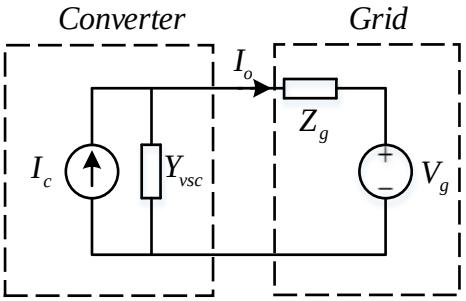

Fig. 6.11 Small signal equivalent circuit

It can be assumed that the converter is stable when the grid impedance is zero and the grid voltage is stable without the converter, i.e., both systems are stable before connection [120]. With consideration of the assumption and (6.40), the grid connected VSC can be stable if the product of the admittance of the VSC and the grid impedance $Y_{vsc}(s)Z_s(s)$ meets the Nyquist stability criterion that not encircling (-1,0) for $s = \omega_p$ with $-\infty < \omega_p < +\infty$ [114], [118], [117], [174].

With the grid impedances (SCR=2) in the pn reference frame $\mathbf{Z}_{sPN}$ for Fig. 6.1 and Fig. 6.7 and $\mathbf{Z}_{sPN1}$ for Fig. 6.9, the open-loop transfer function matrices $\mathbf{Y}_{vscPNT}\mathbf{Z}_{sPN}$ for the GFM VSC with P and Q control, $\mathbf{Y}_{vscPNTM}\mathbf{Z}_{sPN}$ for the GFM VSC with P and AC

voltage control, and $\mathbf{Y}_{vscPNT1}\mathbf{Z}_{sPN1}$ for the GFL VSC are investigated for stability analysis based on the Nyquist stability criterion. Fig. 6.12 compares the Nyquist plots of the GFM VSCs and GFL VSC, where λ_{v1} and λ_{v2} refer to the eigenvalues of $\mathbf{Y}_{vscPNT}\mathbf{Z}_{sPN}$ (GFM VSC with P and Q control), λ_{v3} and λ_{v4} denote the eigenvalues of $\mathbf{Y}_{vscPNTM}\mathbf{Z}_{sPN}$ (GFM VSC with P and AC voltage control), while λ_{i1} and λ_{i2} represent the eigenvalues of $\mathbf{Y}_{vscPNT1}\mathbf{Z}_{sPN1}$ (GFL VSC). As the two GFM VSCs have similar admittances, λ_{v1} and λ_{v2} almost overlap with λ_{v3} and λ_{v4}, as shown in Fig. 6.12. It can be seen that all the three converters are stable on the AC grid with SCR of 2 as λ_{v1}, λ_{v2}, λ_{v3}, λ_{v4}, λ_{i1} and λ_{i2} do not encircle (-1, 0). However, λ_{i1} and λ_{i2} for the GFL VSC are closer to (-1, 0) than λ_{v1}, λ_{v2}, λ_{v3} and λ_{v4} for the GFM VSCs. This indicates that the GFM VSC has a better stability than the GFL VSC on a weak grid with an SCR of 2.

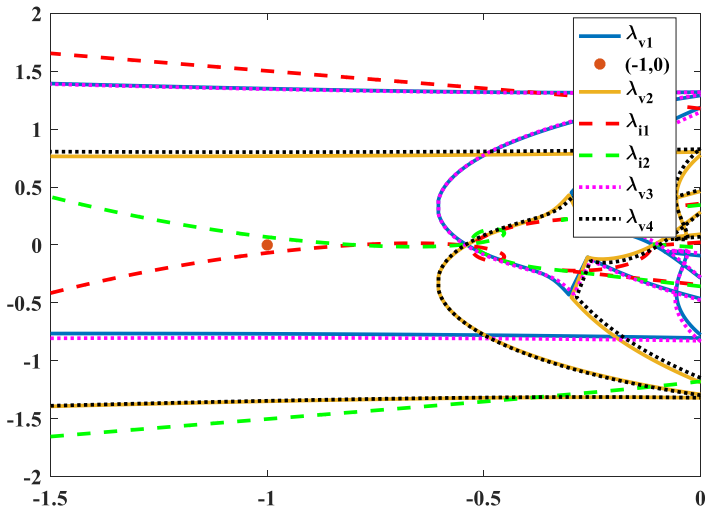

Fig. 6.12 Nyquist curve for the grid forming VSC and GFL VSC on a weak grid with an SCR of 2

Fig. 6.13 compares the time-domain simulation results when a small power step (10 MW, 0.02 pu at 8 s) is applied to the active power orders of the GFM VSCs and GFL VSC, respectively. It can be seen that the generated active power and voltage magnitudes of the two GFM VSCs settle down to the steady-state smoothly, which indicates good system stability. The reactive power droop controller slightly increases the voltage

magnitude due to the increment of active power for the GFM VSC with P and Q control as displayed in Fig. 6.13 (i), while the GFM VSC with P and AC voltage control maintains the voltage magnitude at the nominal level as depicted in Fig. 6.13 (ii). However, the corresponding responses of the GFL VSC settle down after a long duration of significant oscillations as illustrated in Fig. 6.13 (iii), which means a less stable system. The simulation results in time-domain proves the GFM VSC provides a better stability than the GFL VSC on a weak network with an SCR of 2, which verifies the effectiveness and accuracy of the stability analysis based on the small signal model. However, the results do indicate that the response speed of GFM during step change of active power is slow due to the inherent design.

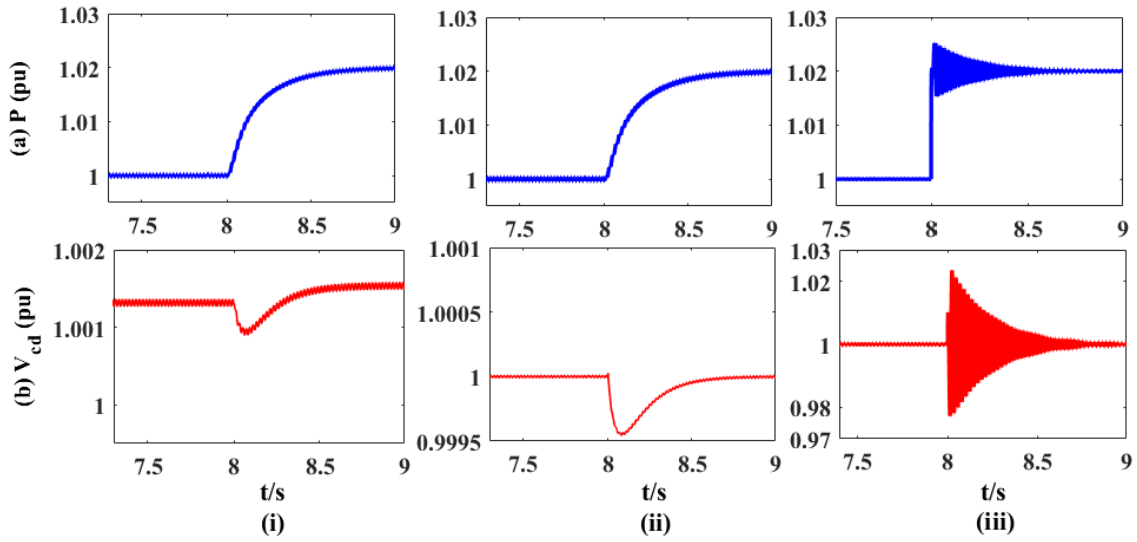

Fig. 6.13 Simulation results in time-domain for a power step (i) GFM VSC with *P* and *Q* control (ii) GFM VSC with *P* and AC voltage control (iii) GFL VSC with *P* and AC voltage control

6.4 Stability improvement with the GFM VSC on a very weak grid

To validate the grid-supporting function of the GFM VSC, two cases are tested, including the vector current control based GFL VSC (rated power of 500 MW) is connected to a very weak grid with an SCR of 1.3 (based on 500 MW) with a 100 MW GFM VSC (as shown in Fig. 6.14) and without (as shown in Fig. 6.9) connected to the network. The outer controller of the GFM VSC uses P and Q control. The system and control parameters are depicted in Table 6.2 and Table 6.3.

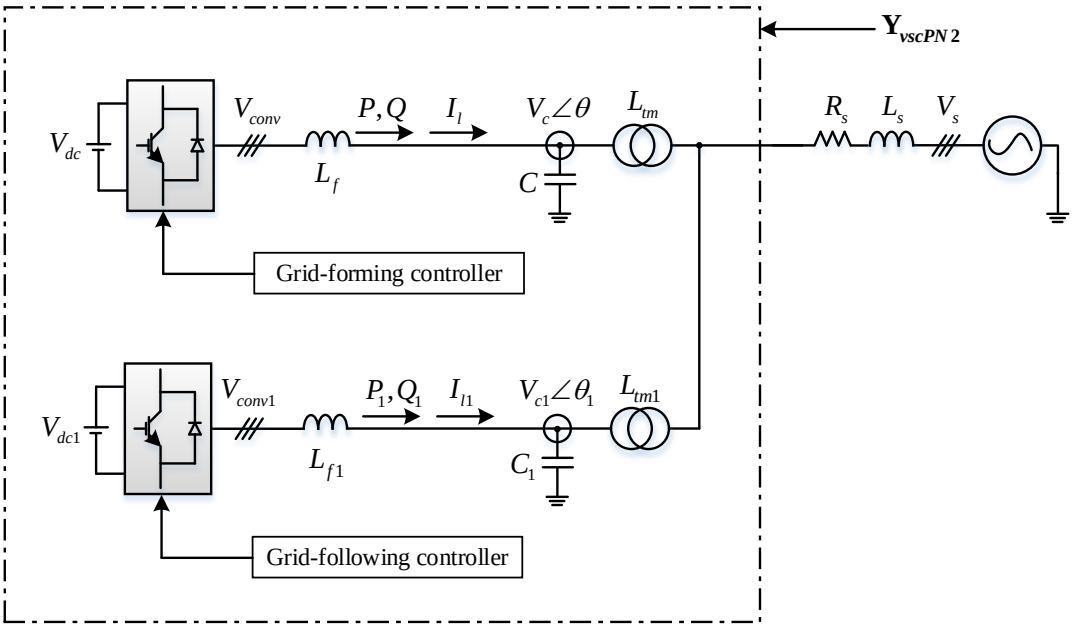

Fig. 6.14 System configuration of parallel VSCs

In Fig. 6.14, $\mathbf{Y}_{vscPNT2}$ represents the small signal admittance of the two parallel VSCs covering the impedance of the capacitors and transformers as in the black dotted box shown in Fig. 6.14, while $\mathbf{Z}_{sPN2}$ refers to the impedance of the AC grid (with a SCR of 1.3). Thus, the open-loop transfer function matrices $\mathbf{Y}_{vscPNT2}\mathbf{Z}_{sPN2}$ and $\mathbf{Y}_{vscPNT1}\mathbf{Z}_{sPN2}$ (without the GFM) are investigated to conduct the stability analysis of the GFL VSC with and without the GFM VSC connected on a very weak grid based on the Nyquist stability criterion, as shown in Fig. 6.15. λ_{vi1} and λ_{vi2} denote the eigenvalues of $\mathbf{Y}_{vscPNT2}\mathbf{Z}_{sPN2}$, while λ_{vi1} and λ_{vi2} represent the eigenvalues of $\mathbf{Y}_{vscPNT1}\mathbf{Z}_{sPN2}$. As shown in Fig. 6.15, the

GFL VSC becomes unstable as λ_{ii1} and λ_{ii2} encircles (-1, 0), while with the GFM VSC connected on the network, it is stable as λ_{vi1} and λ_{vi2} do not encircle (-1, 0). This proves that the GFM VSC improves the stability of the system on a very weak AC grid with an SCR of 1.3.

Table 6.3 System and control parameters of the GFM VSC uses *P* and *Q* control

System parameters		
DC voltage V_{dc}	100 kV	
Power rating	100 MW	
Nominal frequency ω_0 (f^0)	100π rad/s (50 Hz)	
Converter reactance L_f	0.2 pu	
Filter capacitance C	0.15 pu	
Transformer (Y/Y), inductance L_{tm}	55/110 kV, 0.05 pu	
Control parameters		
PLL	Proportional gain k_{ppll}	1
	Integral gain k_{ipll}	78.54
Power droop control	Active power order P^*	1
	reactive power order Q^*	0
	Active power droop coefficient k_p	0.02
	Reactive power droop coefficient k_q	0.02
Frequency droop control	Droop coefficient k_f	1.65
Direct voltage control	Proportional gain k_{pv}	1.08
	Integral gain k_{iv}	9.6

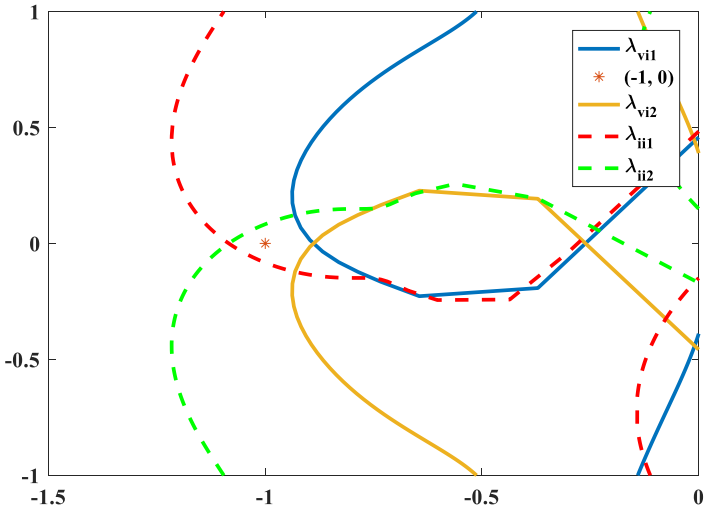

Fig. 6.15 Nyquist curve on a very weak network with an SCR of 1.3

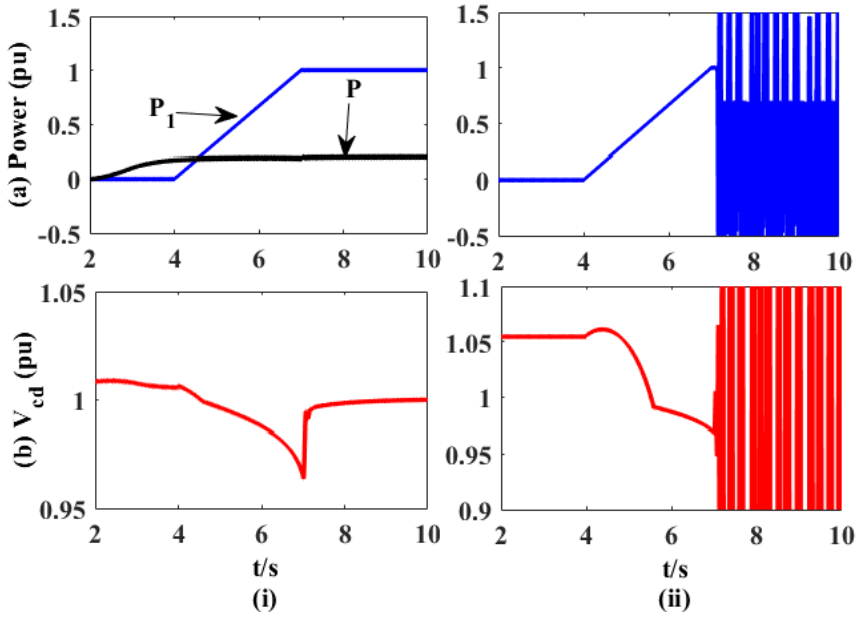

Fig. 6.16 Simulation results in time-domain of the GFL VSC with (i) and without (ii) the GFM VSC connected on a very weak network with an SCR of 1.3 (a) Active power (b) d-axis converter filter bus voltage

Fig. 6.16 compares the time-domain simulation results of the grid following VSC with and without the GFM VSC connected to a very weak AC grid. As can be seen from Fig. 6.16 (ii), without the GFM VSC connected on the network, the GFL VSC is unable to deliver 1 pu active power to the grid, and the system loses its control completely after

7.1s. When the GFM VSC is connected to the grid, as shown in Fig. 6.16 (i), the GFL now is able to generate 1 pu active power P_1 (500 MW) to the network with the support of the GFM VSC on the network while the GFM VSC also generates 100 MW active power P (1 pu based on its own rating of 100 MW) to the network. This proves that the GFM VSC with the proposed control strategy improves the stability of the system on a very weak AC grid and supports the operating of GFL. In addition, as seen from the results, the improvement to system stability is achieved by a relatively small GFM VSC (being one fifth of the rating of the GFL). The results also verify the effectiveness and accuracy of the small signal model depicted in Fig. 6.15.

6.3 Summary

This chapter studies the small signal admittance of the proposed GFM in Chapter 5. To simplify the system analysis, the admittance in the dq reference frame is transformed into the pn reference frame by applying the transforming equations. Simulations in time-domain models are also developed to verify the accuracy of the calculated small signal admittance. The admittances of GFM with different outer loops are compared with those of GFL. It has shown that the admittance of the GFM exhibits a voltage source behaviour with low impedance at low frequency range (e.g., below 100 Hz), while GFL has current source behaviour with high internal impedance at low frequency range.

The open-loop transfer function matrices are investigated to conduct the stability analysis using the Nyquist stability criterion. Based on the Nyquist plots and simulation results in time-domain, it has shown that on a weak AC grid, the GFM VSC provides a better stability compared to the GFL VSC. In addition, the GFM VSC can improve the stability and support the operation of the GFL VSC when both converters are connected to a very weak network (SCR=1.3 in the example).

Chapter 7 Conclusion and future work

7.1 General conclusions

This thesis mainly focuses on the control and operation of the GFM VSC for integrating renewable energy generations under various network conditions, including operation in grid connection and islanding networks.

The two main control classes of VSC, i.e., GFL and GFM converters, are presented and compared. A GFL converter acts as a controllable current source that follows the voltage at its terminals by precise synchronism (commonly using PLL) to control the current injections into the grid, hence the power flowing into the grid. Nevertheless, its performance relies on the assumption of a stiff external AC voltage which is usually provided by large presence of SGs in conventional power generation systems. This assumption will fail to hold up with more power electronic converters and less SGs in the future power systems. Consequently, the system can lose synchronisation and become unstable on weak or islanding networks. To overcome this weakness brought by the GFL converter, an alternative GFM converter is developed as an ideal AC voltage by regulating the local voltage and phase angle. Instead of PLL, the conventional GFM converter accomplishes the synchronisation with its terminals by simple droop control. Thus, the conventional GFM converter has the ability to work in both grid connection and islanding networks, but it lacks the capability of fault ride-through due to the absence of effective current control. Simulation results in time-domain verify the strength and weakness of the GFL and GFM converters.

In order to synthesise the advantages of both general GFM and GFL control, a universal GFM VSC control strategy is developed for grid connected and islanded operation. The proposed control schemes include adaptive power droop, frequency droop, PLL, direct voltage and current limit control. With the proposed control strategies, the GFM VSC is able to operate adequately on both grid connected and islanded operation. The transition from grid connection to island is smooth and seamless. During grid connection, the converter adjusts its active and reactive power generation with respect to the actual network frequency and voltage. When an external AC fault exists, the overall fault current

is effectively limited. Meanwhile, the active and reactive current are distributed to follow the current references provided according to voltage dip and overall fault current level. During islanding, the power generated by the converter is determined by the local load. Thus, the distribution of active and reactive current depends on the equivalent resistance and inductance of the local load on overload condition, while those are determined by the current references according to voltage dip and fault current level on a severe external fault.

To enable the GFM VSC to have fault ride-through capability for both asymmetrical and symmetrical AC faults, the GFM VSC control is coordinated with an enhanced AC fault current limit control when the connected grid is weak. The fault current control system is based on double synchronous reference frames to control the positive- and negative-components independently. An additional voltage balancing control loop is also developed to retain the AC voltage control loop for fault current limiting. In the developed scheme, the d-axis voltage order fed into the direct voltage control loop is adjusted to avoid overvoltage and over-modulations. An enhanced dq current distribution control is proposed to accordingly distribute the active and reactive current during faults, which only works during faults so normal operation of the converter is not affected. To specifically control the negative-sequence current, an extra negative-sequence current control is employed, which mimics the conventional current control to flexibly control the negative-sequence dq current with respect to the pre-set references.

To validate the improved small signal stability with the proposed GFM control in comparison to the conventional GFL control, the impedance-based small signal assessment method is used. The admittance of the converter in the system dq reference frame is derived with the small signal model, which is then transformed into the admittance in the pn reference frame to simplify the analysis. The open-loop transfer function matrices of the overall system are used to conduct the stability analysis based on the Nyquist stability criterion. To validate the analytical results, time-domain simulation results are also tested. It can be found that the proposed GFM VSC not only provides a better stability than the GFL VSC on a weak grid, but also can improve the stability and support the operation of the GFL VSC on a very weak grid.

7.2 Suggestions for future work

Based on the studies and achievements in this thesis, the potential areas for future research are proposed as follows:

- The GFM VSC in this thesis focuses on performance of the AC side, and the DC side is assumed to be a fixed DC source. It is worthwhile investigating the potential impact of the proposed control method on the DC side may be connected to a wind farm drive train or other energy storage system.
- The transitions between normal GFM control and fault current limiting operation during and after large network transients can be further investigated, to ensure smooth switching of the different control mode, so as to minimise any adverse effect on the operation of the power network.
- The provision of fault current from the GFM VSC can be further investigated for future network with large converter penetration. This can include the provision of active and reactive fault current, as well as the provision of negative-sequence current during various fault conditions.
- Experimental tests for the proposed GFM VSC control methods can be demonstrated to further verified the grid-supporting functions and fault ride-through capability.

References

[1] UN Climate Change Conference, “Maintaining a clear intention to keep 1.5°C within reach,” 2022. https://unfccc.int/maintaining-a-clear-intention-to-keep-15degc-within-reach.

[2] D. Jones, “Global Electricity Review 2021,” 2021. [Online]. Available: https://ember-climate.org/app/uploads/2021/03/Global-Electricity-Review-2021.pdf.

[3] D. Gibb, N. Ledanois, L. Ranalder, and H. Yaqoob, “Renewables 2022 global status report,” 2022. [Online]. Available: https://www.ren21.net/wp-content/uploads/2019/05/GSR2022_Full_Report.pdf.

[4] M. Wiatros-Motyka, “Global electricity review 2023,” 2023. [Online]. Available: file:///C:/Users/Yuan Lu/Downloads/Global-Electricity-Review-2023 (1).pdf.

[5] Laura Cozzi, T. Gould, S. Bouckaert, and C. McGlade, “World energy outlook 2022,” https://iea.blob.core.windows.net/assets/830fe099-5530-48f2-a7c1-11f35d510983/WorldEnergyOutlook2022.pdf, 2022. [Online]. Available: https://www.iea.org/reports/world-energy-outlook-2022.

[6] M. A. R. Bueno, “Renewables 2023 global status report,” 2023. [Online]. Available: https://www.ren21.net/wp-content/uploads/2019/05/GSR2023_GlobalOverview_Full_Report_with_endnotes_web.pdf.

[7] European Environment Agency, “Share of energy consumption from renewable sources in Europe,” 2023. https://www.eea.europa.eu/ims/share-of-energy-consumption-from (accessed Jun. 28, 2023).

[8] REN21, “Renewables 2021 global status report,” 2021. [Online]. Available: https://abdn.pure.elsevier.com/en/en/researchoutput/ren21(5d1212f6-d863-45f7-8979-5f68a61e380e).html.

[9] R. Hannah, R. Max, and P. Rosado, “Renewable energy,” *Our World in Data,* 2020. https://ourworldindata.org/renewable-energy#installed-wind-capacity (accessed

Jun. 30, 2023).

[10] B. Kroposki *et al.*, “Achieving a 100% renewable grid: operating electric power systems with extremely high levels of variable renewable energy,” *IEEE Power and Energy Magazine*, vol. 15, no. 2, IEEE, pp. 61–73, 2017.

[11] Offshore Wind Innovation Hub, “Future offshore wind energy integration: outlook & analysis,” 2020. [Online]. Available: https://offshorewindinnovationhub.com/industry_insight/future-offshore-wind-energy-integration-outlook-analysis/.

[12] A. Yazdani and R. Iravani, *Voltage-Source Converters in Power Systems: Modeling, Control, and Applications*. 2010.

[13] D. Chen and L. Xu, “Autonomous DC voltage control of a DC microgrid with multiple slack terminals,” *IEEE Trans. Power Syst.*, vol. 27, no. 4, pp. 1897–1905, 2012.

[14] C. M. Nikos Hatziargyrious, Hiroshi Asano, Reza Iravani, “Mircrogrids,” in *IEEE Power and Energy Magzine*, vol. 5, no. 4, pp. 78–94, 2007.

[15] S. K. Chaudhary, R. Teodorescu, and P. Rodriguez, “Wind farm grid integration using VSC based HVDC transmission - an overview,” in *2008 IEEE Energy 2030 Conference*, pp. 1–7, 2009.

[16] Entsoe, “Voltage Source Converters.” https://www.entsoe.eu/Technopedia/techsheets/voltage-source-converters (accessed Mar. 30, 2023).

[17] M. A. Zamani, A. Yazdani, and T. S. Sidhu, “A control strategy for enhanced operation of inverter-based microgrids under transient disturbances and network faults,” *IEEE Trans. Power Deliv.*, vol. 27, no. 4, pp. 260–265, 2012.

[18] A. G. Paspatis, G. C. Konstantopoulos, M. Mayfield, and V. C. Nikolaidis, “Current-limiting droop controller with fault-ride-through capability for grid-tied inverters,” in *2017 IEEE PES Innovative Smart Grid Technologies Conference, (ISGT-Europe 2017)*, pp. 1–6, 2017.

[19] J. Shair, H. Li, J. Hu, and X. Xie, “Power system stability issues, classifications

and research prospects in the context of high-penetration of renewables and power electronics," *Renew. Sustain. Energy Rev.*, vol. 145, pp. 1–16, 2021.

[20] K. S. Ratnam, K. Palanisamy, and G. Yang, "Future low-inertia power systems: requirements, issues, and solutions - a review," *Renew. Sustain. Energy Rev.*, vol. 124, pp. 1–24, 2020.

[21] N. Hatziargyriou *et al.*, "Definition and classification of power system stability - revisited & extended," *IEEE Trans. Power Syst.*, vol. 36, no. 4, pp. 3271–3281, 2021.

[22] J. Hugel, "Control of syncrhonous generators," in *Control System, Robotics, And Automation*, vol. XVIII, pp. 224–233.

[23] A. Egea-alvarez, S. Fekriasl, F. Hassan, and O. Gomis-Bellmunt, "Advanced vector control for voltage source converters connected to weak grids," *IEEE Trans. Power Syst.*, vol. 30, no. 6, pp. 3072–3081, 2015.

[24] K. Givaki, D. Chen, and L. Xu, "Current error based compensations for VSC current control in weak grids for wind farm applications," *IEEE Trans. Sustain. Energy*, vol. 10, no. 1, pp. 26–35, 2019.

[25] S. L. Lorenzen, A. b. Nielsen, and L. Bede, "Control of a grid connected converter during weak grid conditions," in *IEEE 7th International Symposium on Power Electronics for Distributed Generation Systems*, pp. 2329–5767, 2016.

[26] M. Evans, C. Bono, and Y. Wang, "Toward net-zero electricity in europe: what are the challenges for the power system?," *IEEE Power and Energy Magazine*, vol. 20, pp. 44–54, 2022.

[27] Electrical Concepts, "Short Circuit Ratio-Definition, Calculation and Significance," 2018. https://electricalbaba.com/short-circuit-ratio-definition-calculation-significance/#google_vignette (accessed Nov. 04, 2023).

[28] M. H. Nawir, "Integration of wind farms into weak AC Grids," Cardiff University, 2017.

[29] "IEEE Guide for Planning DC Links Terminating at AC Locations Having Low Short-Circuit Capacities," *IEEE Standard 1204-1997*. 1997.

[30] J. Schmall, S. H. Huang, Y. Li, J. Billo, J. Conto, and Z. Yang, “Voltage stability of large-scale wind plants integrated in weak networks: an ERCOT case study,” in *IEEE Power and Energy Society General Meeting*, pp. 4–8, 2015.

[31] H. Sharma, S. Islam, and C. V. Nayar, “Power quality simulation of a variable speed wind generator connected to a weak grid,” in *International Conference on Harmonics and Quality of Power (ICHQP)*, pp. 988–993, 2000.

[32] M. Dreidy, H. Mokhlis, and S. Mekhilef, “Inertia response and frequency control techniques for renewable energy sources: a review,” *Renew. Sustain. Energy Rev.*, vol. 69, pp. 144–155, 2017, [Online]. Available: http://dx.doi.org/10.1016/j.rser.2016.11.170.

[33] B. J. Matevosyan, H. Urdal, S. Achilles, J. Macdowell, J. O. Sullivan, and R. Quint, “Grid-forming inverters: are they the key for high renewable penetration,” *IEEE Power and Energy Magazine*, vol. 17, no. 6, pp. 89–98, 2019.

[34] R. W. Kenyon *et al.*, “Stability and control of power systems with high penetrations of inverter-based resources: an accessible review of current knowledge and open questions,” *Sol. Energy*, vol. 210, pp. 149–168, 2020.

[35] U. Münz and D. Romeres, “Region of attraction of power systems,” in *IFAC Proceedings Volumes (IFAC-PapersOnline)*, vol. 4, pp. 49–54, 2013.

[36] S. Eftekharnejad, V. Vittal, G. T. Heydt, B. Keel, and J. Loehr, “Impact of increased penetration of photovoltaic generation on power systems,” *IEEE Trans. Power Syst.*, vol. 28, no. 2, pp. 893–901, 2013.

[37] X. Wang and F. Blaabjerg, “Harmonic stability in power electronic-based power systems: concept, modeling, and analysis,” *IEEE Trans. Smart Grid*, vol. 10, no. 3, pp. 2858–2870, 2019.

[38] J. Miret, M. Castilla, and L. Garci, “Hierarchical control of intelligent microgrids,” *IEEE Industrial Electronics Magazine*, vol. 4, no. 4, pp. 23–29, 2010.

[39] P. Kumar, V. Kumar, and B. Tyagi, “Detection of islanding for microgrid based on discrimination factor of islanding,” in *2020 21st National Power Systems Conference (NPSC)*, pp. 1–5, 2020.

[40] C. A. Plet, M. Graovac, T. C. Green, and R. Iravani, “Fault response of grid-connected inverter dominated networks,” in *IEEE PES General Meeting*, pp. 1–8, 2010.

[41] S. F. Zarei, H. Mokhtari, M. A. Ghasemi, and F. Blaabjerg, “Reinforcing fault ride through capability of grid forming voltage source converters using an enhanced voltage control scheme,” *IEEE Trans. Power Deliv.*, vol. 34, no. 5, pp. 1827–1842, 2019.

[42] N. Bottrell and T. C. Green, “Comparison of current-limiting strategies during fault ride-through of inverters to prevent latch-up and wind-up,” *IEEE Trans. Power Electron.*, vol. 29, no. 7, pp. 3786–3797, 2014.

[43] A. Zamani, T. Sidhu, and A. Yazdani, “A strategy for protection coordination in radial distribution networks with distributed generators,” in *IEEE PES General Meeting*, pp. 1–8, 2010.

[44] S. F. Zarei and M. Parniani, “A comprehensive digital protection scheme for low-voltage microgrids with inverter-based and conventional distributed generations,” *IEEE Trans. Power Deliv.*, vol. 32, no. 1, pp. 441–452, 2017.

[45] H. R. Chamorro, M. Ghandhari, and R. Eriksson, “Coherent groups identification under high penetration of non-synchronous generation,” in *2016 IEEE Power and Energy Society General Meeting (PESGM)*, pp. 1–5, 2016.

[46] A. F. Hoke *et al.*, “The Frequency-Watt Function: Simulation and Testing for the Hawaiian Electric Companies,” 2017. [Online]. Available: https://www.nrel.gov/docs/fy17osti/68884.pdf.

[47] D. Pattabiraman, R. H. Lasseter, and T. M. Jahns, “Comparison of grid following and grid forming control for a high inverter penetration power system,” in *IEEE Power and Energy Society General Meeting*, pp. 3–7, 2018.

[48] H. Zhang, W. Xiang, W. Lin, and J. Wen, “Grid forming converters in renewable energy sources dominated power grid: control strategy, stability, application, and challenges,” *J. Mod. Power Syst. Clean Energy*, vol. 9, no. 6, pp. 1239–1256, 2021.

[49] M. Anderson-Cook and C. M. Borror, “Paving the way: A future without inertia is

closer than you think," *IEEE Power and Energy Magzine*, vol. 15, no. 6, pp. 61–69, 2017.

[50] J. Rocabert, A. Luna, F. Blaabjerg, and P. Rodríguez, "Control of power converters in AC microgrids," *IEEE Trans. Power Electron.*, vol. 27, no. 11, pp. 4734–4749, 2012.

[51] R. H. Lasseter, Z. Chen, and D. Pattabiraman, "Grid-forming inverters: A critical asset for the power grid," *IEEE J. Emerg. Sel. Top. Power Electron.*, vol. 8, no. 2, pp. 925–935, 2020.

[52] W. Du, K. P. Schneider, F. K. Tuffner, Z. Chen, and R. H. Lasseter, "Modeling of grid-forming inverters for transient stability simulations of an all inverter-based distribution system," in *2019 IEEE Power and Energy Society Innovative Smart Grid Technologies Conference, ISGT 2019*, pp. 1–5, 2019.

[53] P. Unruh, M. Nuschke, P. Strauß, and F. Welck, "Overview on grid-forming inverter control methods," *Energies*, vol. 13, no. 10, 2020.

[54] A. Khatri, "Evolution of future electrical networks in Eskom," 2010.

[55] D. Dong, J. Li, D. Boroyevich, P. Mattavelli, I. Cvetkovic, and Y. Xue, "Frequency behavior and its stability of grid-interface converter in distributed generation systems," in *2012 Twenty-Seventh Annual IEEE Applied Power Electronics Conference and Exposition (APEC)*, pp. 1887–1893, 2012.

[56] M. C. Chandorkar, D. M. Divan, and R. Adapa, "Control of parallel connected inverters in standalone ac supply systems," *IEEE Trans. Ind. Appl.*, vol. 29, no. 1, pp. 136–143, 1993.

[57] U. Bashir Tayab, M. Azrik Bin Roslan, L. Jenn Hwai, and M. Kashif, "A review of droop control techniques for microgrid," *Renew. Sustain. Energy Rev.*, vol. 76, pp. 717–727, 2017, [Online]. Available: http://dx.doi.org/10.1016/j.rser.2017.03.028.

[58] T. Weckesser, H. Johannsson, and J. Ostergaard, "Impact of model detail of synchronous machines on real-time transient stability assessment," in *2013 IREP Symposium Bulk Power System Dynamics and Control - IX Optimization, Security*

and Control of the Emerging Power Grid, pp. 1–9, 2013.

[59] H. R. Baghaee, M. Mirsalim, G. B. Gharehpetian, and H. A. Talebi, "A current limiting strategy to improve fault ride-through of inverter interfaced autonomous microgrids," *IEEE Trans. Smart Grid*, vol. 24, no. 5, pp. 71–81, 2017.

[60] A. Abdelrahim, P. Mckeever, and M. Smailes, "Modified grid forming converter controller with fault ride through capability without PLL or current loop," in *18th Wind Integration Workshop*, pp. 1–8, 2019.

[61] S. Pholboon, M. Sumner, and R. Ierna, "Virtual synchronous machine control for grid transmission compliance studies," in *2019 International Conference on Smart Energy Systems and Technologies (SEST)*, pp. 1–5, 2019.

[62] M. Saeedian, B. Pournazarian, S. S. Seyedalipour, B. Eskandari, and E. Pouresmaeil, "Emulating rotational inertia of synchronous machines by a new control technique in grid-interactive converters," *Sustainability*, vol. 12, no. 13, pp. 1–14, 2020.

[63] H.-P. Beck and R. Hesse, "Virtual synchronous machine," in *2007 9th International Conference on Electrical Power Quality and Utilisation*, pp. 1–6, 2007.

[64] Y. Chen, R. Hesse, D. Turschner, and H.-P. Beck, "Improving the grid power quality using virtual synchronous machines," in *International Conference on Power Engineering, Energy and Electrical Drives*, pp. 1–6, 2011.

[65] Y. Chen, R. Hesse, D. Turschner, and H.-P. Beck, "Investigation of the virtual synchronous machine in the island mode," in *2012 3rd IEEE PES Innovative Smart Grid Technologies Europe (ISGT Europe)*, pp. 1–6, 2012.

[66] M. Ebrahimi, S. A. Khajehoddin, and M. Karimi-Ghartemani, "An improved damping method for virtual synchronous machines," *IEEE Trans. Sustain. Energy*, vol. 10, no. 3, pp. 1491–1500, 2019.

[67] Y. Chen, R. Hesse, D. Turschner, and H. Beck, "Comparison of methods for implementing virtual synchronous machine on inverters Key words," in *Proceeding of the International Conference on Renewable Energies and Power*

Quality (ICREPQ'12), pp. 734–739, 2012.

[68] Q.-C. Zhong and G. Weiss, "Synchronverters: inverters that mimic synchronous generators," *IEEE Trans. Ind. Electron.*, vol. 58, no. 4, pp. 1259–1267, 2011.

[69] Q. Zhong, P. Nguyen, Z. Ma, and W. Sheng, "Self-synchronized synchronverters : inverters without a dedicated synchronization unit," *IEEE Trans. Power Electron.*, vol. 29, no. 2, pp. 617–630, 2014.

[70] S. Dong and Y. C. Chen, "Adjusting synchronverter dynamic response speed via damping correction loop," *IEEE Trans. Energy Convers.*, vol. 32, no. 2, pp. 608–619, 2017.

[71] Y. Hirase, K. Abe, and O. Noro, "Stabilization effect of virtual synchronous generators in microgrids with highly penetrated renewable energies," in *2016 IEEE 17th Workshop on Control and Modeling for Power Electronics (COMPEL)*, pp. 1–8, 2016.

[72] S. D'Arco, J. A. Suul, and O. B. Fosso, "A Virtual Synchronous Machine implementation for distributed control of power converters in SmartGrids," *Electr. Power Syst. Res.*, vol. 122, pp. 180–197, 2015, [Online]. Available: http://dx.doi.org/10.1016/j.epsr.2015.01.001.

[73] Y. Wang, L. Luo, T. Li, Y. Chen, and Y. Fu, "Research on control strategy of improved virtual synchronous generator for improving the operating capability of passive isolated islands," in *2019 IEEE PES Innovative Smart Grid Technologies Asia, ISGT 2019*, pp. 1485–1490, 2019.

[74] L. Zhang, L. Harnefors, and H. Nee, "Power-synchronization control of grid-connected voltage-source converters," *IEEE Trans. Power Syst.*, vol. 25, no. 2, pp. 809–820, 2010.

[75] Z. Shuai, W. Huang, C. Shen, J. Ge, and Z. J. Shen, "Characteristics and restraining method of fast transient inrush fault currents in synchronverters," *IEEE Trans. Ind. Electron.*, vol. 64, no. 9, pp. 7487–7497, 2017.

[76] K. Shi, W. Song, X. Peifeng, L. Rongke, F. Zhiming, and J. Yi, "Low-voltage ride-through control strategy for a virtual synchronous generator based on smooth

switching," *IEEE A*, vol. 6, pp. 2703–2711, 2018.

[77] S. Mukherjee, P. Shamsi, and M. Ferdowsi, "Improved virtual inertia based control of a grid connected voltage source converter with fault ride-through ability," in *2016 North American Power Symposium (NAPS)*, pp. 1–6, 2016.

[78] K. O. Oureilidis and C. S. Demoulias, "A fault clearing method in converter-dominated microgrids with conventional protection means," *IEEE Trans. Power Electron.*, vol. 31, no. 6, pp. 4628–4640, 2016.

[79] M. G. Taul, X. Wang, P. Davari, and F. Blaabjerg, "Current limiting control with enhanced dynamics of grid-forming converters during fault conditions," *IEEE J. Emerg. Sel. Top. Power Electron.*, vol. 8, no. 2, pp. 1062–1073, 2020.

[80] A. D. Paquette and D. M. Divan, "Virtual impedance current limiting for inverters in microgrids with synchronous generators," *IEEE Trans. Ind. Appl.*, vol. 51, no. 2, pp. 1630–1638, 2015.

[81] L. Huang, H. Xin, Z. Wang, L. Zhang, K. Wu, and J. Hu, "Transient stability analysis and control design of droop-controlled voltage source converters considering current limitation," *IEEE Trans. Smart Grid*, vol. 10, no. 1, pp. 578–591, 2019.

[82] C. A. Plet and T. C. Green, "A method of voltage limiting and distortion avoidance for islanded inverter-fed networks under fault," in *Proceedings of the 2011 14th European Conference on Power Electronics and Applications*, pp. 1–8, 2011.

[83] T. C. Green and M. Prodanovic, "Control of inverter-based micro-grids," *Electr. Power Syst. Res.*, vol. 77, no. 9, pp. 1204–1213, 2007.

[84] J. M. Guerrero, N. Berbel, J. Matas, L. G. de Vicuna, and J. Miret, "Decentralized control for parallel Operation of distributed generation inverters in microgrids using resistive output impedance," in *IECON 2006 - 32nd Annual Conference on IEEE Industrial Electronics*, pp. 5149–5154, 2006.

[85] J. M. Guerrero, J. C. Vásquez, J. Matas, M. Castilla, and L. García de Vicuna, "Control strategy for flexible microgrid based on parallel line-interactive UPS systems," *IEEE Trans. Ind. Electron.*, vol. 56, no. 3, pp. 726–736, 2009.

[86] J. He and Y. W. Li, “Analysis, design, and implementation of virtual impedance for power electronics interfaced distributed generation,” *IEEE Trans. Ind. Appl.*, vol. 47, no. 6, pp. 2525–2538, 2011.

[87] A. Gkountaras, S. Dieckerhoff, and T. Sezi, “Evaluation of current limiting methods for grid forming inverters in medium voltage microgrids,” in *2015 IEEE Energy Conversion Congress and Exposition, ECCE 2015*, pp. 1223–1230, 2015.

[88] Y. Liu, Y. Wang, X. Liu, M. Wang, Z. Xu, and H. Liu, “Steady-state angle stability analysis of parallel grid-forming converters in current saturation mode,” *IEEE Trans. Power Electron.*, vol. 38, no. 1, pp. 8039–8044, 2023.

[89] L. Zhang, L. Harnefors, and H. P. Nee, “Modelling and control of VSC-HVDC connected to island systems,” in *IEEE PES General Meeting, PES 2010*, pp. 1–8, 2010.

[90] Z. Zhang, D. Chen, K. Givaki, and L. Xu, “A Less-Intrusive Approach to Stabilize VSC Transmission against Highly Variable Grid Strength,” *IEEE J. Emerg. Sel. Top. Power Electron.*, vol. 9, no. 6, pp. 7199–7211, 2021.

[91] J. Svensson, “Synchronisation methods for grid-connected voltage source converters,” in *IEE Proceedings: Generation, Transmission and Distribution*, pp. 229–235, 2001.

[92] J. Roldan-Perez, E. J. Bueno, R. Peña-Alzola, and A. Rodriguez-Cabero, “All-pass-filter-based active damping for VSCs with LCL filters connected to weak grids,” *IEEE Trans. Power Electron.*, vol. 33, no. 11, pp. 9890–9901, 2018.

[93] A. Wu, Z. Yuan, H. Rao, B. Zhou, and H. Li, “Analysis of power transmission limit for the VSC-HVDC feeding weak grid,” *J. Eng.*, vol. 2019, no. 16, pp. 2916–2920, 2019.

[94] F. Salha, F. Colas, and X. Guillaud, “Virtual resistance principle for the overcurrent protection of PWM voltage source inverter,” in *2010 IEEE PES Innovative Smart Grid Technologies Conference Europe (ISGT Europe)*, pp. 1–6, 2010.

[95] L. Huang, C. Wu, D. Zhou, L. Chen, D. Pagnani, and F. Blaabjerg, “Challenges

and potential solutions of grid-forming converters applied to wind power generation system—an overview," *Front. Energy Res.*, vol. 11, no. January, pp. 1–14, 2023.

[96] X. Guo, W. Liu, and Z. Lu, "Flexible power regulation and current-limited control of the grid-connected inverter under unbalanced grid voltage faults," *IEEE Trans. Ind. Electron.*, vol. 64, no. 9, pp. 7425–7432, 2017.

[97] N. Tleis, *Power Systems Modelling and Fault Analysis*, 2nd Edtion. Elsevier, 2019.

[98] A. Ingalalli and S. Kamalasadan, "A universal multiple inverter control architecture with droop for unbalanced distribution grid," in *2021 IEEE Power & Energy Society Innovative Smart Grid Technologies Conference (ISGT)*, pp. 1–5, 2021.

[99] B. Mahamedi, M. Eskandari, J. E. Fletcher, and J. Zhu, "Sequence-based control strategy with current limiting for the fault ride-through of inverter-interfaced distributed generators," *IEEE Trans. Sustain. Energy*, vol. 11, no. 1, pp. 165–174, 2020.

[100] M. Parvez, M. F. M. Elias, and N. A. Rahim, "Performance analysis of PR current controller for single-phase inverters," in *4th IET Clean Energy and Technology Conference (CEAT 2016)*, pp. 1–8, 2016.

[101] R. Teodorescu, M. Liserre, and P. Rodriguez, *Grid Converters for Photovoltaic and Photovoltaic and Wind Power Systems*. Wiley-IEEE Press, 2011.

[102] N. Baeckeland, D. Venkatramanan, M. Kleemann, and S. Dhople, "Stationary-frame grid-forming inverter control architectures for unbalanced fault-current limiting," *IEEE Trans. Energy Convers.*, vol. 37, no. 4, pp. 2813–2825, 2022.

[103] M. Hamzeh, H. Karimi, and H. Mokhtari, "Harmonic and negative-sequence current control in an islanded multi-bus microgrid," *IEEE Trans. Smart Grid*, vol. 5, no. 1, pp. 167–176, 2014.

[104] P. Harsha Gadde and S. Brahma, "Comparison of PR and PI controllers for inverter control in an unbalanced microgrid," in *2020 52nd North American Power Symposium, NAPS 2020*, pp. 1–6, 2021.

[105] N. R. Merritt, C. Chakraborty, and P. Bajpai, “New voltage control strategies for VSC-based DG units in an unbalanced microgrid,” *IEEE Trans. Sustain. Energy*, vol. 8, no. 3, pp. 1127–1139, 2017.

[106] M. Amin, J. A. Suul, S. D’Arco, E. Tedeschi, and M. Molinas, “Impact of state-space modelling fidelity on the small-signal dynamics of VSC-HVDC systems,” in *11th IET International Conference on AC and DC Power Transmission*, pp. 1–11, 2015.

[107] L. Xinyu, D. Xiong, and W. Haijiao, “A discussion of eigenvalue-based and impedance- based methods in VSC system,” in *2021 IEEE 4th International Electrical and Energy Conference (CIEEC)*, pp. 1–5, 2021.

[108] M. Amin, A. Rygg, and M. Molinas, “Impedance-based and eigenvalue based stability assessment compared in VSC-HVDC system,” in *2016 IEEE Energy Conversion Congress and Exposition (ECCE)*, pp. 1–8, 2016.

[109] M. Amin and M. Molinas, “Small-signal stability assessment of power electronics based power systems: a discussion of impedance-and eigenvalue-based methods,” *IEEE Trans. Ind. Appl.*, vol. 53, no. 5, pp. 5014–5030, 2017.

[110] Y. Mishra, S. Mishra, F. Li, Z. Dong, and R. C. Bansal, “Small-signal stability analysis of a DFIG-based wind power system under different modes of operation,” *IEEE Trans. Energy Convers.*, vol. 24, no. 4, pp. 972–982, 2009.

[111] G. O. Kalcon, G. P. Adam, O. Anaya-Lara, S. Lo, and K. Uhlen, “Small-signal stability analysis of multi-terminal VSC-based DC transmission systems,” *IEEE Trans. Power Syst.*, vol. 27, no. 4, pp. 1818–1830, 2012.

[112] J. Beerten, S. D’Arco, and J. A. Suul, “Identification and small-signal analysis of interaction modes in VSC MTDC systems,” *IEEE Trans. Power Deliv.*, vol. 31, no. 2, pp. 888–897, 2016.

[113] R. D. Middlebrook, “Input filter considerations in design and application of switching regulators,” in *1976 IEEE Industry Applications Society Annual Meeting*, pp. 366–382, 1976.

[114] Y. Chen, “Small signal impedance modelling and stability assessment of HVDC

systems," University of Strathclyde, 2020.

[115] D. Dong, B. Wen, D. Boroyevich, P. Mattavelli, and Y. Xue, "Analysis of phase-locked loop low-frequency stability in three-phase grid-connected power converters considering impedance interactions," *IEEE Trans. Ind. Electron.*, vol. 62, no. 1, pp. 310–321, 2015.

[116] J. Sun, "Small-signal methods for AC distributed power systems-a review," *IEEE Trans. Power Electron.*, vol. 24, no. 11, pp. 2545–2554, 2009.

[117] N. Hadjsaïd and J. Sabonnadière, "Stability analysis of power systems by the generalised Nyquist criterion," in *1994 International Conference on Control - Control '94.*, pp. 323–354, 2013.

[118] B. Wen, D. Boroyevich, R. Burgos, P. Mattavelli, and Z. Shen, "D-Q impedance specification for balanced three-phase AC distributed power system," in *2015 IEEE Applied Power Electronics Conference and Exposition (APEC)*, pp. 2757–2771, 2015.

[119] C. Henderson, L. Xu, and A. Egea-Alvarez, "PN admittance characterisation of grid supporting VSC controllers with negative sequence regulation and inertia emulation," in *2021 23rd European Conference on Power Electronics and Applications (EPE'21 ECCE Europe)*, pp. 1–10, 2021.

[120] J. Sun, "Impedance-based stability criterion for grid-connected inverters," *2019 21st Eur. Conf. Power Electron. Appl. (EPE '19 ECCE Eur.*, vol. 26, no. 11, pp. 3075–3078, 2011.

[121] G. S. Thandi, R. Zhang, K. Xing, F. C. Lee, and D. Boroyevich, "Modeling, control and stability analysis of a PEBB based dc DPS," *IEEE Trans. Power Deliv.*, vol. 14, no. 2, pp. 497–505, 1999.

[122] S. Sang, N. Gao, X. Cai, and R. Li, "A novel power-voltage control strategy for the grid-tied inverter to raise the rated power injection level in a weak grid," *IEEE J. Emerg. Sel. Top. Power Electron.*, vol. 6, no. 1, pp. 219–232, 2018.

[123] A. Egea-alvarez, "Analysis of controller bandwidth interactions for vector-controlled VSC connected to very weak AC grids," *IEEE J. Emerg. Sel. Top.*

Power Electron., 2020.

[124] B. Wen, D. Boroyevich, R. Burgos, P. Mattavelli, and Z. Shen, "Analysis of D-Q Small-Signal Impedance of Grid-Tied Inverters," *IEEE Trans. Power Electron.*, vol. 31, no. 1, pp. 675–687, 2016.

[125] Y. Xing, G. Zhang, B. Wang, J. Li, and Q. Huang, "Modeling and stability analysis for grid-forming converter in a renewable energy generation system," *Int. J. Electr. Power Energy Syst.*, pp. 1–22, 2022.

[126] Y. Liao, X. Wang, F. Liu, K. Xin, and Y. Liu, "Sub-Synchronous Control Interaction in Grid-Forming VSCs with Droop Control," in *2019 4th IEEE Workshop on the Electronic Grid, eGRID 2019*, 2019, pp. 1–6.

[127] N. Pogaku, M. Prodanovic, and T. C. Green, "Modeling, analysis and testing of autonomous operation of an inverter-based microgrid," *IEEE Trans. Power Electron.*, vol. 22, no. 2, pp. 613–625, 2007.

[128] Y. Prabowo, V. M. Iyer, B. Kim, and S. Bhattacharya, "Modeling and stability assessment of single-phase droop controlled solid state transformer," in *ICPE 2019 - ECCE Asia - 10th International Conference on Power Electronics - ECCE Asia*, pp. 3285–3291, 2019.

[129] L. Xu, L. Yao, and C. Sasse, "Grid integration of large DFIG-based wind farms using VSC transmission," *IEEE Trans. Power Syst.*, vol. 22, no. 3, pp. 976–984, 2007.

[130] S. Yazdani, M. Ferdowsi, and P. Shamsi, "Power synchronization PID control method for grid-connected voltage-source converters," in *2020 IEEE Kansas Power and Energy Conference (KPEC)*, pp. 1–6, 2020.

[131] X. Wang and X. Wang, "Power-synchronized current control for grid-connected converter," in *2021 IEEE Energy Conversion Congress and Exposition (ECCE)*, no. 1, pp. 329–334, 2021.

[132] S. R. Bowes, "Advanced regular-sampled PWM control techniques for drives and static power converters," *IEEE Trans. Ind. Electron.*, vol. 42, no. 4, pp. 367–373, 1995.

[133] M. P. Kazmierkowski and L. Malesani, “Current control techniques for three-phase voltage-source PWM converters : a survey,” *IEEE Trans. Ind. Electron.*, vol. 45, no. 5, pp. 691–703, 1998.

[134] L. Yu, R. Li, and L. Xu, “Distributed PLL-based control of offshore wind turbines connected with diode-rectifier-based HVDC systems,” *IEEE Trans. Power Deliv.*, vol. 33, no. 3, pp. 1328–1336, 2018.

[135] K. Vikram and V. Blasko, “Operation of a phase locked loop system under distorted utility conditions,” *IEEE Trans. Ind. Appl.*, vol. 33, no. 1, pp. 58–63, 1997.

[136] Z. Ali, N. Christo, L. Hadjidemetriou, E. Kyriakides, and Y. Yang, “Three-phase phase-locked loop synchronization algorithms for grid- connected renewable energy systems : A review,” *Renew. Sustain. Energy Rev.*, vol. 90, pp. 434–452, 2018.

[137] A. Jana, P. K. Gayen, P. K. Dhara, and R. Garai, “Simultaneous active and reactive power control of single-phase grid connected battery storage system,” in *2017 Devices for Integrated Circuit (DevIC)*, pp. 289–293, 2017.

[138] S. Grunau and F. W. Fuchs, “Effect of wind-energy power injection into weak grids,” in *European Wind Energy Conference and Exhibition 2012, EWEC 2012*, vol. 2, pp. 1150–1156, 2012.

[139] A. Egea-Alvarez, C. Barker, F. Hassan, and O. Gomis-Bellmunt, “Capability curves of a VSC-HVDC connected to a weak AC grid considering stability and power limits,” in *11th IET International Conference on AC and DC Power Transmission*, pp. 1–5, 2015.

[140] G. P. Adam, K. H. Ahmed, S. J. Finney, K. Bell, and B. W. Williams, “New breed of network fault-tolerant voltage-source-converter HVDC transmission system,” *IEEE Trans. Power Syst.*, vol. 28, no. 1, pp. 335–345, 2013.

[141] L. Zhang, L. Harnefors, S. Member, H. Nee, and S. Member, “Interconnection of two very weak AC systems by VSC-HVDC links using,” *IEEE Trans. Power Syst.*, vol. 26, no. 1, pp. 344–355, 2011.

[142] H. Wu and X. Wang, “Design-oriented transient stability analysis of grid-

connected converters with power synchronization control," *IEEE Trans. Ind. Electron.*, vol. 66, no. 8, pp. 6473–6482, 2019.

[143] K. D. Brabandere, B. Bolsens, J. V. D. Keybus, A. Woyte, and J. Driesen, "A voltage and frequency droop control method for parallel inverters," *IEEE Trans. Power Electron.*, vol. 22, no. 4, pp. 1107–1115, 2007.

[144] R. T. Pinto, P. Bauer, S. F. Rodrigues, E. J. Wiggelinkhuizen, J. Pierik, and B. Ferreira, "A novel distributed direct-voltage control strategy for grid integration of offshore wind energy systems through MTDC network," *IEEE Trans. Ind. Electron.*, vol. 60, no. 6, pp. 2429–2441, 2013.

[145] J. C. Vasquez, J. M. Guerrero, A. Luna, P. Rodríguez, and R. Teodorescu, "Adaptive droop control applied to voltage-source inverters operating in grid-connected and islanded modes," *IEEE Trans. Ind. Electron.*, vol. 56, no. 10, pp. 4088–4096, 2009.

[146] H. Laaksonen, P. Saari, and R. Komulainen, "Voltage and frequency control of the inverter based weak LV network microgrid," in *2005 International Conference on Future Power Systems*, no. 2, pp. 5–10, 2005.

[147] R. Li, L. Yu, and L. Xu, "Offshore AC fault protection of diode rectifier unit based HVDC system for wind energy transmission," *IEEE Trans. Ind. Electron.*, vol. 66, no. 7, pp. 5289–5299, 2019.

[148] S. Foster, L. Xu, and B. Fox, "Coordinated control and operation of DFIG and FSIG based wind farms," in *2007 IEEE Lausanne Power Tech*, pp. 522–527, 2007.

[149] L. Xu, B. R. Andersen, and P. Cartwright, "VSC transmission operating under unbalanced AC conditions — analysis and control design," *IEEE Trans. Power Deliv.*, vol. 20, no. 1, pp. 427–434, 2005.

[150] M. Prodanović and T. C. Green, "High-quality power generation through distributed control of a power park microgrid," *IEEE Trans. Ind. Electron.*, vol. 53, no. 5, pp. 1471–1482, 2006.

[151] C. Glockler, D. Duckwitz, and F. Welck, "Virtual synchronous machine control with virtual resistor for enhanced short circuit capability," in *2017 IEEE PES*

Innovative Smart Grid Technologies Conference Europe (ISGT-Europe), pp. 1–6, 2017.

[152] C. Jiang, A. D. Sinkar, M. K. Das, A. M. Gole, and V. Pathirana, "A comparative study of master-slave control and virtual synchronous machine control for parallel VSC-HVDC links feeding passive loads on offshore platforms," in *15th IET International Conference on AC and DC Power Transmission (ACDC 2019)*, pp. 1–6, 2019.

[153] Y. Jing, R. Li, L. Xu, and Y. Wang, "Enhanced AC voltage and frequency control of offshore MMC station for wind farm connection," *IET Renew. Power Gener.*, vol. 12, no. 15, pp. 1771–1777, 2018.

[154] H. Fujita, Y. Watanabe, and H. Akagi, "Control and analysis of a unified power flow controller," *IEEE Trans. Power Electron.*, vol. 14, no. 6, pp. 1021–1027, 1999.

[155] Q. Yu, S. D. Round, L. E. Norum, and T. M. Undeland, "Dynamic control of a unified power flow controller," in *IEEE Power Electronics Specialists Conference*, pp. 508–514, 1996.

[156] L. Xu, "Enhanced control and operation of DFIG-based wind farms during network unbalance," *IEEE Trans. Energy Convers.*, vol. 23, no. 4, pp. 1073–1081, 2008.

[157] L. Xu, "Coordinated control of DFIG ' s rotor and grid side converters during network unbalance," *IEEE Trans. Power Electron.*, vol. 23, no. 3, pp. 1041–1049, 2008.

[158] L. Shi, G. P. Adam, R. Li, and L. Xu, "Control of offshore MMC during asymmetric offshore AC faults for wind power transmission," *IEEE J. Emerg. Sel. Top. Power Electron.*, vol. 8, no. 2, pp. 1074–1083, 2020.

[159] S. Silwal, M. Karimi-Ghartemani, R. Sharma, and H. Karimi, "Impact of feed-forward and decoupling terms on stability of grid-connected inverters," in *IEEE International Symposium on Industrial Electronics*, pp. 2641–2646, 2019.

[160] S. Huang, L. Kong, T. Wei, and G. Zhang, "Comparative analysis of PI decoupling control strategies with or without feed-forward in SRF for three-phase power

supply," in *Proceedings of the 11th International Conference on Electrical Machines and Systems, ICEMS 2008*, pp. 2372–2377, 2008.

[161] Y. Chen and L. Xu, "Sequence-frame coupling admittance analysis and stability of VSC connected to weak grid," in *Proceedings of the IEEE International Conference on Industrial Technology*, pp. 1297–1303, 2021.

[162] G. Amico, A. Egea-Alvarez, L. Xu, and P. Brogan, "Stability margin definition for a converter-grid system based on diagonal dominance property in the sequence-frame," in *2019 21st European Conference on Power Electronics and Applications, EPE 2019 ECCE Europe*, pp. 1–10, 2019.

[163] P. T. Krein, J. Bentsman, R. M. Bass, and B. L. Lesieutre, "On the use of averaging for the analysis of power electronic systems," *IEEE Trans. Power Electron.*, vol. 5, no. 2, pp. 182–190, 1990.

[164] J. Sun and H. Grotstollen, "Symbolic analysis methods for averaged modeling of switching power converters," *IEEE Trans. Power Electron.*, vol. 12, no. 3, pp. 537–546, 1997.

[165] L. Harnefors, M. Bongiorno, and S. Lundberg, "Input-admittance calculation and shaping for controlled voltage-source converters," *IEEE Trans. Ind. Electron.*, vol. 54, no. 6, pp. 3323–3334, 2007.

[166] M. Cespedes and J. Sun, "Impedance modeling and analysis of grid-connected voltage-source converters," *IEEE Trans. Power Electron.*, vol. 29, no. 3, pp. 1254–1261, 2014.

[167] Y. Chen, L. Xu, S. Member, A. Egea-àlvarez, and O. D. Adeuyi, "MMC impedance modelling and interaction of converters in close proximity," *IEEE J. Emerg. Sel. Top. Power Electron.*, 2020.

[168] B. Wen, D. Boroyevich, P. Mattavelli, R. Burgos, and Z. Shen, "Modeling the output impedance negative incremental resistance behavior of grid-tied inverters," in *2014 IEEE Applied Power Electronics Conference and Exposition - APEC 2014*, pp. 1799–1806, 2014.

[169] S. Shah, "Impedance of three-phase systems in DQ, sequence, and phasor domains,"

2020. https://www.nrel.gov/docs/fy20osti/77669.pdf (accessed Feb. 20, 2023).

[170] S. Shah and L. Parsa, “Impedance modeling of three-phase voltage source converters in DQ, sequence, and phasor domains,” *IEEE Trans. Energy Convers.*, vol. 32, no. 3, pp. 1139–1150, 2017.

[171] A. Rygg, M. Molinas, C. Zhang, and X. Cai, “A modified sequence-domain impedance definition and its equivalence to the dq-domain impedance definition for the stability analysis of AC power electronic systems,” *IEEE J. Emerg. Sel. Top. Power Electron.*, vol. 4, no. 4, pp. 1383–1396, 2016.

[172] M. Cespedes and J. Sun, “Renewable energy systems instability involving grid-parallel inverters,” in *2009 Twenty-Fourth Annual IEEE Applied Power Electronics Conference and Exposition*, pp. 1971–1977, 2009.

[173] G. Amico, A. Egea-àlvarez, P. Brogan, and S. Zhang, “Small-Signal converter admittance in the pn-frame : systematic derivation and analysis of the cross-coupling terms,” *IEEE Trans. Energy Convers.*, vol. 34, no. 4, pp. 1829–1838, 2019.

[174] B. Wen, D. Boroyevich, P. Mattavelli, Z. Shen, and R. Burgos, “Experimental verification of the Generalized Nyquist stability criterion for balanced three-phase ac systems in the presence of constant power loads,” in *2012 IEEE Energy Conversion Congress and Exposition (ECCE)*, pp. 3926–3933, 2012.

Author's Publications

[1] **Y. Lu** and L. Xu, "Generalised grid-forming VSC control for grid connection and island network," in *The 10th International Conference on Power Electronics, Machines and Drives (PEMD 2020)*, 2021, pp. 832–837-Chapter 4

Abstact: This study proposes a generalised grid-forming VSC control for grid connection and island network for distributed generations. The proposed control scheme is based on grid-forming direct voltage control to establish the AC voltage and frequency for island network, while it works as a controlled AC voltage source to regulate the active and reactive power flowing to the local load and AC grid during grid-connected operation. Strategy for fault current limiting is also proposed to overcome the overcurrent problem brought by the grid-forming direct voltage control. Simulation results during three-phase AC fault and transition from grid-connected operation to islanding operation are presented to confirm the feasibility and effectiveness of the proposed control strategy.

[2] **Y. Lu**, Y. Chen and L. Xu, "Control of grid-forming VSC during symmetrical and asymmetrical AC fault," in *IET Renewable Power Generation and Future Power Systems Conference*. (Accepted)-Chapter 5

Abstract: A grid-forming VSC control strategy when connected to a weak grid considering the ability of symmetrical and asymmetrical faults ride-through is studied in this paper. The general control scheme is based on the grid-forming direct voltage control to work as a controlled AC voltage source by regulating the active and reactive power delivering to the AC grid. A voltage balancing control loop is proposed to overcome the limited overcurrent capability of the direct voltage control based grid-forming VSC during AC faults. To provide individual control for positive- and negative-sequence current, the control system is based on the double synchronous reference frames. A dq current distribution control is developed to share the positive-sequence active and reactive current, while a negative-sequence current control is proposed to control the negative-

sequence active and reactive current in the event of an asymmetrical fault. Simulation results are presented to confirm the feasibility of the proposed control strategy.